Haus, R., Kappel, D., Arnold, G.. Planetary Space Science 117, 262-294 (2015) Preprint

Doi: 10.1016/j.pss.2015.06.024

Radiative heating and cooling in the middle and lower atmosphere of Venus and responses to atmospheric and spectroscopic parameter variations

R. Haus[a*], D. Kappel[b], G. Arnold[b]

[a]Westfälische Wilhelms-Universität Münster, Institute for Planetology, Wilhelm-Klemm-Str.10, 48149 Münster, Germany, rainer.haus@gmx.de
[b]German Aerospace Center (DLR), Institute of Planetary Research, Rutherfordstrasse 2, 12489 Berlin, Germany, dkappel@gmx.net, gabriele.arnold@dlr.de

ABSTRACT

A sophisticated radiative transfer model that considers absorption, emission, and multiple scattering by gaseous and particulate constituents over the broad spectral range 0.125-1000 µm is applied to calculate radiative fluxes and temperature change rates in the middle and lower atmosphere of Venus (0-100 km). Responses of these quantities to spectroscopic and atmospheric parameter variations are examined in great detail. Spectroscopic parameter studies include the definition of an optimum spectral grid for monochromatic calculations as well as comparisons for different input data with respect to spectral line databases, continuum absorption, line shape factors, and solar irradiance spectra. Atmospheric parameter studies are based on distinct variations of an initial model data set. Analyses of actual variations of the radiative energy budget using atmospheric features that have been recently retrieved from Venus Express data will be subject of a subsequent paper.

The calculated cooling (heating) rates are very reliable at altitudes below 95 (85) km with maximum uncertainties of about 0.25 K/day. Heating uncertainties may reach 3-5 K/day at 100 km. Using equivalent Planck radiation as solar insolation source in place of measured spectra is not recommended. Cooling rates strongly respond to variations of atmospheric thermal structure, while heating rates are less sensitive. The influence of mesospheric minor gas variations is small, but may become more important near the cloud base and in case of episodic SO_2 boosts. Responses to cloud mode 1 particle abundance changes are weak, but variations of other mode parameters (abundances, cloud top and base altitudes) may significantly alter radiative temperature change rates up to 50% in Venus' lower mesosphere and upper troposphere.

A new model for the unknown UV absorber for two altitude domains is proposed. It is not directly linked to cloud particle modes and permits an investigation of radiative effects regardless of the absorbers's chemical composition. A globally averaged Bond albedo of Venus of 0.763 is inferred in accordance with previous results. Considering the gaseous UV absorbers SO_2 and CO_2 shortward of 0.32 µm, the globally averaged deposited solar net flux at the top of atmosphere (TOA) and the outgoing thermal net flux differ by only 1.5 W m^{-2} around the mean value of 159 W m^{-2} for the selected initial atmospheric model. Global radiative equilibrium can be achieved by moderate adjustments of cloud mode and UV absorber abundances. Half of the TOA solar net flux is absorbed by atmospheric constituents at altitudes above 63 km. Consideration of the unknown UV absorber provides about 50% more heating at 68 km compared with a neglect of this opacity source. Less than 5% of the incident flux reaches the surface. There is a broad net cooling region between 70 and 80 km with a strong increase of cooling toward the poles. A net radiative temperature change rate gradient is also observed at 65 km where heating occurs at low latitudes. At altitudes above 80 km, net heating dominates the low and mid latitudes, while net cooling prevails at high latitudes leading to a dominant global

average net heating that has to be balanced by dynamical processes to maintain the observed thermal structure. The results of energy balance response analyses will serve as reference for ongoing investigations and provide a profound data base to improve the understanding of radiative forcing of atmospheric dynamical processes.

1. Introduction

The specific spatial and temporal distribution of atmospheric sources and sinks of radiative energy that is defined by the balance between incoming solar and escaping thermal radiation constrains the thermal structure and forces the dynamics of planetary atmospheres. Vertical profiles of radiation fluxes cannot be measured by orbiting remote sensing instruments, and there are only few in-situ data sampled by early Venus mission descent probes in very limited wavelength ranges. Therefore, vertical flux profiles have to be calculated by modeling of radiative transfer. In contrast with radiance simulation and retrieval procedures that usually focus on comparatively narrow spectral ranges (e.g. the 4.3 and 15 µm CO_2 bands for temperature profile and cloud parameter retrievals), the calculation of atmospheric solar and thermal fluxes requires consideration of broad spectral ranges and large computational effort.

Former investigations of radiative processes in the atmosphere of Venus based on Pioneer Venus and Venera-15 data (Pollack et al., 1980; Schofield and Taylor, 1982; 1983; Tomasko et al., 1985; Crisp, 1986; Crisp, 1989; Haus and Goering, 1990; Titov, 1995) already indicated a peculiar distribution of sources and sinks of radiative energy that is significantly different from that on Earth and that is most likely the driving force of the remarkable zonal superrotation of the atmosphere. They also revealed the strong sensitivity of radiative energy balance to atmospheric parameter variations like changes of temperature structure, abundances of radiative active trace gases, and cloud microphysical properties and vertical distributions of individual cloud mode abundances.

Summaries of current knowledge about the planetary energy balance characteristics and of open issues were given by Taylor (2006) and Titov et al. (2006; 2007; 2012). According to these references, about 76% of the incoming solar energy flux is reflected back to space by the strongly scattering clouds. About one half of the remaining solar flux is absorbed at levels above 65 km by CO_2, the clouds, and a still enigmatic 'unknown UV absorber' that resides in the upper and middle cloud layers (57-72 km) and causes the observed broad depression in the spherical albedo spectrum in the near UV and visible range between 0.3 and 0.7 µm. Less than 5% of the flux received at the top of atmosphere reaches the surface (Titov et al., 2007). Above the cloud tops, near infrared CO_2 bands absorb enough energy to produce globally averaged heating rates ranging from 4 K/day at 71 km to more than 50 K/day at 100 km (Crisp, 1986). Together with reflected solar radiation, atmospheric thermal emissions determine the outgoing radiative energy flux at the top of the atmosphere. Globally averaged cooling rates above the cloud tops are in the order of 5 K/day (Crisp, 1989). Below the clouds (<48 km), both heating and cooling rates gradually decrease to ~0.001 K/day at the surface due to the large air density and heat capacity.

Sensitivity analyses of radiative forcing are of special importance for altitudes 45-80 km where the fluxes are strongly affected by variations of cloud properties (e.g., mode abundances, cloud top altitudes). This was recently shown by Lee et al. (2015). The clouds of Venus are the most important opacity source after CO_2. The total cloud opacity, to give an example here, can vary between about 22 and 55 at 1 µm (Haus et al., 2014a). Cloud parameter variations affect the heating and cooling rates so heavily, because they alter the visual albedo of the planet, and thus the flow of solar energy through the atmosphere. They also alter the thermal infrared opacity of the middle atmosphere, thereby affecting the atmospheric temperature

fields. The clouds block the upward thermal flux from the surface and the deep atmosphere and are a major contributor to the strong greenhouse effect in Venus' atmosphere.

Simulated radiative fluxes and temperature change rates are not only very sensitive to atmospheric thermal structure and composition, but also to spectroscopic data and numerical algorithms while using these data. Incoming solar radiation above the clouds is mainly absorbed by strong CO_2 bands located at 4.3, 2.7, and 2.0 µm. Thermal emission at these altitudes is controlled by the 15 µm CO_2 band. The comparatively low pressure at high altitudes (~0.03 mb at 100 km) amplifies the relative influence of gaseous absorption line cores on the overall absorption characteristics. Thus, a high spectral resolution of absorption cross-sections (0.01 cm^{-1} or better) and sophisticated line-by-line procedures are often required to make the monochromatic flux calculations sufficiently accurate. Large temperature change rate errors may occur when the spectral resolution used in the calculations is too coarse.

Early modeling results were not strongly constrained by measurements before the latest mission to Venus, ESA's Venus Express (VEX) mission, with its great planetary mapping potential. Moreover, early analyses were hampered by computational constraints during that time, and the use of band models for gaseous absorbers was mostly unavoidable. The VEX orbiter has carried the most powerful remote sensing suite of instruments ever flown to Venus. Together with the other instruments (VMC, SPICAV/SOIR, VeRa, ASPERA, MAG), the Visible and Infrared Thermal Imaging Spectrometer VIRTIS (Piccioni et al., 2007; Drossart et al., 2007; Arnold et al., 2012) has enabled for the first time a long-time study of the structure, composition, chemistry, and dynamics of the atmosphere and the cloud system, as well as investigations of the thermal and compositional characteristics of the planetary surface. VIRTIS-M-IR measurements have been recently used by Haus et al. (2013a; 2013b; 2014a; 2014b; 2015) to retrieve information on mesospheric nightside thermal structure and cloud features, and on minor gas distributions in the lower atmosphere using new methodical approaches. Temperature profile and cloud top altitude retrieval results using VIRTIS spectra were also reported by Grassi et al. (2010; 2014). Resulting maps for the southern hemisphere cover parameter variations with altitude, latitude, local time, and mission time. Together with new VeRa temperature retrieval results (Tellmann et al., 2009) these data will finally allow the calculation of improved atmospheric radiation fluxes and temperature change rates that characterize the radiative energy balance of Venus' middle and lower atmosphere.

It is the main goal of the present paper to investigate the variability of fluxes and temperature change rates in the middle and lower atmosphere of Venus (0-100 km) within the limits of possible parameter variations that were determined from VIRTIS measurements or that are specified based on different spectroscopic model changes. Such a detailed study was not reported before. Due to the great number of required individual parameter influence analyses, a separate presentation of the corresponding results is well justified. It is intended to serve as reference for future investigations. Thus, the present paper is going to use existing atmospheric standard models together with distinct parameter variations. The specification of the radiative energy balance based on improved models of latitude and local time dependent atmospheric features, which have been retrieved from Venus Express data, will be the focus of a subsequent paper in near future.

Section 2 provides a detailed description of the radiative transfer model. After a short definition of radiometric quantities and characterization of used radiative transfer codes (2.1), basic top of atmosphere blackbody radiation features (2.2) and real solar irradiance spectra (2.3) are discussed. Initial one-dimensional atmospheric standard models are specified in Section 2.4. An overview of atmospheric absorption and scattering properties is given in Sections 2.5 and 2.6 for gaseous and particulate

constituents, respectively. Section 3 discusses spectral radiation fluxes at the top of atmosphere. Based on known peculiarities of Venus' spectral Bond albedo shortward of 1 μm, a new model for the unknown UV absorber is developed. Section 4 presents the basic definitions and equations that are required to calculate individual atmospheric flux components and radiative temperature change rates. The discussion Section 5 starts with a description of modeling results for an initial standard model (5.1). Results of detailed studies of temperature change rate responses to spectroscopic and atmospheric parameter variations are discussed in Sections 5.2 and 5.3. A comparison with earlier results is performed in Section 5.4, and a preliminary sketch of the latitude-dependent net radiative heating field is also shown there. The main methodical aspects and results are summarized in Section 6.

2. The radiative transfer model

A sophisticated radiative transfer simulation model (RTM) is applied to calculate radiance and flux spectra in dependence on atmospheric and spectroscopic parameters. The atmospheric models required for RTM operation encompass altitude profiles of temperature, minor gas abundances, and cloud mode particle densities as well as cloud mode composition. These models are used to calculate quasi-monochromatic molecular and particulate absorption and scattering coefficients at defined levels of a plane-parallel atmosphere. Solar flux calculations consider different data sets of solar irradiance spectra.

2.1. Radiative transfer equation

The radiative transfer equation for a plane-parallel atmosphere can be written in a highly compressed manner in the form (Haus and Titov, 2000)

$$I^{\pm}(\lambda,z_R,\theta,\psi) = I^{B}(\lambda,z_B,\theta,\psi)\ \tau(\lambda,z_R,z_B,\theta) + \int_{z_R}^{z_B} J(\lambda,z,\theta,\psi)\ W(\lambda,z_R,z,\theta)\,dz. \quad (1)$$

Latitude and local time dependences are not explicitly marked here. $I^{\pm}(\lambda,z_R,\theta,\psi)$ is the upward (+) or downward (-) directed spectral (monochromatic) radiance at wavelength λ, atmospheric reference level z_R, zenith angle θ, and azimuth angle ψ. θ and ψ are the angles of radiance propagation. $I^{\pm}$ is given in units of [W m^{-2} sr^{-1} μm^{-1}] as spectral radiant energy [Ws μm^{-1}] per units of time, projected area, and solid angle. I^{B} in the first term is the corresponding radiance at the boundary altitude z_B (surface or top of atmosphere), and τ is the monochromatic total atmospheric transmittance between levels z_R and z_B according to

$$\tau(\lambda,z_R,z_B,\theta) = \exp[-u(\lambda,z_R,z_B)/\cos\theta]. \quad (2)$$

u is the monochromatic cumulative atmospheric optical depth,

$$u(\lambda,z_R,z_B) = \int_{z_R}^{z_B} \sigma(\lambda,z)\,n(z)\,dz. \quad (3)$$

σ is the monochromatic extinction cross-section. Eqs. (2) and (3) may also define pure absorption or scattering features of an atmospheric layer. n is the number density of an atmospheric constituent. σ and n depend on pressure and temperature at level z. The product σ n is called (volume) extinction coefficient (in units of [km^{-1}]). Its numerical value is equal to the dimensionless optical depth of a 1 km thick layer.

The last term in Eq. (1) describes the integral contribution of each atmospheric layer. J is the radiation source function and W the so-called weighting function that represents the derivative of $\tau(\lambda,z_R,z,\theta)$ with respect to z. The source function encompasses contributions from single scattering of directional external radiation (direct solar radiation), multiple scattering of direct and diffuse internal radiation, and thermal emission. The lower boundary radiance is determined by surface reflection of the directional and diffuse spectral sky radiation and the spectral thermal emission of the planetary surface, while the upper boundary radiance is exclusively due to external radiation at the top of atmosphere described by the spectral solar irradiance. The intricate integro-differential Eq. (1) can be solved by use of suitable numerical multiple

scattering procedures. One of these techniques, the Successive Order Approximation (SA) (e.g. Irvin, 1975), has been described in detail by Haus and Titov (2000). It was extensively used to study radiative transfer in the atmospheres of Earth and Mars. When the opacity of an atmospheric layer is very large and the single scattering albedo approaches unity (as in case of Venus at many wavelengths), the use of SA is not very recommendable however, since convergence is slow. Thus, the DISORT (Discrete Ordinates Radiative Transfer) code (Stamnes et al., 1988), which has much higher calculation efficiency in such cases, was adapted into the RTM for final applications to Venus. A comparison of SA and DISORT in the spectral range 1.0-2.6 μm was previously performed by Haus and Arnold (2010).

The upward or downward directed spectral radiant flux density (irradiance) is calculated according to

$$\begin{aligned} F^{\pm}(\lambda,z) &= \int_{\Omega} I^{\pm}(\lambda,z,\Omega)\cos\theta\, d\Omega \\ &= \int_0^{2\pi}\int_0^{\pi/2} I^{\pm}(\lambda,z,\theta,\psi)\cos\theta\sin\theta\, d\theta\, d\psi \\ &= 2\pi\int_0^{1} I^{\pm *}(\lambda,z,\mu)\,\mu\, d\mu \end{aligned} \qquad (4)$$

where Ω is the (half, that is, upper or lower hemisphere) solid angle, and μ = cos θ. In contrast with $I^{\pm}$, $I^{\pm *}$ is the azimuth-independent spectral radiance. Radiant flux densities $F^{\pm}$ are often simply denoted as 'fluxes' in the literature. Although not fully correct with respect to the proper definition of radiometric quantities, this notation will also be used in the present paper due to its abbreviating nature. Spectral fluxes are given in units of [W m^{-2} μm^{-1}]. In case of isotropic Planck radiation B, Eq. (4) yields F=πB.

2.2. Top of atmosphere black body radiation under radiative balance conditions

A planet receives its energy from the Sun. The amount of radiation power P [W] per unit area [m^2] that incides on a plane perpendicular to the rays at the top of a planetary atmosphere (TOA) and at a mean distance r_D from the Sun is defined as the 'solar constant'. This flux density E* of solar energy can be calculated using the Stefan-Boltzmann law and the inverse square law,

$$E^* = \sigma\, T_S^{\,4}\, R_S^{\,2} / r_D^{\,2}. \qquad (5)$$

σ is the Stefan-Boltzmann constant (σ = 5.6704x10^{-8} $Wm^{-2}K^{-4}$), T_S and R_S are the effective blackbody surface temperature and the equatorial radius (R_S = 6.96342x10^8 m) of the Sun. For the Earth, r_D=1 AU=1.496x10^{11} m. The 1982 World Meteorological Organization (WMO) value for the Earth's solar constant is E^{*Earth} = 1367 W m^{-2} corresponding to T_S=5775.5 K.

The Sun-Venus distance is r_D = 0.723 AU. Thus, a factor of 1.913 has to be used to find the solar constant for Venus. Eq. (5) yields a WMO value of E^{*Venus} = 2615.15 W m^{-2}.

For a planet in global radiative balance, the total outgoing radiation power P^{OUT} must balance the incoming power P^{IN}. Considering the effective receiver cross-section area $\pi R_P^{\,2}$ of the planet with R_P being the planetary radius, P^{IN} is given by

$$P^{IN} = E^*(1-A)\,\pi R_P^{\,2}. \qquad (6)$$

The quantity A is the Bond albedo of the planet that defines the fraction of the total incident power (or flux) that is reflected back to space. The planet emits in all directions like a blackbody of uniform temperature T_P, the effective planetary emission temperature,

$$P^{OUT} = 4\pi\, R_P^{\,2}\, \sigma\, T_P^{\,4}. \qquad (7)$$

Relating the power equations to the area of the planetary hemisphere that is hit by solar light ($2\pi R_P^{\,2}$) or even to the full sphere and thus coming back to fluxes (flux densities), one finds the equation for the global radiative balance,

$$\frac{E^*(1-A)}{4} = \sigma\, T_P^{\,4}. \qquad (8)$$

Eq. (8) is now applied to determine T_P. Using A^{Earth}=0.31 and A^{Venus}=0.76 (Moroz et al.,

1985) and considering the WMO solar constant, the exact effective radiative balance temperatures are 253.94 K for Earth and 229.35 K for Venus, respectively. Although much closer to the Sun, Venus absorbs less solar energy and has a lower effective temperature than Earth due to its high Bond albedo. The globally averaged radiative balance fluxes on Venus that are absorbed and emitted according to WMO data are 156.9 Wm^{-2}.

The spectral distribution of Venus' TOA fluxes for blackbodies at Sun and effective radiative balance planetary temperatures that are calculated using Planck's law is illustrated in Fig. 1 as functions of wavelength (display A) and wavenumber (display B). The additional thin line shows the spectral flux distribution for an atmospheric temperature of 450 K, which is representative for lower atmospheric conditions at an altitude of about 35 km where minor gas distributions have been retrieved from VIRTIS data (Haus et al., 2015). Solar radiation has its maximum at 0.5 µm, while thermal radiation at 230 K peaks at 12.6 µm. The corresponding maximum flux values are indicated in the figure.

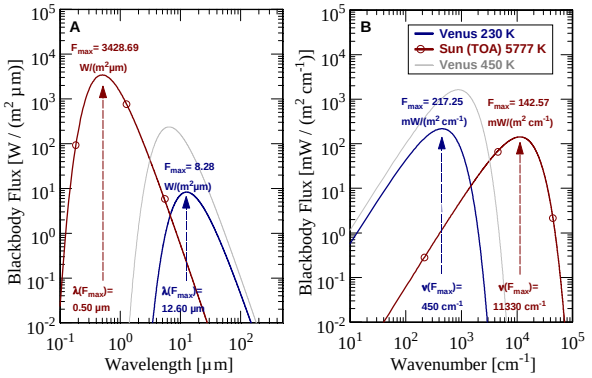

Figure 1. Spectral distribution of blackbody radiation fluxes B_F at temperatures of 5777, 230, and 450 K. A: B_F as function of wavelength, B: B_F as function of wavenumber.

The two main curves intersect at λ_x=7 µm. Solar radiation dominates shortward of λ_x and thermal radiation longward of λ_x. Nevertheless, absorption of solar radiation by atmospheric radiative active gases has to be considered up to at least 30 µm. Significant thermal emission contributions from the middle atmosphere may extend down to 3-4 µm. Lower atmosphere emission contributions to the energy balance can even be expected down to 1-2 µm. Solar fluxes should be investigated down to about 0.1 µm, thermal fluxes up to about 200 µm. It will be shown below that even the spectral range between 200 and 1000 µm should not be neglected.

Spectroscopic data on gaseous constituent absorption parameters always refer to wavenumber, and all monochromatic calculation procedures are accordingly based on this quantity. The spectral distribution of above defined fluxes as functions of wavenumber is shown in Fig. 1b. Note that the maximum of the solar curve for example is now located at 11330 cm^{-1} and not at 20000 cm^{-1} ($\upsilon[cm^{-1}]=10^4/(\lambda[\mu m])$). This is a consequence of the differential definition of the Planck functions, $B(\lambda)d\lambda$, $B(\upsilon)d\upsilon$ that requires consideration of a conversion factor of $\lambda^2/10$ when transforming $F(\lambda)$ in units of $[W/(m^2\mu m)]$ to $F(\upsilon)$ in units of $[mW/(m^2cm^{-1})]$. The two main curves intersect at 1485 cm^{-1}, solar influence has to be considered in the range 50-80000 cm^{-1}, thermal fluxes need to be investigated in the range 10-6000 cm^{-1}.

The two components of the radiative energy balance, solar absorption and thermal emission, are usually modeled independently from each other, and resulting temperature change rates are related to a full rotational period of the planet. One could also decide to include the thermal component into daylight period calculations and calculate pure thermal radiation only for the rest of a full day. This would provide the same results for net heating, however.

2.3. Real solar irradiance spectra

Solar irradiance spectra on Earth have been measured or theoretically calculated in the past by many researchers (e.g. Thekaekara, 1973; Neckel and Laabs, 1984; Mecherikunnel et al., 1983; Kurucz, 1995) and are subject of permanent improvements. Two datasets, which are available online, are used in the present study, the synthetic model of Kurucz (2011) and the ASTM Standard E490-00a (2006), which is a combination from

experimental and model data. The spectra are shown in Fig. 2 in the basic units and spectral increments in each case. Original ASTM data (display A) cover the (usable) range 0.125-1000 µm (10-80000 cm^{-1}). The ASTM spectral sampling varies from 1 nm shortward of 0.63 µm up to 50 nm at 10 µm, and even coarser distances are used longward of 10 µm. Original Kurucz data (display B) are available from 50-50000 cm^{-1} (0.2-200 µm) at spectral sampling of 1 cm^{-1}. Kurucz data have been extended toward 0.125 and 1000 µm (10 and 80000 cm^{-1}), respectively, applying an extrapolation technique. Outside these bounds, all irradiances are set to zero. Note that the irradiance curves in Fig. 2 refer to the mean Sun-Earth distance of 1 AU.

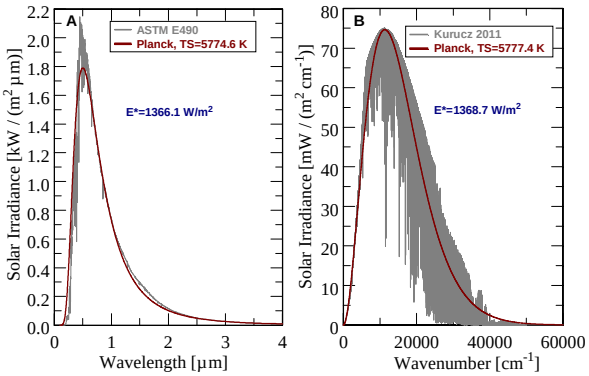

Figure 2. Solar irradiance spectra at the top of Earth's atmosphere. A: ASTM Standard E490-00a (2006), B: Kurucz (2011). E* is the resulting solar constant. TS is the equivalent blackbody temperature of the Sun.

Integration of the spectral irradiances over wavenumber or wavelength yields the solar constant E^{*Earth}, which is 1366.1 Wm^{-2} in case A and 1368.7 Wm^{-2} in case B. Eq. (5) can be utilized to determine the temperatures T_S that produce exactly the same solar constant values. Case A yields T_S = 5774.6 K, case B yields T_S = 5777.4 K. These temperatures are then used to calculate the equivalent Planck irradiance curves shown as thick lines in Fig. 2. Corresponding values of the solar constant at Venus (E^{*Venus}) are 2613.4 and 2618.4 Wm^{-2}, respectively. Based on these values, the globally averaged radiative balance fluxes are 156.8 and 157.1 Wm^{-2}.

Fig. 3 shows a direct comparison of Venus' TOA spectral irradiances in the wavenumber scale. A 3-point smoothing procedure is applied that is repeated 1000 times to produce a smoothed Kurucz spectrum that is better suited for this comparison. The wavenumber integral (the solar constant) does not change in consequence of this smoothing. The third curve in Fig. 3 is the Planck function for T_S=5777.4 K. Kurucz and ASTM spectra are very similar and are not expected to produce a significant difference with respect to radiative forcing of the atmosphere. But it is important to note that the equivalent Planck irradiance curves (being almost identical for both data sets) partly significantly deviate from the real spectra. Planck irradiances are usually smaller in the infrared spectral range, but show higher values in the visible and UV ranges. One could suppose that the overall differences will balance out. It will be shown in Section 5.2.4 that this is not the case. Since equivalent Planck irradiances are sometimes used in the literature to simulate the spectral distribution of the incoming solar radiation, it is important to estimate the resulting error in radiative energy calculations.

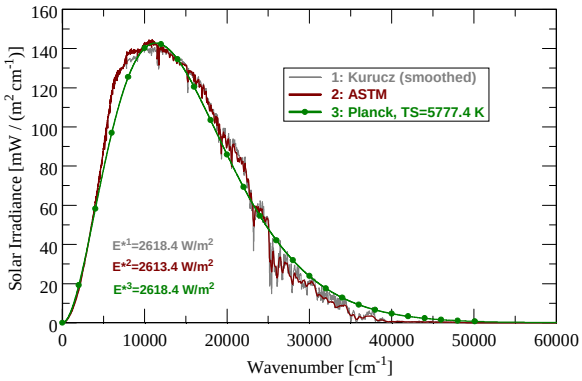

Figure 3. Comparison of solar spectra at the top of Venus's atmosphere as functions of wavenumber. E* is the resulting solar constant. Curve 3 is the Planck function for the Sun temperature TS=5777.4 K that yields exactly the same solar constant as curve 1.

2.4. Initial atmospheric standard model

2.4.1. Thermal structure

Atmospheric temperature altitude profiles on Venus' nightside have been recently retrieved from measured VIRTIS-M-IR spectra in the 4.3 µm CO_2 absorption band in the northern and southern hemisphere of Venus (Haus et al., 2013a; 2014a) using Smiths' relaxation method (Smith, 1970) and a predefined initial temperature model (VIRA-N). The 4.3 µm band sounds the altitude range of about 60-95

km. Outside these bounds, the temperature weighting functions become very small, and retrieved temperatures tend to follow the initial profiles. Their proper specification is very important, therefore, since radiation flux calculations extend over the entire altitude range from the surface up to 140 km including ranges where temperature retrievals from IR and other measurements are not possible and other than VIRA profiles are not available. It will be shown in Section 5.3.1 that especially cooling rate results strongly depend on atmospheric thermal structure.

Two different Venus International Reference Atmosphere (VIRA) models exist at present, the basic version VIRA-1 (Seiff et al., 1985) and an updated version VIRA-2 (Zasova et al., 2006). The notation VIRA-2 was originally introduced by Moroz and Zasova (1997). It was therefore maintained in previous publications by the present authors (Haus et al., 2013a; 2014a; 2015) and is also used here. But note that the notations 'VIRA-1' and 'VIRA-2' are not very common in other papers related to the Venus atmosphere. VIRA-1 was compiled in 1982-1983 and published in 1985. It considers data from early US and USSR Venus missions and (for that time) latest results from the Pioneer Venus mission 1978. VIRA-2 summarizes measurement results from missions that had been completed after the early work on VIRA-1. It includes results from infrared thermal soundings performed by Venera-15 (1983), the Vega 2 entry probes (1985), and Galileo NIMS (1990) as well as radio occultation profiles from Venera-15/16 and Magellan (1990) data. VIRA-2 provides latitude and local time dependent temperature profiles at altitudes between 50 and 100 km.

To calculate initial temperature structure models that are required to operate the retrieval procedures with respect to VIRTIS data, VIRA-2 data have been first averaged over solar longitude (local time) to produce purely latitude-dependent temperature altitude profiles. Below 40 km, the VIRA-1 profiles are used, which are local time averages from the outset. Profiles between 40 and 50 km are obtained by linear interpolation between both models. Initial profiles above 90 km result from a linear interpolation between the latitude-dependent VIRA-2 temperatures at 90 km and a fixed value of 165 K at 100 km. A latitude-independent linear profile then extends to 140 K at 140 km altitude. This is the so-called 'VIRA-N' initial temperature distribution model for the Venus nightside as presented by Haus et al. (2013a). In this article, the authors have assumed that atmospheric temperatures at fixed latitude and averaged over local time on the day- and nightside of Venus below about 95 km are not expected to be very different (cf. Fig. 07 therein, $\Delta T < 2$ K between 60 and 95 km), as it was measured by the Pioneer Venus probes in 1978 (Seiff and Kirk, 1982) and confirmed by 2006 radio-occultation data (VeRa, Tellmann et al., 2009). It must be mentioned, however, that individual local time-dependent profiles may show significant deviations from averaged ones (e.g. at the cold collar at late night).

Above about 95 km, where the VIRA-1, VIRA-2, and VIRA-N profiles converge to about 170 K, the temperatures on the day- and nightside of Venus start to diverge. They change towards very different thermospheric temperatures with differences up to 200 K (Keating et al., 1980; Seiff and Kirk, 1982). For present flux calculations, the top of the atmosphere (TOA) is set to an altitude of 140 km to avoid discontinuities at 100 km (the assumed upper boundary of Venus' mesosphere). A latitude-independent dayside temperature profile is used between 100 and 140 km that corresponds to Table 4-16 published by Keating et al. (1985). Linear interpolations connect the VIRA-N nightside model at 95 km with this data set to construct the day time profile ('VIRA-D').

Remote sensing of temperature fields in the lower atmosphere down to the surface of Venus was never performed till now. Thermal infrared channels (15 µm, 4.3 µm) are not sensitive to the tropospheric temperature structure below about 55-60 km. *In situ* measurements were mainly restricted to equatorial regions up to about ±30° latitude (Seiff et al., 1980; Avduevsky et al., 1983;

Linkin et al., 1987). VIRA-1 provides partially extrapolated data between 40 and 32 km. Below 32 km, all VIRA-1 temperatures are given as latitude independent values, i.e. temperatures at a certain altitude are assumed to be constant all over the planet. This structure is preserved in the initial VIRA-N and -D profiles. Corresponding pressure values are determined from the barometric formula using a mean surface pressure of 92.1 bar at zero elevation.

It was shown by Haus et al. (2014a) that differences between VIRA-N temperature profiles and temperature profiles retrieved from VIRTIS-M-IR data are usually not larger than the observed temperature variability of VIRTIS results. This is a good argument for using VIRA-N profiles in basic studies on radiative energy balance variability.

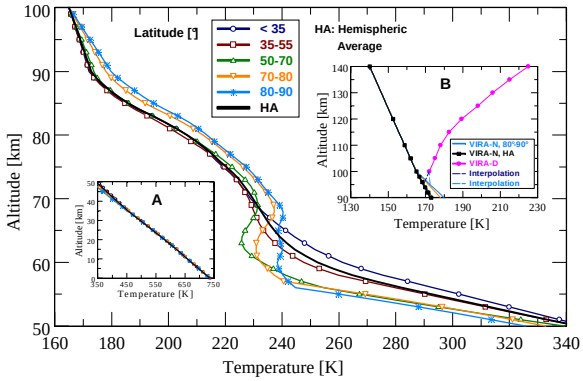

Figure 4. Initial nightside temperature model between 50 and 100 km merged from VIRA-1 and VIRA-2 data (VIRA-N). Inset A: Lower atmosphere (0-50 km), inset B: upper atmosphere (90-140 km) including an average dayside profile.

Fig. 4 illustrates zonal averages of VIRA-N temperature altitude profiles for five latitudinal belts. The two principal temperature domains at low and high altitudes are separated by cells of colder air that are located at latitudes between 50 and 80° and altitudes between 58 and 68 km. They form the well-known 'cold collar' region. The HA curve is the hemispheric average temperature profile where the latitude (φ)-dependent zonal averages are weighted by cos φ. $T_{HA}(z)$ is regarded as a representative temperature profile for the atmosphere of Venus that will be sometimes used in Section 5.3 to investigate the variability of fluxes and heating rates due to changes of other atmospheric input data or spectroscopic data. For completeness, the two insets in Fig. 4 illustrate the above discussed thermal structure below 50 km (display A) and above 90 km (display B). The latter shows the assumed latitude-independent night and day profiles.

2.4.2. Atmospheric composition

The atmosphere of Venus mainly consists of carbon dioxide (96.5 % by volume) and nitrogen (3.5 %) and accommodates water vapor (H_2O), carbon monoxide (CO), sulfur dioxide (SO_2), carbonyl sulfide (OCS), and hydrogen halides (HCl, HF) as the most important minor constituents. Fig. 5 shows altitude distributions of initial minor gas abundances that essentially correspond to those given by Tsang et al. (2008).

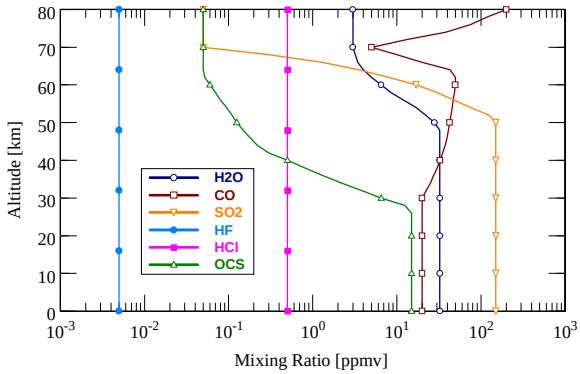

Figure 5. Initial model of minor gas abundance distributions with altitude.

The main gaseous constituent CO_2 has a vertically uniform volume mixing ratio of $9.65 \cdot 10^5$ ppmv. H_2O and SO_2 are assumed to be uniformly mixed in the lower atmosphere below 50 km with volume mixing ratios of 32.5 and 150 ppmv, respectively. CO and OCS are modeled to have a constant mixing ratio of 20 and 15 ppmv below about 30 km. While CO abundance increases to about 50 ppmv at 60 km, OCS abundance quickly drops down to 0.05 ppmv at this altitude. CO enhancement at altitudes above 70 km is due to the photolysis of CO_2 by UV radiation above the cloud tops. HCl and HF are assumed to be uniformly mixed with mixing ratios of 500 and 5 ppbv, respectively. The HDO abundance is considered as 150 times the telluric one (de Bergh et al., 1991).

Atmospheric minor gas abundances for CO, OCS, and H_2O have been recently retrieved from measured VIRTIS-M-IR spectra in the 2.3 µm transparency window in the southern hemisphere of Venus (Haus et al., 2015). It was found that hemispheric averages for H_2O and CO abundances very well correspond to the initial model assumptions at least at altitudes around 35 km where the retrieval results are primarily valid. Maximum H_2O and CO deviations from the hemispheric averages do not exceed 10 and 25%, respectively. The hemispheric average of OCS abundance near 35 km is slightly lower than the initial value (15%), and maximum deviations reach 35%. SO_2 abundances cannot be retrieved from VIRTIS-M-IR spectra. A constant value of (130 ± 50) ppmv was suggested for modeling purposes at altitudes below 50 km (in agreement with Bézard and de Bergh (2007), Tsang et al. (2008), and Marcq et al. (2008)) that is about 15% smaller than the value shown in Fig. 5.

Present studies on radiative energy balance variability use the initial gas abundances model except for OCS and SO_2. These two initial abundance profiles are multiplied by a factor of 0.85 in all calculations. It will be shown in Section 5.3.2, however, that actual minor gas vertical profiles and column abundances have little influence on the calculated atmospheric temperature change rates. This supports the use of the above defined initial model without going into further details at this point.

The clouds of Venus are usually assumed to be composed of four particle size modes that consist of 75 wt% spherical H_2SO_4 aerosols (e.g. Pollack et al., 1993; Zasova et al., 2007; Tsang et al., 2008; Haus and Arnold, 2010; Haus et al., 2013a, 2014a, 2015). Different models of cloud particle distributions with altitude can be found in the literature (e.g. Zasova et al., 1985; Lee, 2012). Detailed studies on the influence of particle mode abundances and altitude distributions on simulated spectra in comparison with measured VIRTIS data and Venera-15 Fourier spectrometer data have been performed by Haus et al. (2013a). Referring to their Fig. 26, the authors found that the measurements in both the 4.3 µm and 15 µm band regions are nearly equally well fitted by several mode 2 altitude distributions, since occurring differences in brightness temperatures are compensated by changes in retrieved temperature profiles and cloud parameters. Since there is no 'absolute truth' information available, it was not possible to specify a 'best choice' initial model. But it was stated that the selected initial cloud model is among the best existing initial mode distribution models that can be specified from the interpretation of remote sensing radiation measurements.

The initial model of cloud particle distributions with altitude that is adapted from the paper of Haus et al. (2013a) is shown in Fig. 6. Supplemental information is given in Tables 1 and 2.

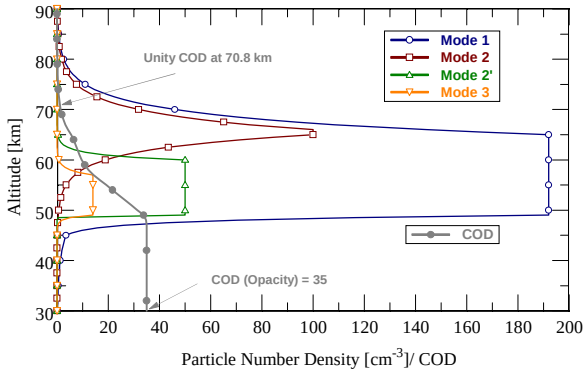

Figure 6. Initial model of cloud particle distribution with altitude. COD is the cumulative optical depth.

Some minor changes occur compared with Table 2 in the above reference. The upper scale height of mode 1 is now the same as for mode 2 below 80 km (3.5 km). At higher altitudes, a reduced upper scale height of 2 km is assumed for both modes to reduce 'distant wing' influences here. A lower haze is added below 45 km consisting of mode 1 particles. To maintain the nominal opacity of the cloud deck, the mode 1 peak concentration is also slightly varied. An advantage of this model consists in the possibility to describe cloud particle distributions of all four modes by simple analytical expressions (see Eq. (T1) in the footnote of Table 1). Fig. 6 also displays the cumulative cloud optical depth (COD) at 1 µm that was calculated using H_2SO_4 microphysical parameters of the four modes

described later on in Section 2.6. Unity COD is reached at 70.8 km, and the total column optical depth (nominal opacity) for this initial cloud model is 35.00 at 1 µm. The altitude of unity optical depth is usually denoted as 'cloud top altitude z_t'. Since aerosol microphysical parameters are functions of wavelength according to their refractive index specifics, any optical depth and cloud top altitude results have to be referenced to one wavelength (1 µm here). Note that z_t in Table 2 only slightly varies shortward of 1 µm.

Table 1. Parameters of the initial cloud model: single mode characteristics.

Mode	1	2	2'	3
Lower base of peak altitude z_b [km]	49.0	65.0	49.0	49.0
Layer thickness of constant peak particle number z_c [km]	16.0	1.0	11.0	8.0
Upper scale height H_{up} [km]	3.5[a,b]	3.5[a,b]	1.0	1.0
Lower scale height H_{lo} [km]	1.0[c]	3.0	0.1	0.5
Particle number density N_0 at z_b [cm^{-3}][d,b]	193.5	100	50	14
Total column particle number density [cm^{-2}][b]	3982.04	748.54	613.71	133.86
Total column optical depth (COD, opacity) at 1 µm[e,b]	3.88	7.62	9.35	14.14
Altitude of unity optical depth z_t [km] at 1 µm[e,b]	63.19	70.36	59.71	57.50

[a] An upper scale height of 2 km is assumed above 80 km.
[b] These values may change with latitude as retrieved by Haus et al. (2013a; 2014a).
[c] A lower haze is considered below 45 km using H_{lo}=5 km.
[d] The particle number density altitude profile N(z) is calculated according to

$$N(z) = \begin{cases} N_0(z_b)\exp\left[-(z-(z_b+z_c))\ /\ H_{up}\right], & z > (z_b+z_c) \\ N_0(z_b), & (z_b+z_c) \geq z \geq z_b \\ N_0(z_b)\ \exp\left[-(z_b-z)\ /\ H_{lo}\right], & z < z_b \end{cases} \quad \text{(T1)}$$

[e] The total cloud ensemble yields COD=35.0 and z_t= 70.91 km (cf. Table 2).

Table 2. Parameters of the initial cloud model: Opacity (COD) and cloud top altitude (z_t [km]) at different wavelengths λ [µm] and wavenumbers υ [cm^{-1}], respectively.

λ	10	5	2.5	1.5	1.0	0.55	0.35	0.2
υ	1000	2000	4000	6667	10000	18182	28570	50000
COD	28.34	25.59	32.09	39.95	35.00	34.72	33.17	31.84
z_t	66.56	66.39	68.93	71.33	70.81	70.45	70.23	70.04

Latitude-dependent cloud parameter variations have been retrieved from VIRTIS-M-IR data by Haus et al. (2013a; 2014a) by use of so-called cloud mode factors MF_j that change the densities independently for each cloud mode j, but maintain their altitude distribution that is determined by the initial cloud model. The retrieval scheme has used an additional parameter, the cloud upper altitude boundary z_{up} (no cloud particles above that level). Together, retrieved values for mode factors $MF_{1,2}$ and z_{up} define the actual cloud top altitude z_t. All these parameters were found to vary with latitude. This is the reason why present studies on radiative forcing variability with cloud features do not use these retrieved values. Instead, more specific investigations of responses to distinct parameter changes are performed (see Section 5.3.3). The full set of actually retrieved cloud parameters will be considered however in near future in the announced subsequent paper.

It is important here to mention that VIRTIS-M-IR data in the infrared are not sensitive to mode 1 particle abundance distributions with altitude. Mode 1 and 2 factors have been determined as an ensemble ($MF_{1,2}$) in the above mentioned retrieval procedures, therefore. But mode 1 extinction cross-sections are about 10-100 times larger in the visible and UV spectral range compared with infrared wavelengths. The retrieved mode factors MF_1 should not be used prior to further

sensitivity studies, therefore. This is the main reason why the suggested new model for the UV absorber (see Section 3) does not rely on absorption and altitude distribution modifications of mode 1 particles as it was often done in the literature, but comes up as an entirely synthetic model with respect to absorption properties.

2.5. Atmospheric absorption and scattering by gaseous constituents

2.5.1. Line absorption in the infrared spectral range (0.7-1000 µm)

Energetic transitions in polyatomic gaseous constituents in the infrared spectral range take place between different vibrational and rotational states and can form millions of spectral lines. Each line of a certain isotopologue can be described by parameters like spectral position of the line center, line strength and half-width at a defined reference temperature and pressure level, energy of the lower state of a transition, and others. These parameters are summarized in spectral line databases that always refer to wavenumber υ in units of [cm^{-1}]. They are used in numerical line-by-line procedures (Haus and Arnold, 2010) to calculate quasi-monochromatic absorption cross-sections $\sigma(\upsilon,p,T)$ in units of [$cm^2 molec^{-1}$].

The shapes of absorption cross-section spectral profiles and resulting radiance spectra depend on the chosen database of line parameters as it was shown for CO_2 by Haus and Arnold (2010). Optimum fits of measured VIRTIS-M-IR spectra could only be obtained in that work by use of spectroscopic line parameters for CO_2 that were ultimately taken from both the HITEMP-Venus database ("HOT-CO2", Pollack et al., 1993) and the high-temperature carbon dioxide spectroscopic databank (CDSD) compiled by Tashkun et al. (2003). The old HITEMP-Earth database (Rothman et al., 1995) and also the latest versions of HITRAN and HITEMP-Earth (HITRAN 2008, Rothman et al., 2009; HITEMP 2010, Rothman et al., 2010) contain some gaps in the CO_2 line lists mainly near 8500 and 10000 cm^{-1}. These spectral ranges however are very important to simulate observed nightside radiance signatures of Venus' lower atmosphere and surface. The transparency windows at 1.18, 1.10, and 1.02 µm have been utilized to retrieve the surface emissivity of Venus (Kappel, 2014; Kappel et al., 2015a; 2015b). On the other hand, contributions of any transparency window to the radiative energy balance of Venus' atmosphere can be safely neglected, since it is a spectral range of particularly low CO_2 absorption. Moreover, it will be shown in Section 5.2.1 that infrared absorption bands shortward of about 1.25 µm contribute only little to the solar heating of the atmosphere. Thermal components can be neglected anyway at these wavelengths.

The HITRAN 2008 line database is selected as reference for present investigations. A line strength cut-off 10^{-28} cm^{-1} is applied for all constituents except of CO_2 (10^{-35} cm^{-1}). Data on H_2O and CO line broadening by CO_2 are taken from Delaye et al. (1989) and Hartmann et al. (1988), respectively. A Voigt line profile is considered as the basic line form factor. Laboratory measurements, however, have indicated that gaseous absorption far from a spectral line center is often less than that predicted by a Voigt profile. It is common practice to model the line shape as the product of a Lorentz or Voigt profile and a function χ that describes the deviation from the Voigt structure beyond a defined distance from the line center (e.g. Pollack et al., 1993). With χ=1, the line shape reduces to the Voigt shape. Different χ-factors were derived in the literature by fitting laboratory data (e.g. Burch et al., 1969; Fukabori et al., 1986; Perrin and Hartmann, 1989; Tonkov et al., 1996) or Earth-based high resolution spectra of Venus' nightside (Bézard et al., 1990; de Bergh et al., 1995). The present reference absorption cross-section compilation for CO_2 uses sub-Lorentz profiles according to Tonkov et al. (1996) over the entire spectral range. Contributions from distant line wings are neglected beyond 125 cm^{-1} (see Section 5.2.3, line cut). Additional computations are carried out however using other sub-Lorentz profiles or even pure Voigt profiles (see Section 5.2.3, line shapes). A possible sub-Lorentz behavior of minor

constituent spectral lines is not considered here, but it will not significantly modify resulting total optical depths due to the low minor gas abundances compared with CO_2. Using the above described data and parameters, look-up tables of gaseous absorption cross-sections $\sigma(\upsilon,p,T)$ are generated for a variety of temperature (T) and pressure (p) values being representative for Venus' atmosphere at altitude levels from the surface up to 140 km.

Fig. 7 shows absorption cross-sections $\sigma(\upsilon,p,T)$ of CO_2 at 70 km altitude (p=34 mb, T=228 K). The spectra are plotted on a logarithmic scale where log denotes the base 10 logarithm and at a spectral wavenumber grid of 1 cm^{-1} in the range 10-14000 cm^{-1} (0.714-1000 µm). The use of wavenumber υ as independent variable (which is also the basic quantity in the line databases) is more convenient here for graphical representation of spectra compared with wavelength λ. The most important single absorption bands are highlighted in the figure. The dominant bands are located at 15, 4.3, 2.7, 2.0, 1.58, and 1.44 µm.

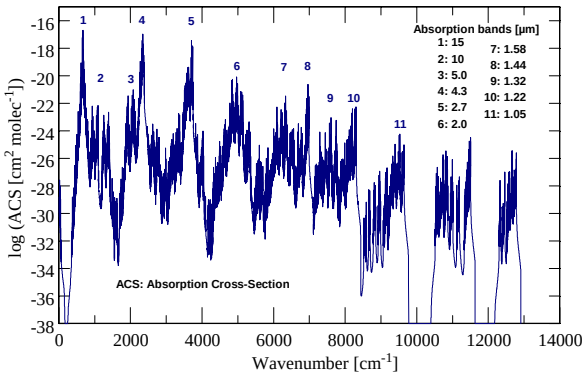

Figure 7. Absorption cross-sections of CO_2 at 70 km altitude as function of wavenumber. The most important individual absorption bands are indicated by numbers.

Figs. 8 and 9 illustrate the spectral behavior of individual gas optical depths (cf. Eq. (3)) of a 1 km thick atmospheric layer centered around 70 km. The initial minor gas abundances shown in Fig. 5 are used here. 70 km is the approximate altitude where the Venus cloud top is observed in low and mid latitudes. It is of special interest in atmospheric investigations, therefore. Since individual optical depths include the abundance of the corresponding constituent, the figures are not only useful to visualize the gas band regions, but also to determine their approximate contribution to the total optical depth of a layer, and thus to estimate the role of different gaseous absorption bands in energetics. The horizontal broken line in each display marks the optical depth of 10^{-4}. This is the approximate lower threshold below which the contributions of individual bands to the wavenumber integrated radiative fluxes become negligible small at all altitudes. This was thoroughly investigated when calculating atmospheric radiative fluxes and temperature change rates. Note that optical depths of different constituents including clouds are additive, while resulting radiances and fluxes are not. The most important H_2O bands are located at 40 µm (pure rotational band), 6.3, 2.7, 1.87, and 1.38 µm. CO can slightly contribute to the energy balance around 4.7 µm (2130 cm^{-1}). SO_2, OCS, HF, and HCl (in the infrared) should play a minor role from the energetics point of view.

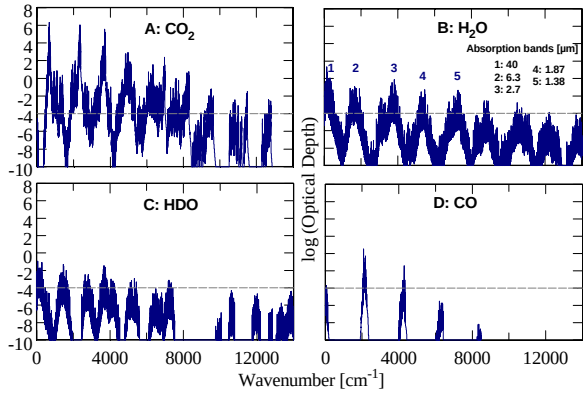

Figure 8. Individual gas optical depths of CO_2, H_2O, HDO, and CO of a 1 km thick atmospheric layer at 70 km as functions of wavenumber. Display B indicates the most important individual absorption bands of water vapor.

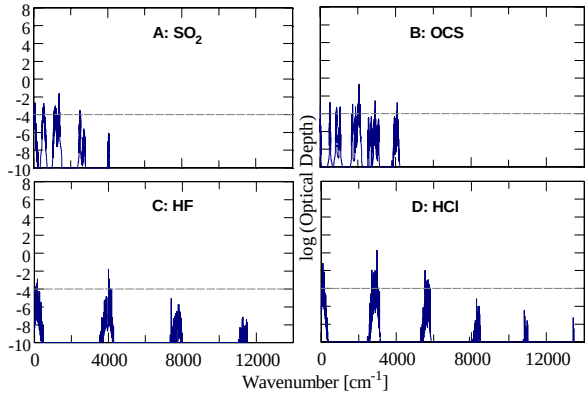

Figure 9. Same as Fig. 8, but for SO_2, OCS, HF, and HCl.

Fig. 10 shows altitude profiles of 1 km thick layer optical depths for CO_2 at different wavenumbers that belong to the stated band systems. It becomes clear that the 15 and 4.3 µm CO_2 bands will strongly contribute to radiative fluxes even at altitudes around 100 km. Since the plot only shows optical depths for one single wavenumber, it can be expected that the weaker 2.0 µm band is also very important for the mesospheric radiative energy balance, while the 1.05 µm band (as an example for very weak bands) will only add a few percent of heating near the mesopause.

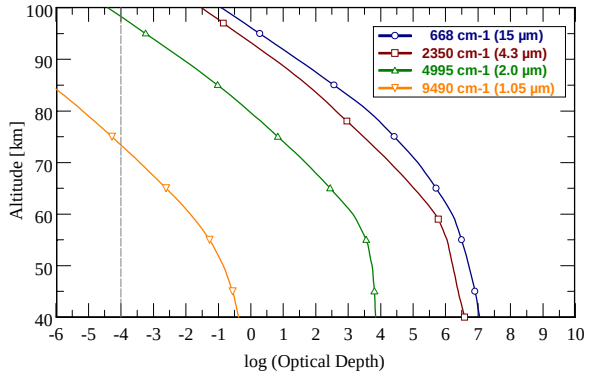

Figure 10. Altitude profiles of 1 km thick layer optical depths for CO_2 at different individual wavenumbers that belong to the band systems indicated in the box.

2.5.2. Line and band absorption in the visible and UV spectral range (0.1-0.7 µm)

Water vapor is the only gaseous species in the visible spectral range (400-700 nm) that is represented by single line data in the HITRAN catalogs (except of molecular oxygen, which does not play a role in Venus' mesospheric energetics). The main isotopologue ($^1H^{16}O^1H$) strongly dominates. H_2O optical depths at 70 km for a 1 km thick layer do not exceed a value of about 10^{-5} (the approximate depth near 14000 cm^{-1} as shown in Fig. 8B). They decrease down to values of about 10^{-8} near 25000 cm^{-1} (0.4 µm). Although a large portion of solar irradiance is received at these wavenumbers (cf. Fig. 3), H_2O at visible wavelengths will not play a significant role in the radiative energy balance.

Energy transitions in the UV take mostly place between different electronic states of molecules and atoms. It is difficult to calculate the corresponding transition parameters and present them in the form of line catalogs as it is the standard in the infrared and visible range, because practically all absorption results in dissociation of the molecule. Thus, UV absorption cross-sections are usually measured in laboratory experiments.

Molecules of CO_2, H_2O, OCS, and HCl exhibit UV spectra in the far (122-200 nm) and partly middle (200-300 nm) UV ranges, while SO_2 absorption extends to the near UV range (300-400 nm). Fig. 11 shows measured UV absorption cross-sections of CO_2, H_2O, OCS, HCl (display A), and SO_2 (display B) as functions of wavelength. The spectral range 100-400 nm corresponds to 25000-100000 cm^{-1}. CO_2 cross-sections were measured at 298 K by Thompson et al. (1963) [A] and Shemansky (1972) [B]. They are in good agreement with more recent data reported by Parkinson et al. (2003). H_2O data (298 K) are taken from Watanabe and Zelikoff (1953) [C], and Thompson et al. (1963) [A]. OCS (295 K) and HCl (298 K) data are based on Molina et al. (1981) [D] and Inn (1975) [E], respectively. Many laboratory experiments to measure SO_2 absorption cross-sections were performed by different authors. Display B provides a selection of seven results, reported by Sidebottom et al. (1972) [A], Thompson et al. (1975) [B], Vandaele et al. (2009) [C], Warneck et al. (1964) [D], Wu et al. (2000) [E], Manatt and Lane (1993) [F], and Crisp (1986) [G]. Most spectra were measured at 298 K (except for F: 293 K).

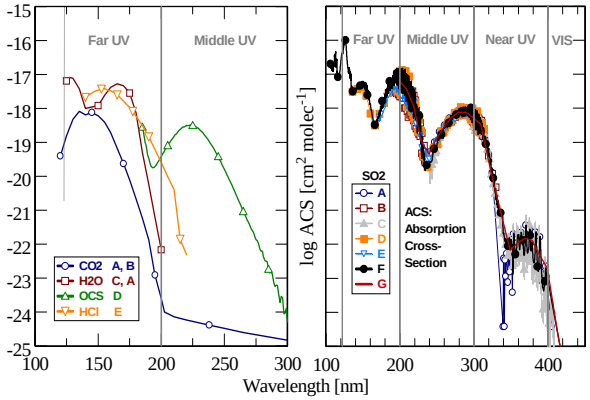

Figure 11. Measured UV absorption cross-sections of CO_2, H_2O, OCS, HCl (display A, references A-E), and SO_2 (display B, references A-G) as functions of wavelength. References see text.

Strongest UV absorptions generally occur in the far UV shortward of 200 nm. The cross-sections are in the order of the strongest CO_2 cross-sections at infrared wavelengths. The UV cross-sections quickly decrease toward longer wavelengths except for OCS, which shows a secondary local maximum at 225 nm. SO_2 has an additional absorption maximum near 300 nm. Molecular nitrogen (N_2), which is the second abundant molecular species on Venus (3.5%) after CO_2, cannot play a role in the energy balance, since the observed absorption bands occur in the XUV spectral range between 11 and 200 eV (6.2-113 nm) (Chan et al, 1993) where the portion of incident solar radiation is negligibly small (cf. Fig. 2a).

Fig. 12 illustrates individual gaseous UV absorber optical depths of a 1 km thick atmospheric layer centered at 70 km as functions of wavelength and wavenumber. SO_2 data are taken from Manatt and Lane (1993). The spectral distance of data points is determined by the different measurements. Note that the symbols do not indicate all available data points. Initial minor gas abundances according to Fig. 5 are used. Referring to the statement given above that layer optical depths smaller than 10^{-4} will not significantly contribute to the radiative energy balance, the spectral range 100-320 nm (υ>31250 cm^{-1}) is of special importance. On the other hand, the solar irradiance shortward of 200 nm becomes very small, and the influence of far UV absorption on the radiative energy balance is not predictable at this point. This will be investigated in Section 5.1.

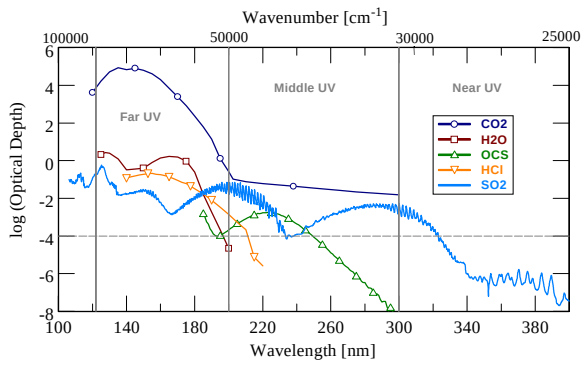

Figure12. Gaseous UV absorber optical depths of a 1 km thick atmospheric layer at 70 km as functions of wavelength and wavenumber.

2.5.3. Continuum absorption in the infrared

A generally accepted definition of continuum absorption has not been established in the literature, and there are different approaches to consider this effect while calculating gaseous absorption cross-sections. The infrared continuum at a certain wavenumber is mainly due to the influence of distant line wings from strong absorption bands. It is therefore connected to the specific form of the line shape factor that determines the absorption contributions away from the main line centers. The contribution of line wing continua can be investigated by calculation of absorption cross-sections σ for different line cut conditions υ_c in the line-by-line procedures.

Fig. 13 illustrates the changes of CO_2 absorption cross-sections σ in the vicinity of the strong 2.0 and 2.7 µm bands and at 70 km altitude in dependence on line cut condition υ_c and sub-Lorentz line shape factor. υ_c = 125 cm^{-1} is the default line cut condition, and the Tonkov profile (Tonkov et al., 1996) is the default line shape factor. The curves are plotted for a wavenumber grid of 1.0 cm^{-1}.

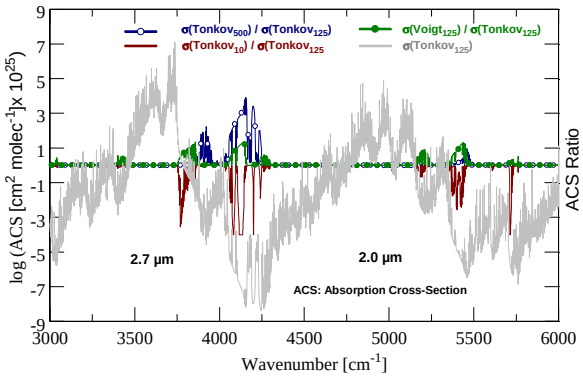

Figure 13. Influence of line cut condition and sub-Lorentz line shape factor on CO_2 absorption cross-sections (ACS) in the vicinity of the strong 2.0 and 2.7 µm bands at 70 km altitude. The thick lines describe ACS ratios, the basic ACS curve (cf. Fig. 7) is represented by the thin line.

Distant line wing contributions are characterized comparing the ratio of results for υ_c = 500 and 125 cm^{-1} and using the Tonkov profile ($\sigma(Tonkov_{500})$ / $\sigma(Tonkov_{125})$). It was verified that σ does no longer change for υ_c > 500 cm^{-1}. The main ratio differences in the spectra are located in the ranges 3750-4250 cm^{-1} and near 5400 cm^{-1}. It can be stated that

the line cut condition is not very important for energetics purposes at least in the middle and upper mesosphere of Venus, since it does not influence the center regions of the main bands. Even when the value υ_c = 10 cm^{-1} is applied, the center cross-sections remain unchanged. But to be on the safe side, the default υ_c value should be maintained. The figure confirms that the band centers are also not very sensitive to the choice of the specific sub-Lorentz profile ($\sigma(Voigt_{125})$ / $\sigma(Tonkov_{125})$). Even using the pure Voigt profile does not strongly change the absorption cross-sections at 70 km compared with the default Tonkov profile. Since this discussion is only performed for one defined altitude, the corresponding responses of temperature change rates over the entire altitude range will be studied in Section 5.2.3.

There is an additional significant continuum absorption in high pressure environments. The probability of molecular collisions dictates the strength of this effect, and hence, it is a function of the square of number density of the gas (predominantly CO_2 in this case). This pressure-induced continuum absorption plays an important role in the deep atmosphere of Venus below about 45 km, but can be neglected at higher altitudes. Thus, its consideration is especially important when lower atmosphere and surface features (cloud parameters, minor gas abundances, surface emissivity) are retrieved from measured radiance spectra (Haus et al., 2013a; 2014a; 2015; Kappel et al., 2015a; 2015b). The continuum parameters for the atmospheric transparency windows located between 1.0 and 2.4 µm have been retrieved from VIRTIS-M-IR data (Kappel et al., 2012; 2015b) using the multi-spectrum retrieval algorithm MSR (Kappel, 2014). Continuum absorption in the 1.10 and 1.18 µm windows was also determined by Bézard et al. (2009; 2011) using both VIRTIS-M-IR and SPICAV-IR spectral measurements. But these continuum parameters cannot be retrieved outside the transparency windows, and there is no information on pressure induced continuum influence over wide spectral ranges. From the above discussion with respect to the wing continua and line shape factor influences it can be concluded, however, that the lower atmosphere continuum absorption does not alter the radiative energy regime at any altitude. This was verified by corresponding tests.

2.5.4. Rayleigh scattering

The scattering of radiation by gaseous constituents (Rayleigh scattering) is inversely proportional to the fourth power of wavelength. Assuming a pure CO_2 atmosphere, Hansen and Travis (1974) have derived an expression that relates the total atmospheric Rayleigh optical depth u_{R0} above the surface of Venus to wavelength [µm] in the form

$$u_{R0} = 1.527\,\lambda^{-4}\,(1 + 0.013\,\lambda^{-2})\,. \qquad (9)$$

It is connected with the cumulative atmospheric optical depth above pressure level p(z) by

$$u_R(z) = u_{R0}\,p(z)/p_0 \qquad (10)$$

where p_0 is the Venus surface pressure. Note that z denotes the base altitude of the vertical column. Hansen and Travis have assumed a p_0 value of 93 p_0^{Earth} with p_0^{Earth} = 1.01325 bar. Present calculations use a Venus zero-altitude surface pressure of 92.1 bar according to VIRA. Thus, Eq. (9) takes the slightly corrected form

$$u_{R0} = 1.492\,\lambda^{-4}\,(1 + 0.013\,\lambda^{-2})\,. \qquad (11)$$

The Rayleigh optical depth of a single 1 km thick layer centered at level z is obtained from the difference between the two adjacent layer values. Fig. 14 illustrates the spectral behavior of Rayleigh layer optical depths at 50 and 70 km as functions of wavenumber and wavelength. Rayleigh scattering at 70 km will be only effective shortward of about 1 µm, but becomes more important at lower altitudes even for longer wavelengths. The overall influence of Rayleigh scattering on the radiative energy budget is comparatively small however as will be shown in Section 5.1.

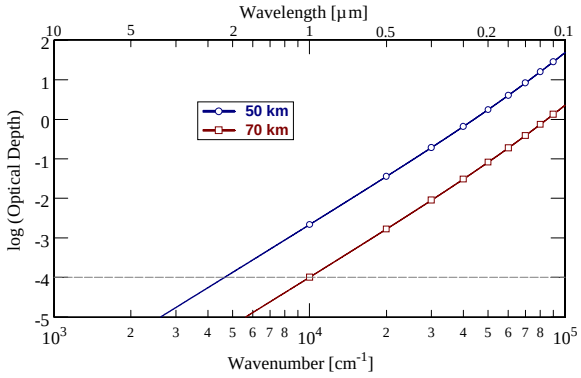

Figure 14. Optical depths of a 1 km thick Rayleigh scattering atmospheric layer at 70 and 50 km as functions of wavenumber and wavelength.

2.6. Atmospheric absorption and scattering by particulate constituents

There is strong evidence from spectroscopic and polarimetric measurements that the chemical composition of the intermediate size (mode 2) particles corresponds to concentrated liquid sulfuric acid (75-85% H_2SO_4 by weight). Otherwise, the good coincidence of observed Venera-15 FS infrared radiation spectra and synthetic spectra that make use of this composition scheme would be impossible (Esposito et al., 1997). But the nature of small mode 1 and especially large mode 3 droplets is still controversially discussed (e.g. Crisp and Titov, 1997; Taylor, 2006). The large mode could have a completely different composition, like sulfur crystals or other. Nevertheless, the chemical composition of mode 2 is carried over to the other modes in most radiative transfer simulation models. H_2SO_4 clouds near the cloud top level (~70 km) are probably formed when H_2O and SO_2 (the latter presumably of volcanic origin) combine photochemically (James et al., 1997; Taylor, 2006), while condensation of a chemically stable sulfuric acid vapor on hydrated sulfuric acid particles may be responsible for their formation near the cloud bottom (~50 km). Investigations by Imamura and Hashimoto (1998, 2001) as well as recent numerical modeling by Parkinson et al. (2015) have indicated that the simulated cloud population is similar to the previously observed one.

The present radiative transfer simulation model uses a four-mode composition scheme and particle number density distributions that were already described in Section 2.4.2 (cf. Fig. 6). Mie scattering theory (Wiscombe, 1980) is applied to derive the wavelength-dependent microphysical parameters of H_2SO_4 aerosols like absorption, scattering, and extinction cross-sections as well as single scattering albedo, asymmetry parameter, and phase function. Log-normal size distributions are used for all four modes with modal radii of 0.3, 1.0, 1.4, 3.65 µm and unitless dispersions of 1.56, 1.29, 1.23, 1.28, respectively (Pollack et al., 1993). Refractive index data are taken from Palmer and Williams (1975). The authors supplied data for the 0.36-25 µm spectral range and H_2SO_4 solutions of 25, 38, 50, 75, 84.5, and 95.6% by weight at 300 K. Radiance and flux simulations in the thermal infrared require calculations up to 1000 µm. The corresponding refractive index data are partly taken from Jones (1976), who supplied measurements for a 75% solution for the 20-50 µm spectral range at 300 K. To merge the different data sources near 25 µm (400 cm^{-1}), Palmer-Williams refractive indices for different solutions are linearly interpolated from 25 µm up to the Jones value at 28.67 µm (260 cm^{-1}). Longward of 50 µm (<200 cm^{-1}), the Jones data are extrapolated up to 1000 µm (10 cm^{-1}). Shortward of 0.36 µm, refractive index data are assumed to be constant down to 0.1 µm. There is a gap in the Palmer-Williams imaginary index data between 1.8 and 2.9 µm (3450-5600 cm^{-1}), where the values for the six solutions drop down to zero. This leads to wrong radiance results in the 2.3 µm transparency window and may also influence flux calculations in the 2.0 and 2.7 µm CO_2 absorption bands. Carlson and Anderson (2011) have measured the imaginary index from 1.7 to 2.8 µm for concentrations of 68, 72, 76, 84, 88, 92, and 96 wt% at 295 K. Their results are integrated into a new complete refractive index database for H_2SO_4 aerosols as shown in inset B of Fig. 15.

Fig. 15 visualizes some microphysical parameters (scattering and extinction cross-sections (QS, QE), single scattering albedo ω_0) of cloud modes 2 and 3 as functions of

wavenumber. ω_0 is very close to unity longward of 6000 cm^{-1} (<1.67 µm) for cloud mode 3 and even almost unity longward of 5000 cm^{-1} (<2 µm) for cloud mode 2. Clouds then just scatter radiation and do not absorb it, that is, conservative scattering is the dominating feature of particulate constituents in this spectral range. This is the crucial precondition that radiation from the deep atmosphere and surface of Venus can penetrate the dense cloud layers in some narrow transparency windows between comparatively weak CO_2 and H_2O bands and is detectable by remote sensing instruments. H_2SO_4 absorption (characterized by the imaginary part of the refractive index) increases shortward of 4000 cm^{-1} (longward of 2.5 µm) and causes upwelling radiation to be trapped below the cloud deck. The clouds are very effective absorbers in the thermal infrared.

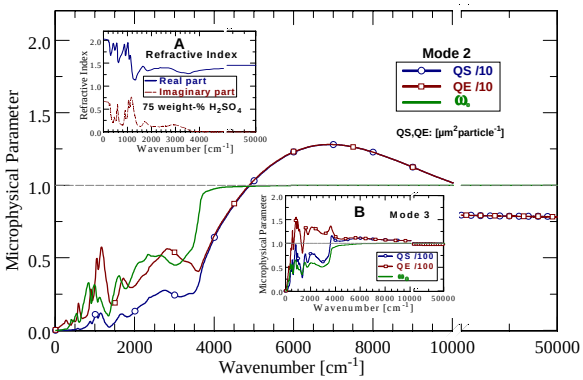

Figure 15. Microphysical parameters (scattering and extinction cross-sections (QS, QE), single scattering albedo ω_0) of cloud mode 2. Inset A: Refractive indices of a 75 weight-% solution of H_2SO_4. Inset B: Same as main display, but for cloud mode 3.

Layer optical depths of the single cloud modes are not shown here, but as an example, the 1 µm optical depth of mode 2 particles of a 1 km thick layer centered at 65 km is calculated. The initial mode 2 particle number density at 65 km is 100 cm^{-3} (cf. Fig. 6). The scattering cross-section at 1 µm, which is equal to the total extinction cross-section at 1 µm, is about 10 μm^2 $particle^{-1}$ (note that Fig. 15 shows QS/10). Thus, the 1 km layer optical depth at 65 km is about 1.0. This must not be confused with the cumulative optical depth of unity that defines the cloud top altitude. For pure mode 2 particles, it is reached at 70.46 km (cf. Table 1). A layer optical depth of unity exceeds the estimated influence threshold 10^{-4} by four orders of magnitude and will be consequently very effective with respect to radiative energy calculations.

3. TOA spectral radiation fluxes, the Bond albedo of Venus, and the unknown UV absorber

At the top of atmosphere (TOA), there are two flux components, the downward direct solar flux F^{Ddir} and the upward diffuse flux F^{Udif} that is composed of reflected solar and thermal radiation and the upward emitted thermal radiation from the underlying atmosphere. Based on the discussion in Section 2.2, the solar components can be determined without considering thermal emissions of the atmosphere. A separated calculation considers thermal emissions, but ignores the TOA insolation. A description of radiation flux components within the atmosphere is provided in Section 4. At this point, only TOA components are of interest. The top of the atmosphere is fixed at 140 km altitude. Downward diffuse fluxes are zero here.

Spectrally resolved thermal and solar radiances and fluxes that pass the TOA are displayed in Fig. 16. The following radiative transfer simulation model (RTM) parameters are utilized:

- solar irradiance spectrum of Kurucz (2011), Fig. 3,
- hemispheric average temperature profile (VIRA-N-HA), Fig. 4,
- standard minor gas abundance profiles, Fig. 5,
- gaseous absorption cross-section databases calculated from HITRAN 2008 using Tonkov line profiles with line cut at 125 cm^{-1}, Figs. 7-9,
- Rayleigh scattering, Fig. 14,
- standard cloud mode abundance profiles, Fig. 6,
- cloud mode microphysical parameters, Fig. 15,
- UV absorption by SO_2, CO_2, H_2O, OCS, HCl, Fig. 12,
- neglect of continuum absorption,
- neglect of the unknown UV absorber.

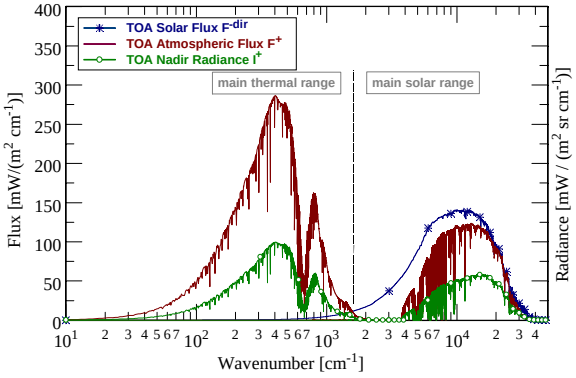

Figure 16. Solar radiation flux, thermal and solar diffuse upward fluxes, and thermal and solar upward radiances at nadir geometry at the top of Venus' atmosphere as functions of wavenumber.

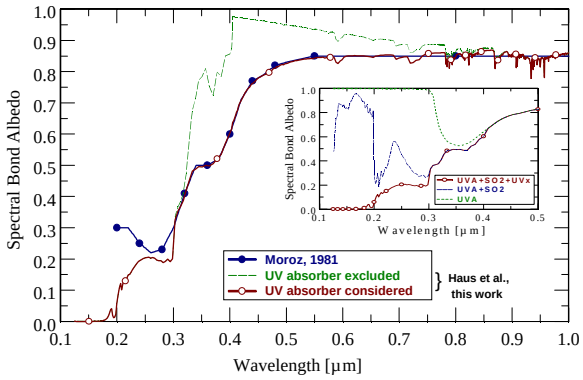

Figure 17. The spectral Bond albedo of Venus as a function of wavelength shortward of 1 µm. The inset illustrates albedo changes when UV_X (X: CO_2, H_2O, OCS, HCl) contributions and additionally SO_2 UV contributions are neglected.

Fluxes are shown for the subsolar point (θ_{Sun}=0°) that resides at the equator on Venus (see Section 4) and a comparatively coarse spectral grid step of 1 cm^{-1}. The radiance I^+ refers to nadir observation geometry (θ_{obs}=0°). The solar calculation extends over the spectral range 10-80000 cm^{-1} (0.125-1000 µm). The thermal calculation starts at 10 cm^{-1} (1000 µm) and terminates at 6000 cm^{-1} (~1.67 µm). There is little contribution beyond 3 µm, however. Apart from the striking feature of the CO_2 band centered at 668 cm^{-1} (15 µm), strong absorptions occur on the dayside between about 2000 and 10000 cm^{-1} (1-5 µm) that are also mainly due to CO_2 but also due to cloud and minor gas influences.

The ratio of total radiation flux reflected from a planet and total incident radiation flux from the Sun at TOA altitude and wavelength λ defines the spectral Bond (or spherical) albedo $A_B(\lambda)$. The total Bond albedo A_B^* is calculated according to

$$A_B^* = \frac{\int_0^\infty A_B(\lambda)\, F^{Ddir}(\lambda)\, d\lambda}{\int_0^\infty F^{Ddir}(\lambda)\, d\lambda} = \frac{\int_0^\infty F^{Udif}(\lambda)\, d\lambda}{\int_0^\infty F^{Ddir}(\lambda)\, d\lambda}. \quad (12)$$

When the spectral Bond albedo $A_B(\lambda)$ is determined from the flux spectra shown in Fig. 16, the upper broken line in Fig. 17 is obtained, which does not consider the unknown UV absorber according to the above specified RTM parameters.

Features of the spectral Bond albedo of Venus were described by Moroz (1981) and Moroz et al. (1985). The analyses were based on measurements of geometric albedo and phase functions carried out by different authors (e.g. Irvin, 1968; Barker et al., 1975). The resulting curve marked by dots is also shown in Fig. 17. Compared with the present initial simulation, there is a broad depression in the observed Bond albedo at wavelengths shortward of about 0.8 µm that becomes particularly striking in the visible and near UV range down to 0.32 µm and that cannot be explained by known absorption features of gases or clouds. Shortward of 0.32 µm, SO_2 UV absorption provides sufficient opacity to match the observed albedo features.

The composition and vertical distribution of the UV absorber is virtually not known, but Venera-13 and -14 as well as Pioneer Venus descending probe measurements have shown that it is confined to the upper cloud region between about 57 and 72 km (Ekonomov et al., 1983; Pollack et al., 1980; Tomasko et al., 1980; Crisp, 1986; Krasnopolsky 2006). A large part of solar radiation is absorbed here, and identification of this substance (or at least quantitative description of some proxy) is required due to its significant influence on the radiative energy balance. Changes in atmospheric structure and dynamics due to a non-uniform distribution of unknown absorber(s) (variations with respect to either geographic coordinates or altitude, or possibly both) were described as the cause of observed

ultraviolet markings in the clouds of Venus (Rossow et al., 1980; Pollack et al., 1980; Titov et al., 2008). These Y-shaped features in UV images of the planet are mostly short-lived but also quickly reappear.

The unknown UV absorber was modeled before by reducing the single scattering albedo of the mode 1 sufuric acid particles in the spectral range 310-780 nm (Crisp, 1986; Pollack et al., 1980), that is, as an impurity of mode 1 particles. This ensures that the optical properties of mode 1 particles at infrared wavelengths are not significantly altered. The impurity model was also supported by the observed correlation between the vertical distribution of the UV absorber and the mode 1 particles in the upper cloud (Crisp, 1986). Iron chloride ($FeCl_3$), elemental sulfur (S_8), metastable sulfur allotropes (S_3, S_4), sulfur dichloride (SCl_2), chlorine gas (Cl_2), disulfur monoxide (S_2O), and some other compounds are possible further candidates for the UV absorber (Toon et al., 1982; Esposito et al., 1997; Mills et al., 2007; Markiewicz et al., 2014), but their sources and sinks are unknown.

Present investigations introduce the additional opacity source in the following way. Two different hypothetical altitude profiles of the unknown absorber number density are defined that are illustrated in the inset of Fig. 18. As discussed above, the absorber may be either composed of aerosol particles or of gaseous molecules or solid atom conglomerates. It may be a mixture of all these agents as well. Therefore, the notation 'particle' in the abscissa caption is used as synonym for the agent's microphysical structure. The number density profile peaks at a constant value of either 10 cm^{-3} between 58 and 70 km (nominal model, case 1) or 20 cm^{-3} between 58 and 64 km (case 2). The use of a 'high and low UV absorber case' was originally proposed by Crisp (1986). The second case in present calculations assumes a twofold absorber peak concentration to partly compensate the halving of the peak width (see Table 3). Both profiles decrease with a scale height of 1 km above and below the bounds of constant particle number density defined above. The particle number density altitude profiles N(z) are calculated according to Eq. (T1) given in the footnote of Table 1. This equation can be also used for molecular agents replacing the notation 'particle' by 'molecule' wherever required.

Table 3. Parameters of the UV absorber vertical distribution.

Case	1: High altitude UV absorber (Nominal)	2: Low altitude UV absorber
Lower base of peak altitude z_b [km]	58	58
Layer thickness of constant peak particle number z_c [km]	12	6
Upper scale height H_{up} [km]	1	1
Lower scale height H_{lo} [km]	1	1
Particle number density N_0 at z_b [cm^{-3}]	10	20
Total column particle number density [cm^{-2}]	140.41	160.82
Total column optical depth (opacity) at 0.35 µm (maximum influence)[a]	0.205	0.410

[a] use of different absorption cross-section spectra for cases 1 and 2

Using these profiles, altitude-independent absorption cross-section spectra are calculated ('retrieved') that yield good fits of the Bond albedo spectrum presented by Moroz (1981). The spectral albedos resulting from the different absorber distributions but from the same spectral absorption cross-section profile are not the same, since interferences with other atmospheric constituents (mainly clouds and SO_2) cause different vertical flux profiles. Thus, the absorption spectrum of the unknown UV absorber has to be adjusted to produce the same spectral albedo. The final spectral albedo curve (line marked by empty circles) is shown in Fig. 17. Shortward of 0.3 µm, the depicted Moroz spectrum is an average over three very different measurement results. One of the data sources (Wallace et al., 1972) is fairly well comparable with present results. It shows a local reflectivity maximum near 250 nm,

smaller values at 270 nm, and a steep decrease shortward of 230 nm reaching zero near 180 nm. The absolute magnitude of the albedo shortward of 0.32 µm will not be able to significantly alter the total wavelength-integrated Bond albedo, however.

Integration of albedo values over the spectral range 0.125-1.0 µm according to Eq. (12) yields A_B=0.789 and A_B=0.788 (omitting the asterisk in the notation from here on) for the Moroz and the present spectrum, respectively. Integration of the present spectrum over the full solar range (0.125-1000 µm) and consideration of the globally averaged value (see Section 4) provides A_B^{Venus}= 0.763 in excellent agreement with Moroz et al. (1985). When the unknown UV absorber is neglected, a value of 0.824 is obtained. The visual Bond albedo at λ=0.55 µm is 0.84.

This way, the solar radiative effect of the unknown absorber can be adequately modeled regardless of its physical and chemical composition. This will be discussed in more detail in Section 5.3.4. The inset in Fig. 17 illustrates the albedo changes shortward of 0.5 µm when UV absorptions by CO_2, H_2O, OCS, and HCl (shortly denoted as UV_X absorbers in the following) and additionally SO_2 absorptions are neglected. In accordance with Fig. 12, UV_X absorptions (mainly due to CO_2) dominate shortward of 0.3 µm. The two SO_2 absorption maxima near 0.2 and 0.3 µm and the minimum near 0.23 µm are clearly discernible as minima and maximum of the albedo curves when UV_X contributions are neglected.

Fig. 18 finally displays the 'retrieved' absorption cross-sections σ(λ) of the UV absorber for the two discussed cases, and the inset shows the assumed initial particle altitude profiles N(z) as already discussed above. Recall that 'particle' is used as a synonym for the unknown absorbing agent. Consequently, this holds also true for the depicted unit of the absorption cross-section. Information on particle size distributions (as in case of cloud mode cross-sections) is not required here, since σ is 'retrieved' from the albedo measurement. Note that σ does not depend on altitude (that is, on temperature and pressure). The spectral shape of the UV absorber optical depth for a 1 km thick layer is not shown here (as done before for other constituents). A simple numerical description can serve as a proxy, however, to emphasize the high importance of the UV absorber for the energetics of Venus. The absorption maximum in the nominal model is located at 0.35 µm and reaches about 10^{-8} cm^2 $particle^{-1}$. The particle number density at 65 km is 10 cm^{-3}. Multiplication with a 10^5 cm thick atmospheric layer yields an optical depth of 10^{-2}. This is significantly less than optical depths in the centers of the CO_2 infrared bands (cf. Fig. 8), but considering the spectral range where the UV absorber is active, its large role in the radiative energy balance becomes clear.

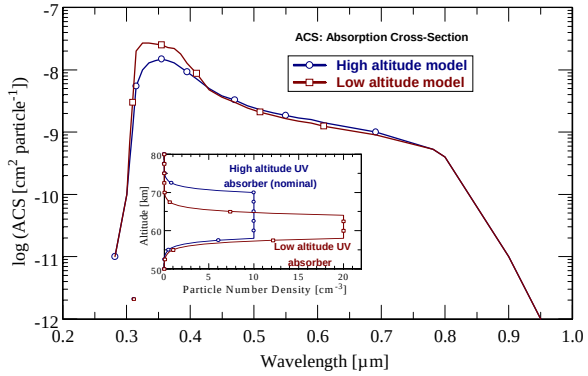

Figure 18. 'Retrieved' altitude-independent absorption cross-sections of the UV absorber as functions of wavelength. The inset shows two assumed initial absorbing agent distributions with altitude.

4. Radiation fluxes and radiative temperature change rates in the atmosphere

Inside the atmosphere, there are three 'solar flux components', the downward direct flux $F^-_{dir\,sol}$, the downward diffuse flux F^{-dif}_{sol}, and the upward (always diffuse) flux F^+_{sol}. The two downward components together determine the total downward flux F^-_{sol}. 'Thermal flux components' encompass the downward and upward diffuse fluxes F^-_{the} and F^+_{the}. The superscripts 'dif' and 'dir' can be omitted from the outset, since all thermal radiation is diffuse radiation.

The gain and loss of radiative energy in a distinct spectral interval Δλ (or Δυ) at each

atmospheric altitude level z, latitude φ, and local time t is determined by the divergence of the net flux $F^n_{\Delta\lambda}(z,\varphi,t)$. The net flux F^n is defined here as the difference between downward and upward fluxes,

$$F^n{}_{\Delta\lambda}(z,\varphi,t) = F^-{}_{\Delta\lambda}(z,\varphi,t) - F^+{}_{\Delta\lambda}(z,\varphi,t) \quad (13)$$

where

$$F^\pm{}_{\Delta\lambda}(z,\varphi,t) = \int_{\lambda_1}^{\lambda_2} F^\pm(\lambda,z,\varphi,t)\, d\lambda \ . \quad (14)$$

The notations F^+, F^-, and F^n refer to either solar or thermal radiation. $\Delta\lambda$ (or $\Delta\upsilon$) may span over the total solar and thermal spectral ranges or may cover certain defined spectral sub-intervals. Thermal emissions take place independently of local time, and the quantities $F^\pm_{the}$ do not depend on t as long as atmospheric parameters remain unchanged with local time. The calculation of solar fluxes $F^\pm_{sol}$ requires consideration of insolation changes. Insolation varies with geographic latitude, local time, and in the general case also with time of year. Although there are almost no seasonal changes on Venus, the following equations and discussions refer to the general case of application for any planet and not only for Venus as a very special case. They may thus serve as a reference for future works on planetary radiative energy balances.

Since temperature change rates are usually given in units of [K/day], it is common practice to define diurnal flux averages in the form

$$\bar{F}^{\pm}{}_{\Delta\lambda}(z,\varphi) = \frac{1}{T_R}\int_0^{T_R} F^\pm{}_{\Delta\lambda}(z,\varphi,\theta(t))\, dt \ . \quad (15)$$

T_R is the rotational period of the planet (the course of a full planetary day), and θ is the solar zenith angle (zero at zenith), which depends on local time. It is also denoted as Sun path angle in the literature, but then with reverse definition (zero at sunrise). A full day in Eq. (15) encompasses all day and night hours, that is, 24 hours on Earth. Although a full day on Venus is much longer than on Earth, the averaged fluxes $\bar{F}$ remain the same when referring to an Earth or Venus day. Eq. (15) can also be applied to determine averaged solar fluxes at any insolation condition (e.g. at the subsolar point) where θ is assumed to be fixed resulting in a time-independent flux in the integrand.

Eq. (15) includes the time period without solar insolation on the nightside of the planet. Time integration is de facto only performed over daylight hours. Moreover, the heliac arc is symmetric with respect to noon. Using t_N=0 h as time of local noon and t_{SS} as time of local sunset, Eq. (15) takes the form

$$\bar{F}^{\pm}{}_{\Delta\lambda}(z,\varphi) = \frac{2}{T_R}\int_{t_N}^{t_{SS}} F^\pm{}_{\Delta\lambda}(z,\varphi,\theta(t))\, dt \ . \quad (16)$$

The solar zenith angle θ is calculated according to

$$\cos\theta = \sin\varphi\sin\delta + \cos\varphi\cos\delta\cos H \ . \quad (17)$$

δ is the solar declination (angle distance of the Sun from the equator plane), and H is the hour angle. H = ω t, ω=360°/T_R. The Earth's angular velocity ω^E is 15°/h. Since day averages $\bar{F}$ are calculated, this value can also be used for other planets when T_R in Eq. (16) is replaced by 24 h. Solar declination δ should not be confused with the inclination (as sometimes done in the literature). Inclination is defined as the angle between the orbital plane of a planet around the Sun and the ecliptic, which is the plane where the Earth is orbiting the Sun. Thus, the Earth's inclination is zero per definition. Mars and Venus have inclinations of 1.85° and 3.39°, respectively. The declination δ is determined by the planetary axis tilt and the resulting seasons over the course of the year. The axis tilt is the angle between the planetary rotational axis and the perpendicular to its Sun orbital plane. The axis tilts of Earth, Mars, and Venus are 23.44°, 25.19°, and 177.36°, respectively. The large tilt value of Venus (North Pole down) is equivalent to the IAU standard of 2.64° that is based on the retrograde rotation definition. The seasonal variability of the Earth's solar declination ranges from +23.44° (summer solstice, June 21) over 0° during the equinoxes (September 23, March 21) to -23.44° (winter solstice, December 22). Consequently, the Sun path angle θ exhibits a large variability with the day of year, and the calculation of accurate

solar fluxes and heating rates for Earth (and also for Mars) requires consideration of seasonal changes.

Due to the small axis tilt of Venus (2.64°), seasonal changes of solar fluxes can be neglected. Test calculations for use of constant δ values 2.64° and 0.0° show that the maximum deviation of resulting heating rates does not exceed 0.05 K/day (~0.06%) at altitudes below 100 km. An approximate and constant solar declination δ=0° is used hereafter, therefore. This reduces Eq. (17) to

$$\cos\theta = \cos\varphi \ \cos H\,. \qquad (18)$$

The local time of sunset (t_{SS}) is calculated from Eqs. (17) and (18) using θ_{SS} = 90° and $H_{SS} = \omega\, t_{SS}$,

$$\begin{aligned} t_{SS} &= \frac{1}{\omega}\arccos(-\tan\varphi\tan\delta) \quad \delta \neq 0°\,, \\ t_{SS} &= \frac{1}{\omega}\arccos(0) = 6\ \mathrm{h} \qquad\quad \delta = 0°\,. \end{aligned} \qquad (19)$$

Hence, when calculating diurnal averages for δ=0°, the solar day integration on Venus extends independently of latitude over 6 hours local time.

Globally (latitude) averaged fluxes $\overline{\overline{F}}^{\pm}_{\Delta\lambda}(z)$ are calculated according to

$$\overline{\overline{F}}^{\pm}_{\Delta\lambda}(z) = \int_{0°}^{90°} \overline{F}^{\pm}_{\Delta\lambda}(z,\varphi)\ \cos(\varphi)\ d\varphi \qquad (20)$$

where cos(φ) is the latitude weighting according to surface integration in spherical coordinates. It reflects the fact that equatorial latitudes contribute much stronger to the globally averaged energy balance than polar latitudes due to the larger relative equatorial area on the planet.

Using the model of a plane-parallel atmosphere, the net flux divergence has only a vertical component, div F^n = dF^n/dz. The energy change per unit time interval dt and unit volume element dV is given by

$$dE = \frac{d\overline{F}^{\,n}_{\Delta\lambda}(z,\varphi)}{dz}\ dV\ dt\,. \qquad (21)$$

A gain of radiative energy heats the atmospheric volume element dV while its pressure is held constant. This thermodynamic energy change of an isobaric process can be expressed by

$$dE = \rho\ c_p\ dV\ dT \qquad (22)$$

where ρ is the air (atmospheric mass) density [kg m^{-3}], c_p is the specific heat capacity, and T is the temperature of volume element dV. c_p defines the amount of energy that is required to heat 1 kg of a medium by 1 K [Ws kg^{-1} K^{-1}]. According to Crisp (1986), the specific heat capacity of a pure CO_2 atmosphere can be approximated by

$$\begin{aligned} c_p(T(z)) &= 443.15 + 1688\ T(z) \\ &- 1.269\times10^{-3}\ T^2(z) + 3.47\times10^{-7}\ T^3(z) \end{aligned} \qquad (23)$$

where all quantities are given in SI units. The air density ρ is calculated according to

$$\rho(z) = \frac{p(z)}{T(z)}\,\frac{M}{R_0} \qquad (24)$$

where p is the atmospheric pressure, M is the mean molecular weight, and R_0 is the universal gas constant (R_0=8.3145 Ws mol^{-1} K^{-1}). At the surface of Venus, a value ρ(0)=65.44 kg m^{-3} is attained using p(0)=92.1 bar, T(0)=735.3 K, and M = 43.44 g mol^{-1}. Altitude profiles of air density, specific heat capacity, and their product ρc_p for the average temperature (and pressure) profile T_{HA} (cf. Fig. 4) are shown in Fig. 19.

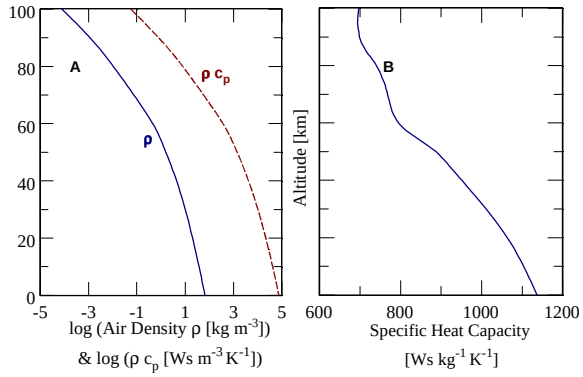

Figure 19. Altitude profiles of air density, specific heat capacity, and product ρc_p.

Combination of Eqs. (21) and (22) yields

$$\overline{Q}_{\Delta\lambda}(z,\varphi) = \frac{dT}{dt} = \frac{1}{\rho(z)\ c_p(z)}\ \frac{d\overline{F}^{\,n}_{\Delta\lambda}(z,\varphi)}{dz}\,. \qquad (25)$$

$\overline{Q}_{\Delta\lambda}(z,\varphi)$ is the atmospheric temperature change rate at level z and latitude φ for a defined spectral interval Δλ and based on diurnal averaging. Given the net flux in [Wm^{-2}] and z in [km], the basic unit of Q is [K/s], but it is finally always given in [K/day] where day refers to one Earth day. Upward directed thermal radiation fluxes F^{+}_{the} are mostly larger than downward fluxes F^{-}_{the}. According to Eq. (13), the net fluxes F^{n}_{the} and the temperature change rates Q_{the} gain a negative sign, and 'radiative cooling' prevails in this case. Downward directed solar radiation fluxes F^{-}_{sol} are generally larger than corresponding upward fluxes, and 'radiative heating' takes place. Real thermal fluxes are always positive of course, but the above definition simplifies illustration of thermal and solar quantities in one plot. Total atmospheric heating and cooling rates are determined extending the flux calculations over the entire spectral range from 0.1-1000 µm.

Flux divergences and temperature change rates are primarily calculated at the layer half-levels between the corresponding main level flux values, that is, at 120 levels between -2 and 140 km. The layer thickness is 1 km between 40 and 130 km (91 flux levels), 2 km between 130 and 140 km (5 flux levels) and also between 6 and 40 km (17 flux levels). Although being in principle not relevant for the calculations, eight 1 km thick layers are considered below 6 km to be able to observe possible responses to surface elevation and emissivity effects. Once the flux divergences and temperature change rates are determined at the half-levels, they are interpolated back to the 121 main levels.

Diurnal averaging of solar fluxes is performed using steps of either 0.5 or 1.0 h in Eq. (16). A coarser step significantly accelerates the calculations. It is verified that flux differences resulting from use of these two grids are negligible below 80 km and do not exceed 0.3 K/day at 100 km. Latitude-dependent results are presently calculated in steps of 10°.

5. Results and Discussion

5.1. Results for an initial standard model

Having collocated all theoretical prerequisites and required spectroscopic and atmospheric input parameters, this section presents results for solar and thermal radiation fluxes and radiative temperature change rates that are based on an initial parameter standard model. These parameters have been specified above in Section 3, but now the unknown UV absorber is considered according to the model described in Fig. 18. Continuum absorption is also taken into account. The latitude-dependent VIRA-N temperature profiles (Fig. 4) are used considering the daytime profile at altitudes above 95 km. Local time parameter variations are not included in this study. As a consequence, thermal calculations above 95 km make use of a mean temperature that is obtained by simply averaging the day and nightside profiles. It is stressed that neither cloud nor UV absorber parameter changes with latitude are considered in the initial standard model. The quasi-monochromatic flux simulations are performed for different grid steps along the wavenumber scale. A detailed description is given below in Section 5.2.1.

One additional parameter has not been mentioned before that has to be specified to ensure proper RTM operation, the surface emissivity. It determines both the thermal surface emission and the surface reflection of downward flux components. The standard model uses a wavelength-independent value of ε=0.7 that may represent basaltic surface features at around 1 µm. The reflectance (surface albedo) is calculated according to A_S=1-ε. A_S will modify the upward fluxes, but it is not expected to affect the results with respect to temperature change rates some kilometers away from the surface. This was verified by test calculations. Thermal cooling rates only change below 2 km with a maximum deviation of about 0.005 K/day (~ 18%) at the surface when A_S=0.0 (closer to real conditions at thermal wavelengths) is used instead of 0.3. Due to the low amount of solar radiation reaching the ground and also due to the large values of air density ρ and specific

heat capacity c_p (cf. Fig. 19), solar heating rates at all altitudes remain completely unchanged. An arbitrary ε or A_S value can be used in the routines, therefore.

Fig. 20 illustrates the solar flux components at 0° latitude (display A) and for the global average (display B) as functions of altitude. Note the different flux scales in the displays. These components are the direct and diffuse downward fluxes and their sum (F^{-dir}, F^{-dif}, F^{-}) and the diffuse upward flux F^{+}. The subscripts 'sol' are omitted here and later on when the notations explicitly refer to solar radiation. Display A contains the four curves for noon and for the day average. Noon at the equator is in good approximation the subsolar point on Venus (see Section 4).

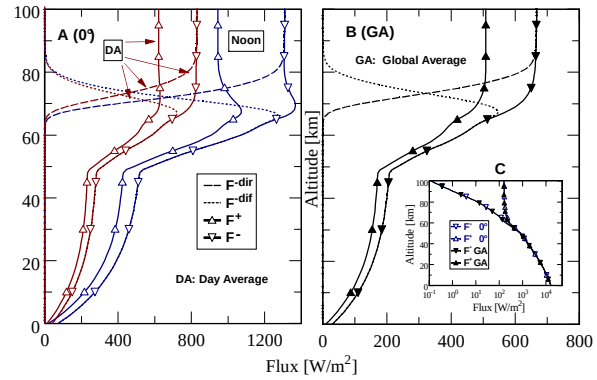

Figure 20. Altitude profiles of solar flux components (direct and diffuse downward fluxes and their sum (F^{-dir}, F^{-dif}, F^{-}) and diffuse upward flux F^{+}). A: Latitude 0°, subsolar point and diurnal average, B: Global average. The inset (display C) shows thermal flux components at the equator and for the global average.

F^{-dir} at the subsolar point corresponds to one half of the solar constant (E*=2618 Wm^{-2}) down to about 95 km. Recall that the diurnal average flux definition according to Eq. (16) is also applied to determine solar fluxes at the subsolar point. Subsolar heating is a quantity that can be used to investigate several responses of atmospheric heating with respect to parameter variations in a faster way, since day time integration is omitted. One can also decide to define subsolar heating by simply multiplying heating result for θ=0 (primarily always calculated in units of [K/s] according to Eq. (25)) by 24 h. This was sometimes done in the literature (e.g. Tomasko et al., 1985). Thus, present subsolar point results may differ by a factor of two from some literature data. The way of definition does not play any role in real energy balance calculations, however. An advantage of the present definition is that cooling and subsolar point heating results can be better illustrated together in one display.

The solar irradiance decreases from noon to sunset, leading to much smaller day averages (DA curves in Fig. 20A) at any latitude compared with subsolar heating. Most of the direct solar flux is either absorbed or redistributed above 70 km (the approximate cloud top region), and the downward flux below 72-74 km becomes quickly dominated by the diffuse component F^{-dif}. In case of the extreme insolation at the subsolar point, the strong forward scattering by cloud mode 1 and 2 particles (mainly at wavelengths shortward of 2 µm (> 5000 cm^{-1}), cf. Fig. 15) generates a local F^{-} flux (total downward solar flux) maximum just below the cloud top altitude. This local maximum also occurs in the upwelling flux. The remarkable bend in the diffuse flux profiles at 48-49 km is due to the cloud bottom, which is defined as a very sharp boundary (cf. Fig. 6). The 70 km flux maxima disappear toward sunset (and also at higher latitudes), but the cloud bottom feature is preserved in all situations. On global average, half of the external solar flux received by Venus (F^{TOA-GA}=667 Wm^{-2}) is absorbed and scattered by CO_2 and cloud mode 1 and 2 particles at altitudes above 74 km. Cloud scattering adds the diffuse downward flux component, which peaks at 68 km. Both components together reach the 50% level of TOA downward flux at 55 km. The contribution of the unknown UV absorber to the total downward flux at this altitude is about 15%. Considering both globally averaged downward and upward solar flux components (that is, the solar net flux, cf. Fig. 21A), half of the solar flux deposited on the planet at TOA altitude (140 km) is absorbed by atmospheric constituents at altitudes above 63 km. Less than 5% of solar TOA flux reaches the surface (73 Wm^{-2} at the subsolar point (5.6%) and 30 Wm^{-2} on global average (4.5%)), and about 20 Wm^{-2} are absorbed on global average at the ground (3% of TOA flux). This stands in a noticeable contrast with

the Earth where the surface absorbs 74% of solar radiation (Arking, 1996).

The inset in Fig. 20 (display C) provides the thermal flux components at the equator and for the global average. The superscript 'dif' is omitted in the box, since all thermal radiation is diffuse radiation. The subscripts 'the' are also omitted here and later on when the notations explicitly refer to thermal radiation. Note again the very different flux scale compared with the main displays. Thermal fluxes below about 60 km seem to fall closely together, but this is only due to graphical representation on the logarithmic scale. Near the surface, both components are as high as 16.5 kWm^{-2}. F^- is zero at TOA altitudes, since there is no external thermal radiation source.

Fig. 21 shows the altitude profiles of globally averaged solar and thermal net fluxes (display A) and net flux divergences (display B) obtained from the individual flux profiles in Fig. 20. The global averages of solar flux deposited on the planet (158.1 W m^{-2}) and the outgoing thermal flux at TOA altitude (140 km) (159.7 W m^{-2}) for the chosen initial standard model are almost identical. This indicates the presence of approximate global radiative equilibrium on Venus. Recall that the equilibrium value derived in Section 2.2 was 157.1 W m^{-2} for the Kurucz (2011) solar irradiance spectrum, which is used as reference in present investigations. For comparison, Titov et al. (2007) derived a value of (157±6) W m^{-2} for the deposited solar flux. Since the actually determined net fluxes are based on a very complex radiative transfer model, it can be concluded that this model and also the initial standard model for spectroscopic and atmospheric parameters are quite well suited to simulate the radiative energy balance of the middle and lower atmosphere of Venus. The small net flux difference of about 1.5 W m^{-2} around the mean value of 159 W m^{-2} cannot be interpreted as an indication of global radiative imbalance due to the uncertainties in both TOA values. Numerical experiments show that the equilibrium TOA value 157.1 W m^{-2} is obtained for both the deposited solar and the outgoing thermal net flux when a total cloud factor of 1.14 (corresponding to a cloud opacity of about 40 at 1 µm) and an UV absorber amount factor of 1.17 are used in the calculations. These modifications do almost not change the globally averaged Bond albedo, it would attain a value of 0.764 instead of 0.763 for the initial atmospheric model.

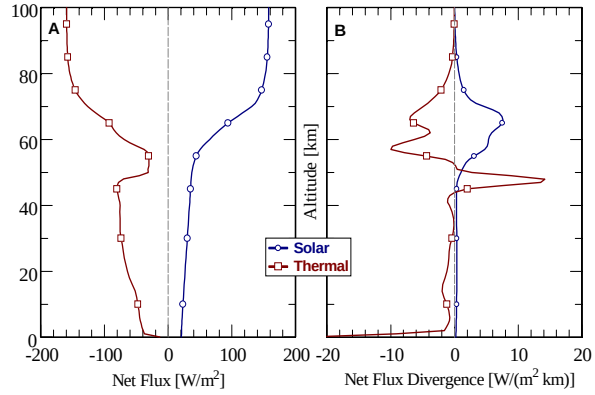

Figure 21. Altitude profiles of globally averaged solar and thermal net fluxes (A) and net flux divergences (B).

Both solar and thermal net fluxes slowly vary with altitude between 80 and 100 km and also between about 48 km and the ground. The influence of surface radiation on the upward thermal flux in the lowest 1-2 km is clearly discernible, however. Much stronger net flux changes occur between 48 km (the cloud bottom altitude) and 80 km due to the influence of cloud layers and of the unknown UV absorber in the solar part. The influence of the latter is well discernible in Fig. 21B (maximum at 65 km). There is a peculiarity in the thermal net flux profile. Its increase between 45 and 55 km yields positive net flux divergences in the cloud bottom region leading to an atmospheric heating.

Due to the almost constant net fluxes at altitudes above about 90 km, net flux divergences become very small. Considering the low air density and specific heat capacity at these altitudes (cf. Fig. 19, ρc_p<0.1 Ws m^{-3} K^{-1} at 100 km) it is clear that the calculation of accurate temperature change rates from Eq. (25) in this altitude domain may pose a challenge. Consequently, the accuracy of flux calculations must be very high. This is discussed in more detail in Section 5.2.1. On the other hand, it is also clear already at this point that temperature change rates in the lower atmosphere below 45 km have to be

very small due to large air densities and the large heat capacity of the atmosphere.

Fig. 22 displays the latitude dependence of thermal and solar TOA net fluxes according to the used VIRA-N model. The globally averaged values are also indicated here. There is a general trend of decreasing solar flux with latitude, since the planet receives solar energy mainly at the equator and at low latitudes due to the latitudinal dependence of the solar zenith angle. The outgoing thermal flux shows another peculiarity of Venus' atmosphere.

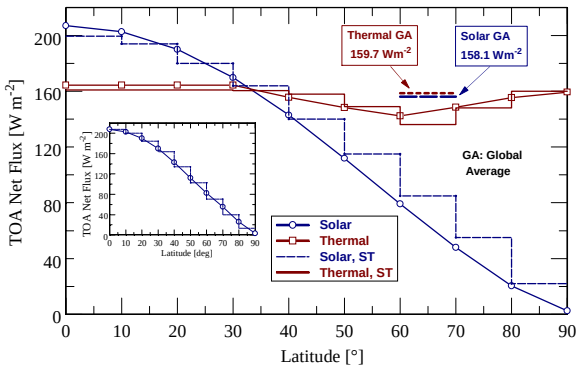

Figure 22. Latitude dependence of thermal and solar TOA net fluxes. ST: Results from Schofield and Taylor (1982). GA: Results for global averages. The inset shows corrected solar flux curves that considers both albedo (ST) and cloud parameter (this work) changes with latitude (see text).

Thermal fluxes at Earth and Mars monotonically decrease from mid latitudes toward the poles. On Venus, the thermal flux only weakly decreases between 30° and 60°, but then increases again toward the poles to reach values that are comparable with those at equatorial latitudes. This is a consequence of higher mesospheric temperatures poleward of the cold collar that resides at latitudes between about 55° and 75° (cf. Fig. 4). Since the high polar temperatures are not forced by solar insolation, dynamical processes must be responsible for the observed temperature field. The two staircase-shaped curves in Fig. 22 are results taken from Schofield and Taylor (1982). They assumed the Bond albedo A_B to be latitude-independent (A_B=0.762). A_B for the present model of the unknown UV absorber however varies from about 0.75 at the equator to 0.89 at the poles in accordance with Moroz et al. (1985). This leads to lower deposited solar energy with increasing distance from the equator compared with the constant albedo value as shown by the modified staircase-shaped curve in the inset of Fig. 22. The RTM simulation used to generate the solar net flux profile, which is described by the smooth solid line with empty circles, now additionally considers the decrease of cloud top altitude as retrieved by Haus et al. (2014a). These two modifications yield a very good agreement of both solar flux curves.

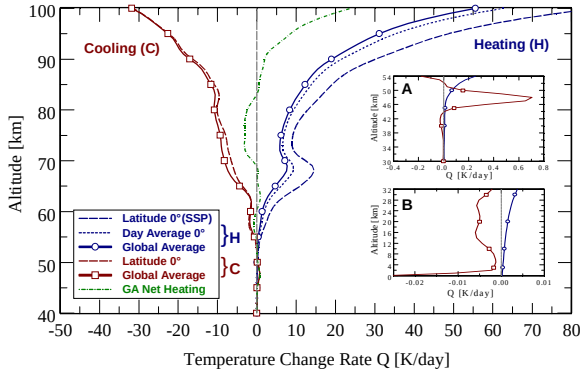

Figure 23. Equatorial day averages and global averages of thermal cooling, solar heating, and net heating rates. Heating rates are also shown for the subsolar point (SSP). The insets represent zooms of global average curves near the cloud base (A) and near the surface (B).

Fig. 23 illustrates altitude profiles of equatorial day averages and global averages of thermal cooling, solar heating, and net heating rates based on the initial atmospheric standard model and the flux results shown in Figs. 20-22. Recall that global averages are based on a weighting of latitude-dependent quantities with the cosine of latitude. Heating rates are also displayed for the subsolar point (SSP). At 100 km altitude, the latter may reach more than 80 K/day. This value reduces to 55 K/day on global average. This is almost twice the value found for thermal cooling at this altitude leading to a net heating of more than 20 K/day. Net heating of the atmosphere occurs down to 82 km. A negative net heating (net cooling) of about 3 K/day is found above the cloud top region at altitudes between 70 and 80 km. The almost zero net heating between 65 and 70 km is forced by the unknown UV absorber (cf. Fig. 24 below). Radiative heating and cooling are generally very small at altitudes below 55 km. This is mainly due to the strongly increasing air density and specific heat capacity with decreasing altitude (cf. Fig. 19). Inset A illustrates the above mentioned

peculiarity of thermal fluxes near the cloud base at 48 km in terms of temperature change rate. There is a significant heating in the order of 0.7 K/day. The deep atmosphere below 30 km is practically not heated by solar radiation (inset B). Thermal cooling rates are in the order of 0.005 K/day except for the lowest 1-2 km where the direct hot surface radiation (T=735 K) causes a net cooling up to 0.025 K/day.

Fig. 24 shows the contributions of individual atmospheric constituents to the total temperature change rates. The calculations are performed for the equator (subsolar point in case of heating). It is important to mention that the results are only indicative of the approximate role of these constituents in energetics calculations, since net fluxes that result from absorption characteristics of individual species that contribute to a certain spectral range are not additive. Thermal cooling (display A) above 75 km is mainly determined by infrared CO_2 emission. Note that 'distant wings' of mode 1 and 2 cloud particle distributions (cf. Fig. 6) cause a weak heating at thermal wavelengths (predominantly near 10 µm) at altitudes between 80 and 90 km. H_2O influence becomes important at altitudes below about 70 km. The same holds true for SO_2, which causes the deviation of the two curves marked by 'CO2+H2O' and 'all gases'. HDO, CO, HF, and HCl can be completely neglected here. OCS may slightly contribute near the cloud base.

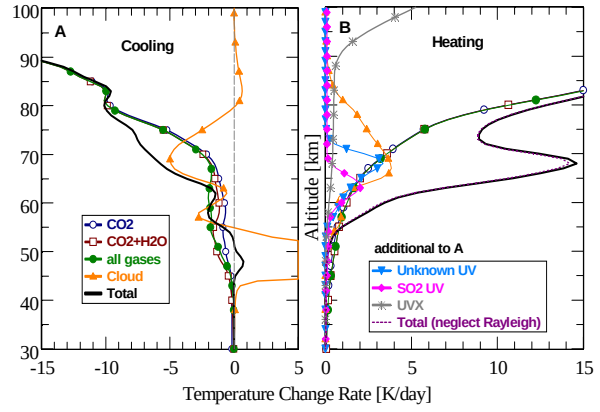

Figure 24. Contributions of individual atmospheric constituents to the total temperature change rates at equatorial latitudes (subsolar point in case of heating). Note that the components are not additive.

The altitude range of the cloud base (~48 km) would experience an extreme heating (up to 150 K/day) in the absence of gaseous constituents, but this is clipped off in the figure. Although this hypothetical pure cloud heating is mainly compensated by the dense CO_2 atmosphere in reality, the cloud base range is sensitive to the distribution of the minor constituents H_2O and SO_2. This will be investigated in more detail in Section 5.3.2.

As in case of thermal cooling, solar heating (display B) above 70-75 km is dominated by near infrared CO_2 absorption, but cloud mode 1 (the upper haze part) and cloud mode 2 particles (the latter being more important) also provide some contributions here. CO_2 absorption at UV wavelengths shortward of 0.3 µm is significant at all altitudes above 60 km, especially above 90 km. CO_2 dissociation strongly increases at these altitudes. UV absorption by H_2O, OCS, and HCl (cf. Fig. 12) can be completely neglected, however. It is important to note that UV CO_2 heating above about 90 km is predominantly caused by solar absorption in the spectral range shortward of 200 nm (>50000 cm^{-1}) even though the solar irradiance is very small here. The unknown UV absorber and SO_2 UV absorption add strong contributions to the heating between 58 and 72 km. Minor gas line absorptions play a minor role in the solar spectral range. SO_2, OCS, HF, and HCl can be completely neglected there under nominal conditions. CO yields a small contribution of 0.8 K/day at 100 km (not discernible in the graph), but is also negligible at lower altitudes. Neglect of Rayleigh scattering would slightly modify the heating results below about 75 km. Its maximum influence (0.4 K/day) is only discernible in the figure at the local heating maximum at 68 km.

5.2. Responses to spectroscopic model parameter changes

5.2.1. Accuracy of absorption cross-sections and optimization of numerical procedures

At pressures below about 1 mb (~86 km on Venus), the width of a spectral line is mainly determined by Doppler broadening, while it is

more and more dominated by collisional (Lorentz) broadening at higher pressures. Typical Doppler half-widths are in the order of $5x10^{-4}$ and $3.5x10^{-3}$ cm^{-1} in the CO_2 bands located at 15 and 2 µm, respectively. It can be expected, therefore, that high altitude gaseous absorption cross-sections σ_a are significantly in error when a too coarse wavenumber grid (called point distance PD in the following) is selected in the line-by-line calculation procedure.

Fig. 25 shows CO_2 absorption cross-sections σ^{CO2} at different altitudes and for point distances of 0.001, 0.01, and 0.1 cm^{-1} in the spectral range 640-680 cm^{-1}, which is part of the strong 15 µm CO_2 band (cf. Figs. 7 and 8A). This range was also simulated for PD=0.0001 cm^{-1}, but there are no σ^{CO2} differences between this extremely high resolution and PD=0.001 cm^{-1}. On the other hand, it is very evident that coarser PD's at low pressures (90 km, display A) do not resolve the real structure within an absorption band. The important line centers are mostly lacking for PD=0.1 cm^{-1} (note the logarithmic scale). This situation is considerably improved with increasing pressure. At 70 km (display B), the difference between PD's of 0.001 and 0.01 cm^{-1} is tiny and only discernible at the line maxima. On the other hand, PD=0.1 cm^{-1} is again not sufficiently accurate. This is the case at 50 km, however, where any differences between the three PD's disappear. The strongest CO_2 bands located at 15, 4.3, 2.7, and 2.0 µm are mostly responsible for absorption of solar energy above the cloud deck. Weaker bands (e.g. near 10 µm) absorb radiation at lower altitudes, and the use of coarser PD's is sufficient, therefore. Anyway, a point distance of 0.001 cm^{-1} should be used as primary reference for line-by-line absorption cross-section databases of CO_2 at least in the vicinity of the main band centers and at high altitudes. This is a non-trivial problem considering that the generation of a complete CO_2 cross-section base σ^{CO2} in the total spectral range from 10 to about 13000 cm^{-1} (cf. Fig. 7), for 22 reference pressure levels and 3 reference temperatures at each pressure level, for a line cut condition of υ_c=125 cm^{-1}, and for a point distance of 0.01 cm^{-1} (i.e. 10 times below the true requirement) takes several weeks of computation time. Calculations of 0.001 cm^{-1} σ^{CO2} bases are only feasible for the band center regions of the main bands, therefore. The abundances of minor constituents in Venus' atmosphere are very low compared with CO_2, and a spectral resolution of 0.01 cm^{-1} is sufficient.

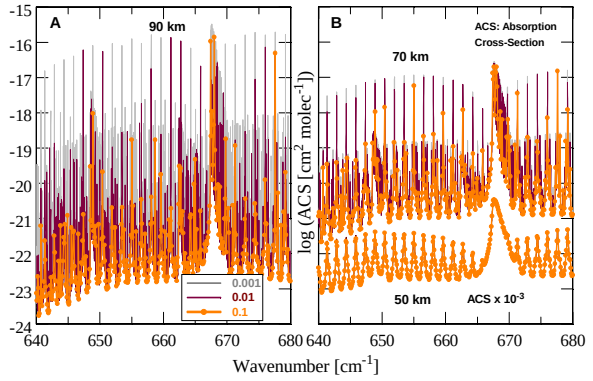

Figure 25. CO_2 absorption cross-sections as functions of wavenumber in the center of the 15 µm band at 90, 70, and 50 km altitude for point distances of 0.001, 0.01, and 0.1 cm^{-1}. The curve for 50 km is multiplied by a factor of 10^{-3} for better discriminability.

Fig. 26 illustrates spectral point distance influences on temperature change rates Q in a hypothetical pure CO_2 atmosphere (latitude 0°, subsolar point in case of heating). Differences $\Delta Q^H(P1, P2)=Q^H(P1)-Q^H(P2)$ are shown in this figure and in some other figures below where Q^H refers to heating rates and P1 and P2 refer to the two different parameters in each comparison. In case of cooling, $\Delta Q^C(P1, P2)= - [Q^C(P1)-Q^C(P2)]$ is used instead in order to compensate for negative cooling values. This facilitates the direct comparison of heating and cooling responses to parameter changes. Display A shows the differences ΔQ(PD=0.01 cm^{-1}, PD=0.001 cm^{-1}) for the 15 µm band in cooling mode and for the 2.7 and 4.3 µm bands in heating mode. Display B is described later on. ΔQ is a measure of the error in the calculated temperature change rates due to less accurate CO_2 absorption cross-section databases. Negative values mean that the coarser grid yields less heating or less cooling. The differences for all three bands are very small at altitudes below 90 km (usually less than 0.01 K/day) and do not exceed 0.3 K/day at 100 km. The change between positive and negative ΔQ values is due to the specific distribution of spectral lines in the

corresponding bands. As a consequence, the differences of heating bands may partly compensate. It can be concluded that the use of CO_2 absorption cross-section databases at a spectral point distance of 0.01 cm^{-1} is always sufficiently accurate to model the temperature change rates in the Venus atmosphere up to the mesopause at 100 km.

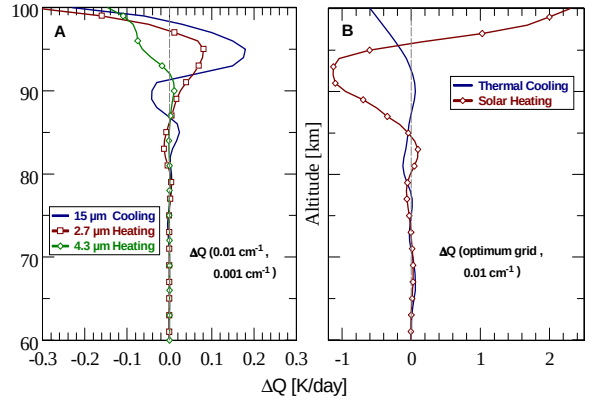

Figure 26. Deviations ΔQ of temperature change rates in a pure CO_2 atmosphere (latitude 0°, subsolar point in case of heating) due to spectral point distance modifications. Display A: Deviations for selected CO_2 bands with respect to a very high resolution reference grid. Display B: Deviations for an optimized point distance grid.

Spectral ranges between the strong CO_2 bands but also different sub-intervals within these bands contribute much less to temperature change rates at higher altitudes than the band center regions do. This is illustrated in Fig. 27 for a pure CO_2 atmosphere at equatorial latitudes. In contrast with Fig. 24, temperature change rates of individual spectral ranges of the same atmospheric species are additive. The maximum contributions from the near and distant wings of the 15 µm CO_2 thermal band for example (display A, ranges < 600 cm^{-1} and 750-1000 cm^{-1}) are -1.25 K/day at 76 km and -0.61 K/day at 72 km, respectively, while the band center range yields ever increasing cooling rates above 70 km up to $5x10^4$ K/day at TOA altitude of 140 km. Band wing contributions above 85 km are very small, but they may produce stronger cooling at lower altitudes where the above discussed point distance influences do no longer affect the results. The characteristic bend in the total cooling curve near 82 km is mainly a consequence of the additive influence of the different spectral range contributions.

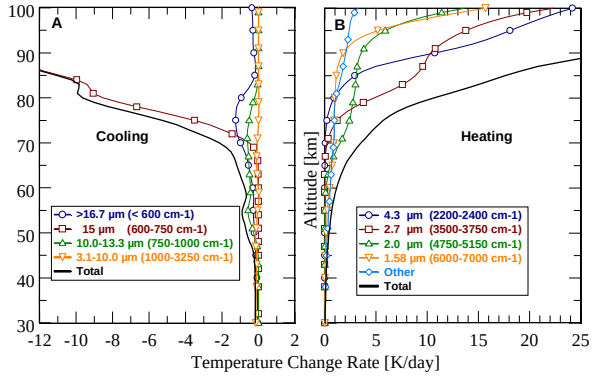

Figure 27. Contribution of individual bands in a pure CO_2 atmosphere at equatorial latitudes (subsolar point in case of heating).

Display B shows the heating contribution of the main CO_2 bands at the subsolar point. The relative contributions of the bands do not change with local time and latitude but vary with altitude. The 4.3 and 2.7 µm bands clearly dominate above 85 km, and the former takes the leading part above 90 km. The 2.0 µm band yields the next strongest contributions at altitudes between 85 and 95 km. It seems to be surprising that the much weaker 1.58 µm band (cf. Fig. 7) generates larger contributions above 95 km, but this is due to the broader spectral range that is considered here for the 1.58 µm band ($\Delta\upsilon$=1000 cm^{-1}) compared with the other bands (e.g. $\Delta\upsilon$=400 cm^{-1} for 2.0 µm). It is interesting to observe the 2.0 µm band dominance between 70 and 75 km. Other CO_2 spectral ranges including the much weaker solar bands (e.g. 1.44, 1.32 µm) cannot be neglected. They dominate heating below 60 km, and their contribution at 100 km is even about 3 K/day.

Based on this discussion with respect to Fig. 27, it is worth to perform a detailed study on further acceleration options for the used algorithms including the search for spectral ranges where even coarser point distant grids than 0.01 cm^{-1} can be applied. This will certainly be the case outside the main CO_2 and minor constituent bands.

The thermal spectral range is divided into 13 sub-intervals covering the total range 10-6000 cm^{-1} (1.67-1000 µm). These intervals are not only defined by the different spectral contributions of CO_2 but also by minor gas

band contributions according to Figs. 8 and 9. Interval 13 extends from 3250 cm^{-1} (3.1 µm) to 6000 cm^{-1} (1.67 µm), since small (and even negative) cooling effects in the lower atmosphere are identified up to this bound. The intervals are given in Table 4. Each interval is investigated in detail, and cooling rates are calculated for the four spectral point distances PD=0.01, 0.1, 1.0, and 10 cm^{-1}. As a compromise, maximum absolute cooling rate errors for the total thermal spectral range of ±0.2 K/day below 90 km and ±1.0 K/day at 100 km are tolerated. Interval 8 (the center range of the 15 µm band (600-750 cm^{-1}) always requires PD=0.01 cm^{-1}. Intervals 1-7 (10-600 cm^{-1}) and intervals 9-11 (750-1000 cm^{-1}) can be considered using the coarser grid PD=0.1 cm^{-1}. This becomes possible, since differences for individual sub-ranges partly compensate each other. Intervals 12 and 13 yield acceptable results even for PD=10.0 cm^{-1}.

The resulting cooling rate deviations are shown in display B of Fig. 26 in terms of ΔQ(optimum grid, PD=0.01 cm^{-1}). Errors up to 95 km are usually smaller than ±0.1 K/day. At 100 km, the selected optimum PD grid yields 0.6 K/day less cooling than for PD=0.01 cm^{-1}. Using the optimum PD grid, a processing time reduction factor of 10 (now about 360 s for one latitude) is achieved compared with the required time for PD=0.01 cm^{-1}.

Table 4. Spectral sub-intervals in the thermal and solar spectral ranges and optimum point distances (PD) for quasi-monochromatic flux calculations. Wavenumber and PD are given in [cm^{-1}]. Superscript letters denote the main absorption bands: [a] 15, [b] 4.3, [c] 2.7, [d] 2.0, [e] 1.58, [f] 1.44, [g] 1.32 (all in [µm]).

Thermal

No.	Wavenumbers	PD	No.	Wavenumbers	PD
1	10 - 100	0.1	8[a]	600 - 750	0.01
2	100 - 200	0.1	9	750 - 850	0.1
3	200 - 300	0.1	10	850 - 900	0.1
4	300 - 350	0.1	11	900 - 1000	0.1
5	350 - 450	0.1	12	1000 - 3250	10.0
6	450 - 500	0.1	13	3250 - 6000	10.0
7	500 - 600	0.1			

Solar

No.	Wavenumbers	PD	No.	Wavenumbers	PD	No.	Wavenumbers	PD
1	10 - 600	10.0	10[d]	4750 - 5150	0.1	19	8050 - 8300	1.0
2	600 - 750	1.0	11	5150 - 5350	1.0	20	8300 - 9400	1.0
3	750 - 1900	1.0	12	5350 - 6000	1.0	21	9400 - 9650	1.0
4	1900 - 2200	0.1	13[e]	6000 - 6500	0.1	22	9650 - 10000	10.0
5[b]	2200 - 2400	0.1	14	6500 - 6900	0.1	23	10000 - 12800	10.0
6	2400 - 3250	1.0	15[f]	6900 - 7000	0.1	24	12800 – 25000	500.0
7	3250 - 3500	1.0	16	7000 -7500	1.0	25	25000 -50000	500.0
8[c]	3500 - 3750	0.1	17[g]	7500 -7800	1.0	26	50000 -80000	500.0
9	3750 - 4750	1.0	18	7800 -8050	10.0			

The same type of investigation is performed for the solar range. It is divided into 26 sub-intervals that are again defined by the different spectral contributions of individual gases according to Figs. 8 and 9. Solar heating calculations extend down to 10 cm^{-1} (1000

µm), since small heating contributions occur even at low wavenumbers. The 15 µm band for example produces an equatorial (subsolar point) pure CO_2 heating of 0.7 K/day at 100 km. The intervals and the determined optimum PD grids are summarized in the lower part of Table 4. The calculation of solar heating rate is much more expansive than the calculation of thermal cooling rates. The total considered solar range is broader by a factor of about 13, and at least seven solar half-day integration steps (noon and at each full hour after noon) are required. Thus, numerical solar calculation runs exceed the thermal ones by a factor of at least 90. The ambitious error limits of 0.2 and 1.0 K/day being used in the thermal range cannot be maintained for the solar range, therefore. The determined sub-interval point distances given in Table 4 are a result of numerous trial and error tests to keep the total computation time within reasonable limits and to find an optimum grid that partly produces compensations of heating rate deviations due to coarser grids in certain sub-intervals. None of these intervals uses the point distance of 0.01 cm^{-1}, since this would be too time consuming in operational calculations. Actual PDs vary between 0.1 and 1.0 cm^{-1} shortward of 9650 cm^{-1} with the finer value in the main CO_2 bands. At larger wavenumbers, even a 10 cm^{-1} PD can be used. In the visible and UV ranges, a very coarse PD of 500 cm^{-1} is sufficient, since there are no significant gaseous line absorptions.

The resulting heating rate deviations for a hypothetical pure CO_2 atmosphere are shown in Fig. 26 (display B). Note that the depicted errors in display B do not include the depicted values in display A, but considering the different scales in the displays, B errors would not seriously change. Moreover, A and B errors partly compensate. Deviations of the optimum grid compared with PD=0.01 cm^{-1} are smaller than ±0.1 K/day below 85 km. Above about 90 km, they reach -1.1 K/day and then turn to +2.3 K/day at 100 km. Solar heating is strongest at the subsolar point, and differences in the heating rates are consequently also strongest here. Since final heating rates are averaged over all solar zenith angles during the course of a day (and additionally over all latitudes when global averages are calculated), the resulting final errors become even smaller (e.g. 0.7 K/day near 92 km and 1.7 K/day at 100 km). Compared with PD=0.01 cm^{-1}, a processing time reduction factor of about 40 is achieved when the optimum grid is used (now about 360 s for one latitude and one solar zenith angle). These are very satisfying results at the end of a huge portion of analysis work.

5.2.2. Spectral line databases

Present studies utilize the HITRAN 2008 line database (Rothman et al., 2009) as standard data set for calculating molecular absorption cross-sections. Two other databases are also investigated, the HITEMP-Venus database ("HOT-CO2", Pollack et al., 1993) and the HITEMP-Earth database (Rothman et al., 2010). The former was slightly modified by incorporation of some data from the high-temperature carbon dioxide spectroscopic databank (CDSD, Tashkun et al., 2003) to provide optimum fits of measured VIRTIS-M-IR spectra (Haus et al., 2013a). The databases slightly differ with respect to line positions, line intensities, line half-widths, and other spectroscopic parameters. Some gaps occur in the HITRAN 2008 CO_2 line list near 1 µm. The parameter differences are still large enough, however, to produce significant variations of calculated fluxes and temperature change rates.

Fig. 28 visualizes the calculated cooling and heating rate differences (equator, diurnal average in case of heating) in the form ΔQ(H08, X) where H08 is the synonym for HITRAN 2008 and X stands for either HITEMP 1993 or HITEMP 2010. Note the different ΔQ scales for heating and cooling responses. Both HITEMP databases produce similar results as HITRAN 2008 below 90 km. Deviations are not larger than ±0.1 K/day for cooling and -0.2 K/day for heating, respectively. Positive ΔQ values are indicative for smaller temperature change rates resulting from use of HITEMP. This way, the differences would partly compensate with respect to net heating, although cooling

deviations ΔQ^C are generally smaller than heating deviations ΔQ^H. The deviations reach -0.3 (ΔQ^C) and +3.0 (ΔQ^H) K/day at 100 km. It should be also mentioned that the HITEMP databases yield slightly smaller thermal heating near the cloud base. This is exactly what is to be expected, since HITEMP bases contain much more weak lines that become important at higher temperatures in the lower atmosphere. It was shown in Figs. 24 and 27 that CO_2 and other gases would never produce atmospheric heating at any altitude at thermal wavelengths, since the upward thermal flux always dominates the downward flux. Near the cloud base, gaseous absorption acts to attenuate strong cloud heating, however. An increased CO_2 cooling in case of HITEMP provides a stronger heating compensation than HITRAN 2008 does. Thus, ΔQ as defined above becomes positive near the cloud base. Below about 45 km and down to the surface, cooling rate differences defined as $\Delta Q^C = -[Q^C(H08)-Q^C(X)]$ become always negative, that is, HITEMP yields more cooling, but this difference never exceeds an absolute value of 0.0025 K/day due to the smallness of radiative cooling at these altitudes (cf. insets in Fig. 23). Heating rate differences almost completely vanish.

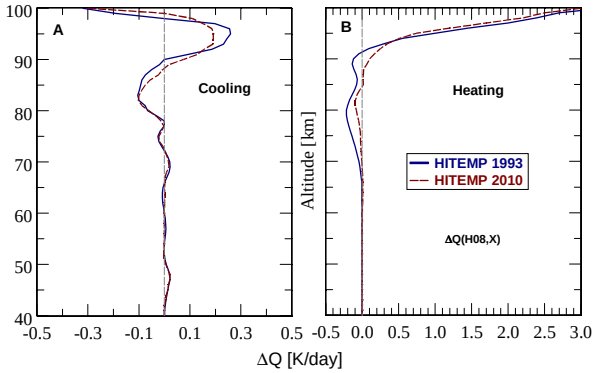

Figure 28. Response of temperature change rates to the used spectral line database. HITRAN 2008 (H08) is the default database. Latitude 0°, diurnal average in case of heating.

5.2.3. Continuum absorption and line shape factors

It was discussed in Section 2.5.3 that continuum contributions from distant line wings may change the absorption cross-sections of infrared active gases. It was shown however that different line cut conditions and also different sub-Lorentz line profiles do not influence the center regions of the main absorption bands. Fig. 29 illustrates the temperature change rate responses (equator, diurnal average of heating) to variations of these parameters where υ_c=125 cm^{-1} is the default line cut condition, and the Tonkov profile (Tonkov et al., 1996) is the default line shape factor. Differences are calculated according to ΔQ(default, X) (cf. ΔQ definition in Section 5.2.1, Fig. 26) where X stands for either different υ_c values or different line shape factors. 'Bézard' refers to Bézard et al. (1990). Continuum absorption of far line wings (υ_c=500 cm^{-1}) does not play a significant role in radiative heating of the atmosphere (ΔQ^H<0.01 K/day). Cooling rate differences are usually less than 0.05 K/day, but a local minimum of ΔQ^C=-0.13 K/day is detected near the cloud base. Since this region is determined by a weak thermal heating in the order of 0.7 K/day for υ_c=125 cm^{-1}, the continuum reduces this value by about 20% down to 0.55 K/day. It is recommended therefore to model thermal radiation fluxes at least by use of a line cut condition υ_c=250 cm^{-1} in future calculations. The line cut condition υ_c=10 cm^{-1} was only utilized in this study to provide quick looks of absorption cross-section databases, since it considerably reduces computational expenses. It is not applied further on.

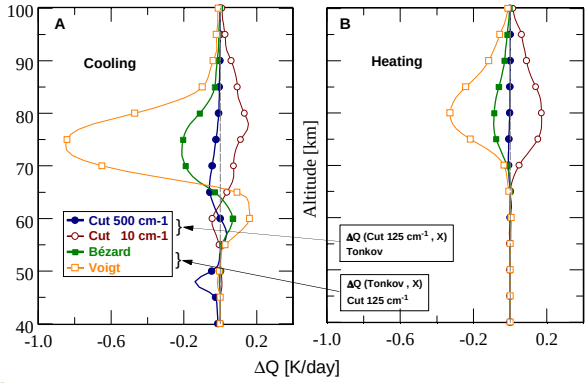

Figure 29. Response of temperature change rates to variations of line cut condition and sub-Lorentz line profile. Latitude 0°, diurnal average in case of heating.

Different sub-Lorentz profiles affect the temperature change rates mainly at altitudes between 60 and 80 km, but in view of the magnitude of cooling and heating at these altitudes, the deviations are rather small. The

curves indicate that the use of any of the studied sub-Lorentz profiles should be favored over a pure Voigt profile. A decision on a "best choice" model based on present studies is not possible, however. Other calculations (not shown here) clearly indicate that the deep atmosphere CO_2 continuum that is very important for the retrieval of cloud parameters, minor gas abundances, and surface emissivity from measured VIRTIS radiance spectra (Haus et al., 2013a; 2014a; 2015; Kappel et al., 2015a; 2015b) can be safely neglected in energy balance calculations.

5.2.4. Solar irradiance spectra

Section 2.3 has introduced the two data sets on solar irradiance spectra that are used in present investigations (Kurucz, 2011; ASTM Standard E490-00a, 2006; cf. Fig. 2). With respect to Fig. 3 it has been emphasized that Kurucz and ASTM spectra are not expected to produce a significant radiative forcing difference, while the equivalent Planck irradiance curve may generate significant errors. Fig. 30 shows the response of solar heating rates to the different solar insolation data sets. Inset A compares Kurucz and ASTM data. There is a small deviation of 0.1 K/day near 65 km. Larger deviations up to -1.2 K/day are identified at 100 km, but they are marginal compared with absolute heating values at this altitude. The curves marked by solid and empty circles in the main display compare the heating rates for Kurucz and Planck insolation spectra when the spectral range (1) from 10 to 25000 cm^{-1} (0.4-1000 µm) is considered in the calculations. This range is characterized by an underestimation of the solar irradiance applying Planck's law (cf. Fig. 3), and as a consequence, the Planck heating rates are slightly smaller. The deviation does not exceed -0.4 K/day below 95 km. The situation changes dramatically, however, when the spectral range (2) from 25000 to 80000 cm^{-1} (0.125-0.4 µm) is considered where Planck's law yields much larger solar irradiances compared with measurement data. The differences between the two curves marked with solid and open boxes in Fig. 30 may reach 90 K/day at 100 km and are always larger than 2 K/day down to the cloud top region. Inset B, which is a zoom from the main display, explains that this huge difference is almost exclusively due to the influence of the UV_X absorbers (mainly CO_2). Omitting them would yield a maximum heating rate deviation of about 1 K/day near 65 km. Since equivalent Planck irradiance spectra are sometimes used in the literature (e.g. Lee and Richardson, 2011) to parameterize the spectral distribution of the incoming solar radiation, it is important to hint on this possible error source.

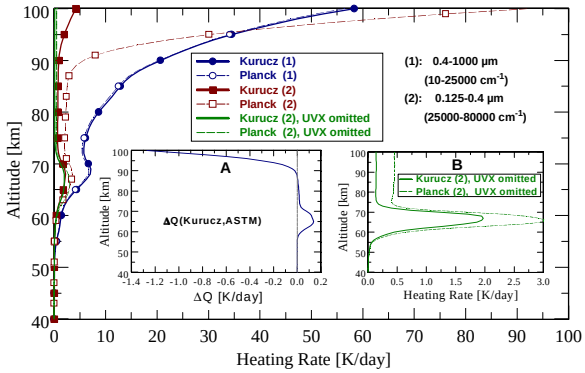

Figure 30. Response of solar heating rates to solar insolation models. Inset A: Change of heating rates when using Kurucz or ASTM data. Inset B: Zoom from the main display. Latitude 0°, diurnal average in case of heating.

Summarizing the response analyses of atmospheric temperature change rates with respect to spectroscopic model parameters performed in Section 5.2, it can be stated that the calculated cooling and heating rates are very reliable at altitudes below 85 km with maximum uncertainties of about 0.25 K/day. Cooling uncertainties do not increase between 85 and 95 km, but heating uncertainties may reach 1 K/day. Heating uncertainties of about 3-5 K/day are possible at 100 km. Use of Planck's radiation law to model incoming solar radiation is not recommended.

Most spectroscopic analyses are based on certain models (line databases, line shape factors etc.). One should therefore not talk about resulting errors while using different models, since the error of a certain quantity is its possible deviation from an objective 'ground-truth' value. This ground-truth is not known in the present case. Assuming for

example that the HITEMP 2010 database is the only correct one, the deviations of heating rates above 90 km due to use of HITRAN 2008 (cf. Fig. 28) would change the sign and nearly compensate the deviations caused by application of the optimum point distance grid instead of the 0.01 cm^{-1} grid (cf. Fig. 26).

5.3. Responses to atmospheric parameter variations

The discussions in Section 5.2 have been devoted to spectroscopic parameters that are either specified by the finally applied models (line database, solar irradiance spectrum) or determined by the chosen approximations (point distance, continuum, line shape). This section is going to discuss responses of atmospheric fluxes and temperature change rates to parameter variations that occur under real atmospheric conditions. It has been already mentioned in the introduction section that present investigations do not intend to model the complete radiative energy balance on the basis of multi-dimensional input data. The main goal is a study of possible influences of different model parameters.

5.3.1. Thermal structure

Fig. 31 illustrates responses of radiative net flux divergences and resulting temperature changes rates (diurnal average in case of heating) to atmospheric temperature profile variations with latitude according to Fig. 4. Temperatures may vary by more than 40 K near 60 km (cold collar (~60° latitude) temperatures are the lowest ones) and by about 10 K at 70 km (higher temperatures at high latitudes).

Thermal net fluxes and their divergences (display A) strongly depend on atmospheric thermal structure at altitudes between the cloud bottom (~48 km) and about 75 km but only slightly change at higher altitudes. Thermal cooling rates Q^C essentially follow the divergence profiles in this altitude domain, but Q^C variations below 50 km become very small due to the strong increase of air density ρ and specific heat capacity c_p (cf. Fig. 19 and Eq. (25)). At altitudes above 75 km, Q^C variations are mainly determined by temperature and pressure induced changes of the product ρc_p. At 80 km for example, the net flux divergence for T(0°) and T(60°) is equal to -1.00 and -0.87 W/(m^2 km), respectively. The corresponding ρc_p values are 8.47 and 6.43 Ws/(m^3 K) resulting in $Q^C(0°) = 1.18 \times 10^{-4}$ K/s = 10.2 K/day and $Q^C(60°) = 1.47 \times 10^{-4}$ K/s = 12.7 K/day. This means, Q^C at 80 km differs by about 2.5 K/day, although the difference of net flux divergences is only 0.13 W/(m^2 km). The variability of Q^C decreases toward 100 km, since the different temperature profiles converge.

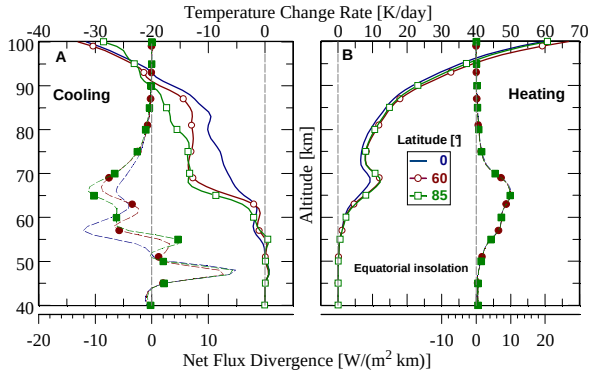

Figure 31. Responses of net flux divergences (broken lines) and temperature change rates (solid lines) to variations of atmospheric thermal structure according to VIRA-N. Diurnal averages in case of heating.

Altitude profiles of solar net flux divergences (display B) show a very weak sensitivity to temperature changes. Solar heating rates Q^H are mainly determined by ρc_p changes, resulting in larger heating rates for high latitude temperature profiles. Note that equatorial insolation conditions are assumed for this comparison. Otherwise it would not be possible to investigate the pure temperature effect with respect to heating, since solar insolation strongly reduces with increasing latitude resulting in much smaller real heating rates.

In summary it can be stated that radiative net flux divergences and resulting cooling rates in the thermal spectral range strongly depend on atmospheric thermal structure including meridional as well as zonal variations. Solar net fluxes, on the other hand, weakly respond to temperature changes, and overall heating

rate variations are smaller than in the thermal case. Nevertheless, temperature influences on both components have to be carefully taken into account when calculating two- or three-dimensional net heating rates.

5.3.2. Minor gas abundances

Fig. 32 illustrates the influence of minor gas abundance changes by a factor of two (3 solid lines) on the calculated cooling and heating rates (equator, diurnal average in case of heating) in terms of ΔQ(X, Initial) where X denotes which of the gas factors is modified and 'Initial' refers to the initial abundance profiles of that gas (that is, gas factor 1.0) shown in Fig. 5. In the thermal spectral range (display A), both H_2O and SO_2 may affect the cooling rates over a broad altitude range. A doubling of H_2O abundances at all altitudes would intensify thermal cooling at altitudes between 60 and 100 km (domain 1) by up to 0.15 K/day and up to 0.2 K/day near the cloud base (48 km, domain 2). Related to the absolute values of cooling in these altitude domains, the radiative effect of H_2O is small in domain 1 but quite large in domain 2. Higher SO_2 abundances mainly act near 63 km. Very small changes of cooling rates at the cloud base are also possible due to the influence of OCS (cf. Fig. 9), which dominates the 'other' curve characteristics in the thermal spectral range. The 2.3 and 4.8 µm bands of CO and also HF and HCl bands are not effective. Thus, variations of CO, HF, and HCl do not produce any responses and can be safely neglected. The broken line describes the possible response of cooling rates to a SO_2 abundance boost by a factor of ten. Such high abundance variations were observed by Marcq et al. (2011; 2013). The authors reported on a general two-fold SO_2 increase at cloud top levels in the years 2006-2008 over the northern hemisphere and an episodic much stronger increase in early 2007, while a SO_2 decrease by an order of magnitude occurred between 2008 and 2012. The strong sudden increase was possibly due to a convective episode transporting some sulfur dioxide from deep atmospheric layers into the mesosphere. This event could have been related to volcanic activity (Esposito et al., 1988). Under 'normal' conditions however, SO_2 variability by a factor of two and cooling rate changes up to 0.2 K/day seem to be reasonable limits.

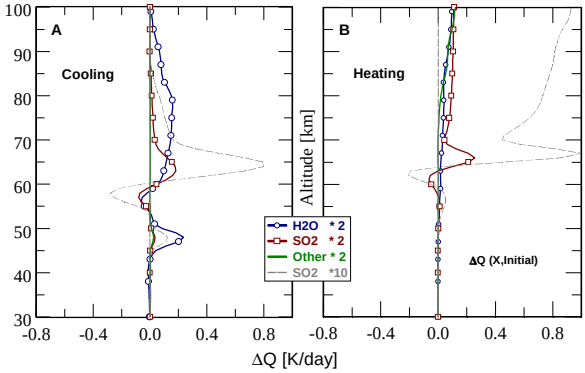

Figure 32. Response of temperature change rates to variations of atmospheric minor gas composition. Latitude 0°, diurnal average in case of heating.

The influence of water vapor on atmospheric heating rates (display B) is rather small. It reaches 0.1 K/day at 100 km. 'Other' minor gas influence in the solar spectral range above 75 km is determined by carbon monoxide in case of heating, since CO abundances strongly increase above 70 km (cf. Fig. 5). The 2.3 µm CO band (cf. Fig. 8) is mostly responsible for the observed heating. Due to the general uncertainties of heating rates near 100 km, a Q^H change of 0.1 K/day is not important for the overall energy balance. As in case of thermal cooling, SO_2 abundance variations may affect solar heating mainly near 65 km and in the same order of magnitude (0.2 K/day). It is important to note that the depicted changes are not due to infrared line absorptions (in contrast with the cooling rate response), but are exclusively a consequence of SO_2 UV absorption shortward of 0.32 µm (cf. Fig. 12). Episodic dramatic abundance boosts may quite strongly influence solar heating near 65 km, but this seems to be balanced out by thermal cooling. The SO_2 effect at higher altitudes under normal conditions is rather small and does not exceed 0.1 K/day.

Except for episodic SO_2 boosts, the overall response of the radiative energy balance on minor gas variations is rather small in the mesosphere, but minor gas influences should be properly considered in the cloud bottom range near 48 km.

5.3.3. Cloud parameters

Present discussions of cloud influences on the radiative energy balance are restricted to individual parameter variations like changes of mode factors and upper scale height. The systematic latitudinal dependence of these parameters as retrieved by Haus et al. (2013a; 2014a) is not considered at this point. Fig. 33 illustrates the change of cooling and heating rates in absolute values (displays A and B) and changes of the differences ΔQ(X, Initial) (displays C-F) at the equator when individual cloud mode factors (MF_j), mode 2 upper scale height ($H_{up}(2)$), and the altitude range of mode 2 location are independently modified. The definition of ΔQ for heating and cooling with respect to parameter variations was given in Section 5.2.1. The calculations use the hemispheric average temperature model HA (cf. Fig. 4). Heating rates are determined as diurnal averages. Mode 1 and mode 2 factors tend to be smaller compared with the initial value of unity according to recently obtained retrieval results (Haus et al., 2013a; 2014a), while the mode 3 factor rather increases up to more than 2.0. The cloud top altitude z_t tends to decrease with latitude. This is modeled here by decreasing the upper scale height H_{up} of mode 2 particles. Another quite realistic scenario investigates a downward shift of the mode 2 particle density distribution by reducing the parameter z_b (lower base of peak altitude) from 65 km (cf. Table 1) to 62 km. The resulting opacity and z_t changes are summarized in Table 5. Note that the mode 2 shift does not change the cloud opacity, while doubling of mode 2' and 3 factors does not change the cloud top altitude.

There is little response of both cooling and heating rates to abundance changes of mode 1 particles. Responses do not exceed 0.12 K/day at 70 km and become much smaller above and below this level. The detailed structure of the upper haze and the mode 1 influences in the lower mesosphere are not very important in energy balance calculations, at least when relying on its assumed chemical composition and density altitude profile used in the present model. In previous radiative balance studies (e.g. Pollack et al., 1980; Crisp, 1986), the UV absorber was assumed to be associated with mode 1 particles, and it was modeled by reducing their single scattering albedo in the spectral range 310-780 nm, that is, as an impurity of mode 1 particles. The so modified extinction and single scattering albedo characteristics of mode 1 led to much stronger influence on the radiative balance. The present approach separates features of the unknown UV absorber from mode 1 extinction altitude profiles and models the UV absorber as an independent species. Due to the above discussed small influence of pure H_2SO_4 aerosols in mode 1, this approach is regarded to be equivalently useful.

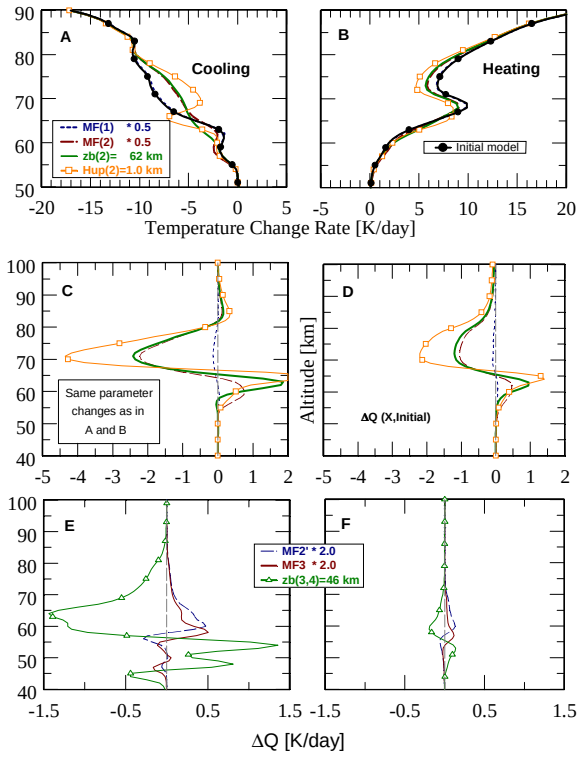

Figure 33. Response of temperature change rates Q to variations of cloud parameters. A, B: Absolute Q values for upper cloud parameter changes; C, D: deviations ΔQ for upper cloud parameter changes; E, F: deviations ΔQ for lower cloud parameter changes. Latitude 0°, diurnal average in case of heating, temperature profile HA from Fig. 4. Notations in the legends correspond to notations in Table 1.

The responses to changes of mode 2 parameters are much stronger. When MF_2 is reduced by 50%, cooling near 70 km (display C) becomes smaller by about 2 K/day compared with the initial model. It is larger by 0.5-0.7 K/day near 60 km. Small changes at high altitudes indicate that even the 'distant upper wing' of the mode 2 abundance

Table 5. Opacity and cloud top altitudes for different cloud parameters.

	Initial	MF_1=0.5	MF_2=0.5	$MF_{2'}$=2.0	MF_3=2.0	$z_b(2)$=62.0	$H_{up}(2)$=1.0
COD	35.00	33.05	31.19	44.34	49.14	35.00	32.49
z_t	70.81	70.59	68.83	70.81	70.81	68.40	66.65

MF_j: cloud mode factor, z_b [km]: lower base of mode peak altitude, H_{up} [km]: mode upper scale height,
COD: total column optical depth (opacity) at 1 µm, z_t: cloud top altitude (unity optical depth at 1 µm). See Table 1.

distribution has some influence there (cf. Fig. 24A, reduced cloud influence yields more cooling). The heating (display D) response behaves similar, but with smaller changes. Maximum deviations due to smaller heating values are in the order of 1 K/day near 70 km. A generally stronger response of both cooling and heating rates is found when the entire mode 2 altitude distribution is shifted downward by 3 km. This may happen in particular at polar latitudes, but applying this shift at the equator does not affect the principal conclusions. Corresponding calculations for other latitudes yield similar deviations. A lower peak altitude of mode 2 particles is comparable with a reduction of its mode abundance at altitudes above 65 km. The deviations between 60 and 65 km are larger for the shift case compared with halving mode 2 abundances, since the maximum cloud mode 2 influence is now located at 62 km instead of 65 km. A decrease of cloud mode 2 upper scale height by 2.5 km (3.5 km is the default value) that was retrieved from high latitude VIRTIS data analyses causes the largest temperature change rate responses with respect to mode 2 variations (displays C+D). Maximum influence with more than 4 K/day less cooling and about 2 K/day less heating is found again at 70 km due to the reduced aerosol amount around this altitude.

Displays E and F show cooling and heating responses to changes of mode 2' and mode 3 parameters. The doubling of mode factors generates more cooling (0.5 K/day) and more heating (~0.15 K/day) around 60 km, but much smaller changes at the cloud bottom. Strongest changes (up to -1.5 K/day for cooling near 65 km) are detected when the entire mode 2' and 3 altitude distributions are shifted downward by 3 km (49 km is the default value of the lower boundaries of constant peak abundances, z_b). It is interesting to observe that changes of lower cloud parameters may still have some weak influence on thermal cooling at altitudes above 70 km. The heating response to mode 2' and mode 3 abundance changes is much smaller due to the small amount of solar radiation that is available below 65 km. There is no heating rate change at altitudes above 70 km.

Variations of Q by 1 K/day at 60 km or 4 K/day at 70 km (display C) correspond to about 50% of the nominal Q^C values at these altitudes and are very significant, therefore. These comparatively strong changes and the specific curvature mainly in the cooling rate profiles result from distinct altitude-dependent changes of downward and upward fluxes and the resulting change of net flux divergences. The general influence of the cloud deck on thermal radiative fluxes through the atmosphere is an increase of the downward flux component due to increasing atmospheric layer optical depths. Upward fluxes that include contributions from the hot underlying layers suddenly start to diverge from a hypothetical cloud-free case just at the cloud base due to strong cloud extinction. When clouds were absent, much more upward radiation would reach the higher altitude levels.

Summarizing the discussed responses of radiative temperature change rates to cloud parameter variations, it can be stated that most variations are large enough to generate significant heating and cooling changes up to 50% in Venus' lower mesosphere and upper troposphere. Consideration of observed real variations of cloud parameters with latitude will strongly influence the overall energy balance compared with calculation results for the initial atmospheric model.

5.3.4. Unknown UV absorber

Fig. 34 illustrates the influence of different models of the unknown UV absorber (UVA) on the calculated heating rates (diurnal average at the equator, temperature profile HA). The UVA generally increases heating at altitudes 55-75 km (nominal high altitude model 1, 'H', cf. Table 3) and 55-69 km (low altitude model 2, 'L'), respectively. At 68 km, the nominal model provides about 4.5 K/day more heating than it would result from an exclusion of this opacity source (broken line) and thus, a doubling of solar heating rate. Changing the UVA-'H' abundance by a constant factor of two (without adjusting the albedo curve) yields the heating profile described by the solid line without symbol. The 'L' model was constructed to provide the same albedo curve as the 'H' model (cf. Section 3). Its maximum influence on the heating rates occurs at 63 km, and due to higher peak abundance concentration, the 'L' model causes a stronger heating below this level compared with the 'H' model. The extreme large maximum of the 'L' model shown by Crisp (1986) reaching almost 10 K/day at 63 km could not be verified by present calculations. It is probably due to the different cloud model used by Crisp.

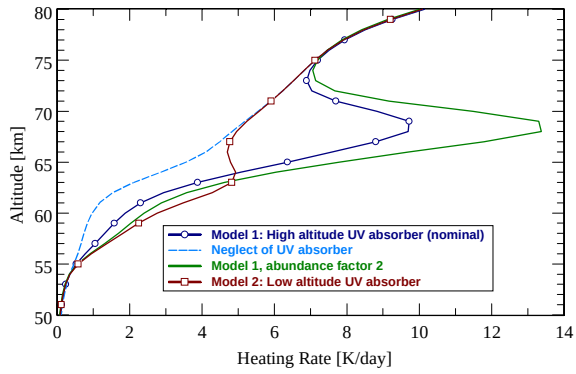

Figure 34. Response of heating rates to variations of the unknown UV absorber. Latitude 0°, diurnal average, temperature profile HA from Fig. 4.

In contrast with the two basic UVA models 'H' and 'L' that are constructed to produce the same spectral albedo profile, a change of UVA opacity in one of these altitude distribution models (that is, a change of UVA column abundance as shown in Fig. 34) may well reproduce observed bright and dark UV regions on the planet. This is the great advantage of the present model that simulates the unknown absorber as an agent that is independent of cloud microphysical parameters. This way, modeling of UV brightness variations can be easily achieved without costly on-line recalculations of cloud microphysical parameters by simple multiplication of the UVA number density profile (cf. inset of Fig. 18) by a suitable factor. This procedure also modifies the spectral albedo curve shown in Fig. 17. Recall that spectral albedos resulting from different absorber distributions but from the same UVA absorption cross-section spectrum are not the same, since interferences with other atmospheric constituents shortward of about 800 nm (mainly clouds and SO_2) cause different vertical flux profiles.

5.3.5. Specific heat capacity

According to Eq. (25) and following the discussion performed in Section 5.3.2, the two parameters air density ρ and specific heat capacity c_p are of crucial importance for the calculation of radiative temperature change rates, and possible variations may influence the numerical results. ρ according to Eq. (24) is always calculated considering actual (latitude-dependent) temperature and pressure values at each altitude where pressures are determined from the barometric formula using a mean surface pressure of 92.1 bar at zero elevation. The mean molecular weight M of Venus' atmosphere in Eq. (24) is derived using the carbon dioxide / nitrogen abundance ratio of 96.5% / 3.5 % leading to M = 43.44 g mol^{-1} compared with a pure CO_2 atmosphere (M = 44 g mol^{-1}). In contrast with quantity ρ, the heat capacity c_p in Eq. (23) refers to a pure CO_2 atmosphere. According to Crisp (1986), Eq. (23) was derived by least-square fitting to laboratory measurements of c_p at temperatures between 200 and 590 K and should be accurate to 0.5% throughout that range (that is between about 20 and 80 km on Venus). At temperatures 170-200 K (80-95 km), the error was estimated to remain < 1%.

At standard temperature and pressure condition (T_S=300 K, p_S=1 atm), CO_2 and N_2

exhibit c_p values of 846 and 1040 Ws kg^{-1} K^{-1}, respectively (www.engineeringtoolbox.com). A mixture according to the above given abundance ratio would produce c_p^{mix}=853 Ws kg^{-1} K^{-1}, and thus, a value being only about 1% larger than for pure CO_2, which is assumed to be valid also at other altitudes. Larger c_p values result in smaller temperature change rates. Test calculations have shown that an estimated c_p error of 1% at any altitude does not change the cooling/heating rates below 45 km. At 65 km, a cooling change of 0.02 K/day occurs, while heating decreases by about 0.1 K/day. Moving to higher altitudes, c_p influences become larger, but the rates do not decrease by more than 0.25 K/day, which is the estimated accuracy limit of cooling rates below 95 km and heating rates below 85 km due to spectroscopic parameter influences as described above in the summary at the end of Section 5.2.4.

5.4. Comparison with earlier results and a preliminary sketch of net radiative heating

Fig. 35 compares present results on globally averaged heating and cooling rates with earlier results from the literature (Crisp, 1986; Crisp, 1989; Tomasko et al., 1985; Lee and Richardson, 2011; Haus and Goering, 1990). The data points are extracted from the corresponding plots in the papers and are not guaranteed to be fully correctly represented in the figure. The discussion is strongly hampered by the fact that any of these investigations used different atmospheric and spectroscopic model parameters. The spectral ranges that are taken into account, the used solar irradiance spectra, and the definition of TOA altitude also differ. It is not always clear from the given information whether global averages are generated by use of cosine weighting or not. Thus, it is not possible to compare the results in detail. Moreover, present results are preliminary, since latitude-dependent changes of cloud features are not considered. This may partly explain the large differences even between literature results. If for example a cloud abundance factor of two was used (that is, all modes of the present initial model are simultaneously multiplied by this factor), a cooling profile was obtained that was more comparable to the profile of Lee and Richardson (2011) below 70 km. This would correspond to the responses shown in Figs. 33C and E. Note that 33C illustrates mode 2 response to a factor halving. According to Figs. 33D and F, the heating profile however would also show larger values above 65 km and smaller values below this altitude. The general conclusion is again that variations of cloud model parameters may result in significant changes of calculated temperature change rates. In any case, thermal cooling rates much stronger depend on cloud parameter variations than solar heating rates do.

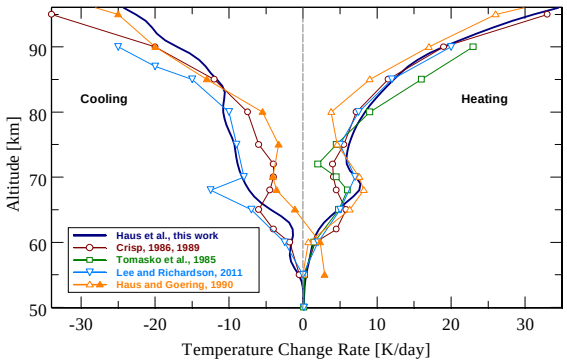

Figure 35. Comparison of globally averaged cooling and heating rates with results from the literature.

At altitudes above 90 km, the applied definition of TOA altitude (z^{TOA}) becomes very important. Both cooling and heating rates would be strongly in error for z^{TOA}=100 km, resulting in Q^C(100 km)=66 K/day, Q^H(100 km)=120 K/day. This is due to changes in the downward and upward directed flux components, since CO_2 IR and UV absorptions wouldn't be sufficiently considered in this case. In case of cooling, the thermal downward component becomes smaller and leads to an increase of net flux and net flux divergence. In the solar spectral range, both total downward flux and diffuse upward flux increase, but the downward component increases faster leading again to larger net fluxes and divergences above 90 km. Setting z^{TOA} to 110 km still provides cooling and heating differences at 100 km of 0.9 and 2.2 K/day, respectively. The differences almost disappear for z^{TOA}=120 km (0.03 and 0.11 K/day). Present studies use z^{TOA}=140 km.

Fig. 36 provides a very preliminary sketch of net radiative forcing as function of latitude and altitude (display A). Note that the step between isolines varies. It is selected to ensure optimum graphical representation. Display B shows the altitude profile of globally averaged net radiative heating where the latitude weighting according to Eq. (20) is not used. This enables a better comparison with display A. The results are based on the initial atmospheric parameter model. Latitudinal variations of cloud features are not considered here. There is a narrow altitude range at the cloud base (48-49 km) where weak net heating of about 0.5 K/day occurs. This heating is slightly stronger at low latitudes. In the deep atmosphere below this altitude, zero net heating prevails that is only interrupted between 35 and 43 km by a layer of very weak net cooling. Thus, the troposphere of Venus is in nearly complete radiative energy balance. The picture changes in the middle cloud layers and above. A planet-wide weak cooling layer occurs near 57 km. A second, much broader cooling region exists between 72 and 80 km, but there is a strong increase of cooling toward the pole up to 14 K/day. This net gradient is also observed at 65 km where heating prevails at low latitudes. At altitudes above 80 km, net heating dominates the low and mid latitudes, while net cooling prevails at high latitudes. Net heating may reach more than 30 K/day at the equator at 100 km. The transition region between net heating and net cooling above 80 km moves with increasing altitude from 60° to 80°.

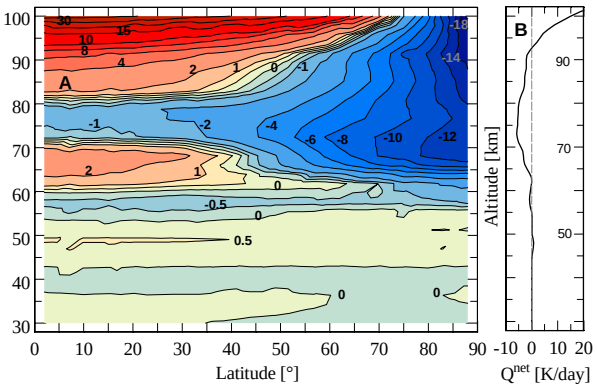

Figure 36. A: Net radiative forcing in the atmosphere of Venus [K/day] as function of latitude and altitude for the initial atmospheric parameter model. B: Global average of net radiative forcing (no latitude weighting).

Generally speaking, the net radiative forcing field in the Venus mesosphere at altitudes between 60 and 100 km is characterized by net solar heating at low and mid latitudes and net thermal cooling at high latitudes, while the lower mesosphere and troposphere are almost in radiative balance. Net cooling at higher latitudes is due to reduced solar insolation in combination with the warmer atmosphere. These results well agree with previous findings (e.g. Crisp, 1989; Titov et al., 2007; Lee et al., 2015), although some details are quite different. The present study predicts the existence of a planet-wide cooling layer between 72-80 km with equatorial and low latitude cooling of about 1-3 K/day and polar cooling of 12-14 K/day at 77 km, while recent findings by Lee et al. (2015) (for altitudes 55-80 km) have shown this layer to be centered at 69 km. Thus, the general mesospheric transition region between net cooling and heating near 40-45° as reported by these authors is not observed here, but it is well discernible in Fig. 36 at altitudes 60-70 km and 80-90 km, respectively. Local cooling minima at high latitudes centered near 70 km are recognized in both studies, but the existence of some weak net heating spots at 57-60 km in the cold collar region (60-80°) cannot be verified by present findings. Differences between these results can be most likely explained by the different atmospheric model assumptions where the studies are based on. Apart from different assumed thermal structure models (Lee results are based on VeRa data (Tellmann et al. (2009)), Lee et al. (2015) have used a very different cloud model. The only cloud mode particles that were assumed to be present at altitudes above 60 km belong to mode 2 particles. Thus, neither upper haze and higher altitude mode 1 particles nor larger mode 2' particles above 60 km were considered. On the other hand, these authors have carefully investigated the change of mode 2 abundances and resulting cloud top location with latitude what is not yet done in the present study. Consideration of cloud top altitude and individual mode abundance variations with latitude (as recently retrieved by Haus et al. (2014a) using a very similar initial cloud model as the one described in

Section 2.4.2, Fig. 6) and subsequent comparisons with literature results remain one of the most thrilling issues of a follow-up paper.

The atmospheric thermal structure used to calculate the net radiative forcing field (VIRA-N in the present study) can only be maintained by dynamical processes. A possible mechanism would involve a pole-to-equator meridional circulation, rising motion at low latitudes, poleward heat flow (being especially strong near the mesopause), and subsidence at high latitudes (Crisp, 1989).

6. Summary and conclusions

A radiative transfer simulation model (RTM) that includes the discrete ordinate package DISORT is applied to calculate radiance and flux spectra in dependence on atmospheric and spectroscopic parameters and for different solar spectrum models. The RTM considers absorption, emission, and multiple scattering by gaseous and particulate constituents over the broad spectral range 0.125-1000 µm. The individual contributions of these constituents at infrared (0.7-1000 µm), visible (0.4-0.7 µm), and ultraviolet (0.1-0.4 µm) wavelengths are investigated (Figs. 8-10, Fig. 15). Infrared continuum absorption and molecular Rayleigh scattering are also addressed (Figs. 13, 14). Look-up tables of quasi-monochromatic absorption cross-sections of gaseous constituents are calculated in the infrared and visible spectral ranges on the basis of a line-by-line procedure for a variety of temperature and pressure values being representative for Venus' atmosphere at altitude levels between the surface and 140 km. These tables are generated for different sets of spectroscopic parameters including very fine spectral sampling steps down to 0.0001 cm^{-1} (Fig. 25), different spectral line catalogs, and variations of line profiles with respect to line cut and sub-Lorentz structure.

The atmospheric models required for RTM operation encompass altitude profiles of temperature, minor gas abundances, and cloud mode particle densities as well as cloud mode composition. Initial models are selected for present studies. The thermal structure of Venus' atmosphere is described by latitude-dependent temperature altitude profiles that are merged from the VIRA-1 and VIRA-2 data sets assuming identical thermal regimes on the nightside and dayside of the planet up to 95 km. A characteristic dayside profile is considered above 95 km (Fig. 4). The initial minor constituent altitude distribution model is similar to that described by Tsang et al. (2008) (Fig. 5). Possible variations with latitude as recently retrieved by Haus et al. (2015) are not considered here. The initial cloud model (Haus et al., 2013a) facilitates analytical descriptions of four-modal particle altitude distributions (Fig. 6) where all modes are assumed to consist of spherical H_2SO_4 aerosols at 75 wt% solution. Mie scattering theory is applied to derive wavelength-dependent microphysical parameters of each mode. The clouds of Venus may strongly change in terms of total abundance and altitude distribution of particulate constituents leading to variations of cloud top and base altitudes as well as total cloud opacity. Present studies are devoted to a detailed analysis of individual cloud mode parameter influences rather than applying parameter fields that have been retrieved from VIRTIS-M-IR data (Haus et al., 2013a, 2014a). This ensures a better understanding of possible mode-dependent responses of calculated output quantities with respect to the atmospheric energy balance.

Using available measurements of Venus' spectral Bond albedo, a new model for the unknown UV absorber is developed. This species being located at altitudes between 57 and 70 km is required to fit the observations shortward of 0.8 µm down to 0.32 µm, while SO_2 UV absorption provides sufficient opacity at shorter wavelengths. Present calculations also include UV absorptions by CO_2, H_2O, OCS, and HCl shortward of 0.3 µm (Figs. 11, 12). CO_2 dominates these absorptions. The new UV absorber model is not directly linked to cloud particle modes 1 or 2, and thus, permits an investigation of its radiative effects regardless of chemical composition. By analogy with a previously proposed model of Crisp (1986), two different altitude

distribution (and resulting absorption cross-section) models are assumed. Based on these profiles, altitude-independent absorption cross-section spectra are calculated ('retrieved') that yield good fits of the Bond albedo spectrum presented by Moroz (1981) (Figs. 17, 18). Both models provide a globally averaged Bond albedo of 0.763 in excellent agreement with Moroz et al. (1985).

Downward and upward directed radiation fluxes inside the atmosphere as well as resulting net fluxes and net flux divergences with respect to altitude are calculated based on quasi-monochromatic absorption and scattering properties of all atmospheric constituents. These calculations are performed separately for thermal (1.67-1000 µm, 10-6000 cm^{-1}) and solar (0.125-1000 µm, 10-80000 cm^{-1}) flux components. Wavelength-integrated quantities and diurnal averages (Figs. 20, 21) are then used to determine temperature change rates at each altitude in terms of thermal cooling rates and solar heating rates (Fig. 23). Contributions of individual atmospheric constituents as well as contributions of different CO_2 absorption bands to the total temperature change rates are determined (Figs. 24, 27). On global average, half of the solar flux received at the top of atmosphere (F^{TOA-GA}=667 Wm^{-2}) is either absorbed or redistributed by CO_2 and cloud mode 1 and 2 particles at altitudes above 74 km. The sum of direct and diffuse downward solar fluxes attains the 50% level of TOA flux at 55 km where the unknown UV absorber has made a major contribution of about 15%. Half of the solar flux deposited on the planet at TOA altitude (140 km) is absorbed by atmospheric constituents at altitudes above 63 km. Less than 5% of solar TOA flux (30 Wm^{-2}) reaches the surface. The thermal downward flux near the surface is 16.5 kWm^{-2}. The global average of solar flux deposited on the planet (the solar net flux at TOA) is 158.1 Wm^{-2}, and the outgoing globally averaged thermal net flux is 159.7 Wm^{-2} for the present initial atmospheric standard model (Figs. 20, 21). Thus, these net fluxes differ by about 1.5 Wm^{-2} around the mean value of 159 Wm^{-2}, which very well corresponds to the value of (157±6) Wm^{-2} reported by Titov et al. (2007). Considering the uncertainties in both TOA values, this discrepancy should not be interpreted as an indication of global radiative imbalance. Exact TOA global radiative equilibrium can be achieved by moderate adjustments of cloud mode and UV absorber abundances. There is a general trend of decreasing solar flux with increasing distance from equator, while the outgoing thermal flux shows a peculiarity of Venus compared with Earth and Mars. It only weakly decreases between 30° and 60°, but then increases again toward the poles (Fig. 22).

The responses of net fluxes and temperature change rates to variations of spectroscopic parameters are studied in great detail to provide estimates of their uncertainties with respect to individual parameters. The use of CO_2 absorption cross-section databases at a spectral wavenumber grid step (often called point distance PD here) of 0.01 cm^{-1} is sufficiently accurate. Differences compared with higher resolution databases are usually less than 0.01 K/day at altitudes below 90 km and do not exceed 0.3 K/day at 100 km (Fig. 26A). Based on a careful separation of spectral ranges that are dominated by more or less strong gaseous absorption bands, an optimum PD grid is developed that considerably accelerates the time expensive monochromatic flux calculations without introducing significant accuracy losses. Individual spectral ranges outside the strong absorption bands can be modeled by using coarser PD grids of 0.1, 1.0 and even 10 cm^{-1}. Maximum deviations from the reference PD (0.01 cm^{-1}) of both cooling rates and heating rates at the subsolar point are smaller than ±0.1 K/day below 85 km. At 100 km, solar heating rate deviations may reach +2.3 K/day, but the uncertainties of diurnally averaged heating rates are much smaller (Fig. 26B). Using the optimum PD grid and pre-calculated absorption cross-sections, a RTM run over either the thermal or solar spectral range for one latitude (and one solar zenith angle in case of heating) takes about 360 s, but further optimizations of some procedures are still possible.

Largest uncertainties of temperature change rates result when different spectral line

catalogs are used. Compared with the default dataset HITRAN 2008, HITEMP 2010 for example would produce 3 K/day less heating and 0.3 K/day more cooling at 100 km, while the deviations with respect to net heating would partly compensate between 70 and 90 km (Fig. 28). The use of different sub-Lorentz profiles and line cut conditions does not significantly alter cooling and heating results above 50 km, but for accurate thermal flux and cooling rate calculations in the region of the cloud base (48 km) the use of a line cut condition of at least 250 cm^{-1} is recommended (Fig. 29). It can be concluded that the calculated cooling and heating rates are very reliable at altitudes below 85 km with maximum uncertainties of about 0.25 K/day. Cooling uncertainties do not increase between 85 and 95 km, but heating uncertainties may reach 3-5 K/day at 100 km. The use of equivalent Planck radiation as solar insolation source in place of measured spectra should be avoided, since it seriously overestimates solar heating shortward of 0.4 µm (Fig. 30).

There is a very strong response of cooling rates to variations of atmospheric thermal structure, while heating rates are less sensitive (Fig. 31). Temperature variations with latitude and local time have to be carefully taken into account when calculating two- or three-dimensional net heating rates. Except for observed episodic strong SO_2 abundance boosts, the overall response of the radiative energy balance on minor gas variations is rather small in the mesosphere, but minor gas variations (especially H_2O and SO_2) near the cloud base may become very important and should be properly considered (Fig. 32). The influence of mode 1 cloud particles is found to be comparatively small. When their column abundance is halved, both cooling and heating responses do not exceed 0.12 K/day at 70 km with decreasing tendency toward higher and lower altitudes. On the other hand, changes of mode 2, 2', and 3 parameters (cloud top and base altitudes, total mode abundances, upper scale height) may significantly alter radiative temperature change rates up to 50% in Venus' lower mesosphere and upper troposphere (Fig. 33). The new nominal model for the unknown UV absorber provides about 50% more heating at 68 km compared with a neglect of this opacity source (Fig. 34).

Present results on globally averaged heating and cooling rates reveal basic conformity with earlier results from the literature (Fig. 35), although details are different. This is due to the fact that each of these investigations used different atmospheric and spectroscopic model parameters. Present methodology and sensitivity studies do not yet consider variations of cloud features with latitude that may result in significant changes of calculated temperature change rates.

The very detailed investigation of responses of net fluxes and temperature change rates to variations of atmospheric model parameters provides valuable estimates of possible changes that can be expected when individual parameters are varied. Present results on globally averaged radiative heating and cooling rates and net radiative forcing in the atmosphere of Venus as function of latitude and altitude should be regarded as preliminary sketches, however, since real (and often simultaneous) variations of cloud parameters are not considered yet. According to these preliminary results (Fig. 36), there is a broad net cooling region between 70 and 80 km with a strong increase of cooling toward the poles. A net rate gradient is also observed at 65 km where heating prevails at low latitudes. At altitudes above 80 km, net heating dominates the low and mid latitudes, while net cooling prevails at high latitudes leading to a dominant global average net heating. The observed thermal structure in the Venus mesosphere can only be maintained by dynamical processes.

Future studies will consider improved models of middle and lower atmospheric parameters of Venus that have been retrieved from VIRTIS-M-IR data (Haus et al., 2013a; 2014a; 2015) with respect to latitude and local time dependent thermal structure and meridional variations of cloud features and minor gas distributions. These investigations will compare latitude-altitude fields of cooling and heating rates obtained for the presently used initial thermal model (VIRA) with the VIRTIS retrievals. They are also intended for

comparisons with VeRa, VMC, and SPICAV data and recent analyses of the cloud structure from VeRa/VIRTIS observations by Lee et al. (2015). Variations of cloud mode abundances and cloud top and base altitudes are expected to considerably alter the results on atmospheric radiative energy balance of Venus.

Acknowledgments

This work is funded by the German Research Foundation under Grant number HA 2887/2-2.

References

Arking, A., 1996. Absorption of solar energy in the atmosphere: Discrepancy between model and observation. Science 273(5276), 779-782, http://dx.doi.org/10.1126/science.273.5276.779.

Arnold, G., Haus, R., Kappel, D., Piccioni, G., Drossart, P., 2012. VIRTIS/VEX observations of Venus: Overview of selected scientific results. J. Appl. Remote Sensing 6, 20 pp., http://dx.doi.org/10.1117/1.JRS.6.063580.

ASTM Standard E490-00a, 2006. Solar constant and zero air mass solar spectral irradiance tables. Available at: (http://dx.doi.org/10.1529/E0490-00AR06 and http://rredc.nrel.gov/solar/spectra/am0/).

Avduevsky, V.S., Marov, M.Y., Kulikov, Y.N., Shari, V.P., Gorbachevsky, A.Y. et al., 1983. Structure and parameters of the Venus atmosphere according to Venera probe data. In *Venus*, Hunten, D.M., Colin, L., Donahue, T.M., Moroz, V.I. (Eds.), pp. 280-298, University of Arizona Press, Tucson.

Barker, E.S., Woodman, J.H., Perry, M.A., Hapke, B.A., Nelson,R., 1975. Relative spectrophotometry of Venus from 3067 to 5960 A°. J. Atmos. Sci.32(6), 1205-1211, http://dx.doi.org/10.1175/1520-0469(1975)032<1205:RSOVFT>2.0.CO;2.

Bézard, B., de Bergh, C., Crisp, D., Maillard, J.P., 1990. The deep atmosphere of Venus revealed by high-resolution nightside spectra. Nature 345, 508-511, http://dx.doi.org/10.1038/345508a0.

Bézard, B., de Bergh, C., 2007. Composition of the atmosphere of Venus below the clouds. J. Geophys. Res. 112(E04S07), http://dx.doi.org/10.1029/2006JE002794.

Bézard, B., Tsang, C.C.C, Carlson R.W., Piccioni, G., Marcq, E., Drossart, P., 2009. Water vapor abundance near the surface of Venus from Venus Express / VIRTIS observations. J. Geophys. Res. 114(E00B39), http://dx.doi.org/10.1029/2008JE003251.

Bézard, B., Fedorova, A., Bertaux, J.L., Rodin, A., Korablev, O., 2011. The 1.10- and 1.18-µm nightside windows of Venus observed by SPICAV-IR aboard Venus Express. Icarus 216, 173-183, http://dx.doi.org/10.1006/j.icarus.2011.08.025.

Burch, D.E., Gryvnak, D.A., Patty, R.R., Bartky, C.E., 1969. Absorption of infrared radiant energy by CO_2 and H_2O. IV. Shapes of collision-broadened CO_2 lines. J. Opt. Soc. Am. 59(3), 267-278, http://dx.doi.org/10.1364/JOSA.59.000267.

Carlson, R.W. and Anderson, M.S., 2011. Absorption properties of sulfuric acid in Venus' infrared spectral window region. In: EPSC Abstracts 6, EPSC-DPS2011-1171.

Chan, W.F., Cooper, G., Sodhi, R.N.S., Brion, C.E., 1993. Absolute optical oscillator strengths for discrete and continuum photoabsorption of molecular nitrogen (11-200 eV). Chem. Phys. 170(1), 81-97, http://dx.doi.org/10.1016/0301-0104(93)80095-Q.

Crisp, D., 1986. Radiative forcing of the Venus mesosphere: I. Solar fluxes and heating rates. Icarus 67(3), 484–514, http://dx.doi.org/10.1016/0019-1035(86)90126-0.

Crisp, D., 1989. Radiative forcing of the Venus mesosphere: II. Thermal fluxes, cooling rates, and radiative equilibrium temperatures. Icarus 77(2), 391–413, http://dx.doi.org/10.1016/0019-1035(89)90096-1.

Crisp, D. and Titov, D.V., 1997. The thermal balance of the Venus atmosphere. In *Venus-II: Geology, Geophysics, Atmosphere, and Solar Wind Environment*, Bougher, S.W., Hunten, D.M., Phillips, R.J. (Eds.), 353–384, University of Arizona Press, Tucson. ISBN-13: 978-0816518302.

de Bergh, C., Bézard, B., Owen, T., Crisp, D., Maillard, J.P., Lutz, B.L., 1991. Deuterium on Venus: Observations from Earth. Science 251(4993), 547-549, http://dx.doi.org/10.1126/science.251.4993.547.

de Bergh, C., Bézard, B., Crisp, D., Maillard, J.P., Owen, T. et al., 1995. Water in the deep atmosphere of Venus from high-resolution spectra of the night side. Adv. Space Res. 15(4), 79-88, http://dx.doi.org/10.1016/0273-1177(94)00067-B.

Delaye, C., Hartmann, J.M., Taine, J., 1989. Calculated tabulations of H_2O line broadening by H_2O, N_2, O_2, and CO_2 at high temperature. Appl. Opt. 28(23), 5080-5087, http://dx.doi.org/10.1364/AO.28.005080.

Drossart, P., Piccioni, G., Adriani, A., Angrilli, F., Arnold, G. et al., 2007. Scientific goals for the observation of Venus by VIRTIS on ESA/Venus

express mission. Planet. Space Sci. 55(12), 1653-1672, http://dx.doi.org/10.1016/j.pss.2007.01.003.

Ekonomov, A.P., Moshkin, B.E., Moroz, V.I., Golovin, I.U., Gnedykh, V.I., Grigoriev, A.V., 1983. The UV-photometry experiment on the Venera-13 and Venera-14 descent modules (in Russian). Kosm. Issled. 21(2), 254-268.

Esposito, L.W., Copley, M., Eckert, R., Gates, L., Stewart, A.I.F., Worden, H., 1988. Sulfur dioxide at the Venus cloud tops, 1978-1986. J. Geophys. Res. 93(D5), 5267-5276, http://dx.doi.org/10.1029/JD093iD05p05267.

Esposito, L.W., Bertaux, J.L., Krasnopolsky, V., Moroz, V.I., Zasova, L.V., 1997. Chemistry of lower atmosphere and clouds. In: *Venus-II: Geology, Geophysics, Atmosphere, And Solar Wind Environment*, Bougher, S.W., Hunten, D.M., Phillips, R.J. (Eds.), 415-458, University of Arizona Press, Tucson. ISBN-13: 978-0816518302.

Fukabori, M., Nakazawa, T., Tanaka, M., 1986. Absorption properties of infrared active gases at high pressures- I. CO_2, J. Quant. Spectrosc. Radiat. Transfer 36(3), 265-270, http://dx.doi.org/10.1016/0022-4073(86)90074-9.

Grassi, D., Migliorini, A., Montabone, L., Lebonnois, S., Cardesin-Moinelo et al., 2010. Thermal structure of Venusian nighttime mesosphere as observed by VIRTIS-Venus Express. J. Geophys. Res. 115 (E09007), 11 pp., http://dx.doi.org/10.1029/2009JE003553.

Grassi, D., Politi, R., Ignatiev, N.I., Plainaki, C., Lebonnois, S. et al., 2014. The Venus nighttime atmosphere as observed by the VIRTIS-M instrument. Average fields from the complete infrared data set. J. Geophys. Res. 119(4), 837-849, http://dx.doi.org/10.1002/2013JE004586.

Hansen, J.E. and Travis, L.D., 1974. Light scattering in planetary atmospheres. Space Sci. Rev. 16(4), 527-610, http://dx.doi.org/10.1007/BF00168069.

Hartmann, J.M., Rosenmann, L., Perrin, M.Y., Taie, J., 1988. Accurate calculated tabulations of CO line broadening by H_2O, N_2, O_2, and CO_2 in the 200-30000-K temperature range. Appl. Opt. 27(15), 3063-3065, http://dx.doi.org/10.1364/AO.27.003063.

Haus, R. and Goering, H., 1990. Radiative energy balance in the Venus mesosphere. Icarus 84(1), 62–82, http://dx.doi.org/10.1016/0019-1035(72)90009-7.

Haus, R. and Titov, D.V., 2000. PFS on Mars Express: Preparing the analysis of infrared spectra to be measured by the Planetary Fourier Spectrometer. Planet. Space Sci. 48(12-14), 1357-1376, http://dx.doi.org/10.1016/S0032-0633(00)00116-1.

Haus, R. and Arnold, G., 2010. Radiative transfer in the atmosphere of Venus and application to surface emissivity retrieval from VIRTIS/VEX measurements. Planet. Space Sci. 58(12), 1578-1598, http://dx.doi.org/10.1016/j.pss.2010.08.001.

Haus, R., Kappel, D., Arnold, G., 2013a. Self-consistent retrieval of temperature profiles and cloud structure in the northern hemisphere of Venus using VIRTIS/VEX and PMV/VENERA-15 radiation measurements. Planet. Space Sci. 89, 77-101, http://dx.doi.org/10.1016/j.pss.2013.09.020.

Haus, R., Kappel, D., Arnold, G., 2013b. Investigation of Venus' atmospheric thermal structure and cloud features over the northern nightside hemisphere applying self-consistent retrieval procedures. In: EPSC Abstracts 8, EPSC2013-270.

Haus, R., Kappel, D., Arnold, G., 2014a. Atmospheric thermal structure and cloud features in the southern hemisphere of Venus as retrieved from VIRTIS/VEX radiation measurements. Icarus 232C, 232-248, http://dx.doi.org/10.1016/j.icarus.2014.01.020.

Haus, R., Kappel, D., Arnold, G., 2014b. Atmospheric thermal structure and cloud features of Venus as retrieved from VIRTIS/VEX measurements. In: EPSC Abstracts 9, EPSC2014-7-1.

Haus, R., Kappel, D., Arnold, G., 2015. Lower atmosphere minor gas abundances as retrieved from Venus Express VIRTIS-M-IR data at 2.3 µm. Planet. Space Sci. 105, 159-174, http://dx.doi.org/10.1016/j.pss.2014.11.020.

Imamura, T. and Hashimoto, G.L., 1998. Venus cloud formation in the meridional circulation. J. Geophys. Res. 103(E13), 31349-31366, http://dx.doi.org/10.1029/1998JE900010.

Imamura, T. and Hashimoto, G.L., 2001. Microphysics of Venusian clouds in rising tropical air. J. Atmos. Sci. 58(23), 3597-3612, http://dx.doi.org/10.1175/1520-0469(2001)058<3597:MOVCIR>2.0.CO;2.

Inn, E.C.Y., 1975. Absorption Coefficient of HCl in the Region 1400 to 2200 A°. J. Atmos. Sci. 32(12), 2375-2377, http://dx.doi.org/10.1175/1520-0469(1975)032<2375:ACOHIT>2.0.CO;2.

Irvine, W.M., 1968. Monochromatic phase curves and albedos for Venus. J. Atm. Sci.25(4), 610-616, http://dx.doi.org/10.1175/1520-0469(1968)025<0610:MPCAAF>2.0.CO;2.

Irvine, W.M., 1975. Multiple scattering in planetary atmospheres. Icarus 25, 175-204, http://dx.doi.org/10.1016/0019-1035(75)90019-6.

James, E.P., Toon, O.B., and Schubert, G., 1997. A numerical microphysical model of the condensational Venus clouds. Icarus 129(1), 147-171,

http://dx.doi.org/10.1006/icar.1997.5763.

Jones, A.D., 1976. Optical constants of sulphuric acid in the far infrared. J. Quant. Spectrosc. Radiat. Transfer 16(12), 1017-1019, http://dx.doi.org/10.1016/0022-4073(76)90130-8.

Kappel, D., Arnold, G., Haus, R., Piccioni, G., and Drossart, P., 2012. Refinements in the data analysis of VIRTIS-M-IR Venus nightside spectra. Adv. Space Res. 50(2) 228-255, http://dx.doi.org/10.1016/j.asr.2012.03.029.

Kappel, D., 2014. MSR, a multi-spectrum retrieval technique for spatially-temporally correlated or common Venus surface and atmosphere parameters. J. Quant. Spectrosc. Rad. Transfer 133, 153-176, http://dx.doi.org/10.1016/j.jqsrt.2013.07.025.

Kappel, D., Haus, R., Arnold, G., 2015a. Error analysis for retrieval of Venus' IR surface emissivity from VIRTIS/VEX measurements. Planet. Space Sci. 113-114, 49-65, http://dx.doi.org/10.1016/j.pss.2015.01.014.

Kappel, D., Arnold, G., Haus, R., 2015b. Multi-spectrum retrieval of Venus IR surface emissivity maps from VIRTIS/VEX nightside measurements of Themis Regio. Icarus (submitted for publication).

Keating, G.M., Nicholson, J.Y. and Lake, L.R., 1980. Venus upper atmosphere structure. J. Geophys. Res. 85(A13), 7941-7956, http://dx.doi.org/10.1029/JA085iA13p07941.

Keating, G.M., Bertaux, J.L., Bougher, S.W., Cravens, T.E., Dickinson, R.E., et al., 1985. Models of Venus neutral upper atmosphere: Structure and composition. In: *The Venus International Reference Atmosphere*, Kliore, A. J., Moroz, V.I., Keating, G.M. (Eds.), Adv. Space Res. 5(11), 117-171 (1985), http://dx.doi.org/10.1016/0273-1177(85)90200-5.

Krasnopolsky, V.A., 2006. Chemical composition of Venus atmosphere and clouds: Some unsolved problems. Planet. Space Sci. 54, 1352-1359, http://dx.doi.org/10.1016/j.pss.2006.04.019.

Kurucz, R.L., 1995. The solar irradiance by computation. Proc. 17th Annual Conference Transmission Models, Phillips Laboratory, Hanscom AFB, PL-TR-95-2060. G.P. Anderson et al., Eds., pp . 333-334.

Kurucz, R.L., 2011. Available at: http://kurucz.harvard.edu/sun/.

Lee, C. and Richardson, M.I., 2011. A discrete ordinate, multiple scattering, radiative transfer model of the Venus atmosphere from 0.1 to 260 µm. J. Atmos. Sci. 68, 13223-1339, http://dx.doi.org/10.1175/2011JAS3703.1.

Lee, Y.J., 2012. Venus cloud structure and radiative energy balance of the mesosphere. *International Max Planck Research School on Physical Processes in the Solar System and Beyond at the Universities of Braunschweig and Göttingen*, Uni-Edition, 150 pp, ISBN 978-3942171687.

Lee, Y.L., Titov, D.V., Ignatiev, N.I., Tellmann, S., Pätzold, M., Piccioni, G., 2015. The radiative forcing variability caused by changes of the upper cloud vertical structure in the Venus mesosphere. Planet. Space Sci. 113-114, 298-308, http://dx.doi.org/10.1016/j.pss.2014.12.006.

Linkin, V.M., Blamont, J., Devjatkin, S.I., Ignatova, S.P., Kerzhanovich, V.V. et al., 1987. Thermal structure of the atmosphere of Venus from the results of measurements taken by landing vehicle Vega-2. Cosmic Res. 25, 501-512.

Manatt, S.L. and Lane, A.L., 1993. A compilation of the absorption cross-sections of SO_2 from 106 to 403 nm. J. Quant.Spectrosc. Radiat. Transfer 50(3), 267-276, http://dx.doi.org/10.1016/0022-4073(93)90077-U.

Marcq, E., Bézard, B., Drossart, P., Piccioni, G., Reess, J.M., Henry, F., 2008. A latitudinal survey of CO, OCS, H_2O, and SO_2 in the lower atmosphere of Venus: Spectroscopic studies using VIRTIS-H. J. Geophys. Res. 113(E00B07), http://dx.doi.org/10.1029/2008JE003074.

Marcq, E., Belyaev, D., Montmessin, F., Fedorova, A., Bertaux, J.L. et al., 2011. An investigation of the SO_2 content of the Venusian mesosphere using SPICAV-UV in nadir mode. Icarus 211(1), 58-69, http://dx.doi.org/10.1016/ j.icarus.2010.08.021.

Marcq, E., Bertaux, J.L., Montmessin, F., and Belyaev, D., 2013. Variations of sulphur dioxide at the cloud top of Venus's dynamic atmosphere. Nat. Geosci. 6, 25-28, http://dx.doi.org/10.1038/ngeo1650.

Markiewicz, W.J., Petrova, E., Shalgina, O., Almeida, M., Titov, D.V. et al., 2014. Glory on Venus cloud tops and the unknown UV absorber. Icarus 234, 200-203, http://dx.doi.org/10.1016/j.icarus.2014.01.030.

Mecherikunnel, A.T., Gatlin, J.A., Richmond, J.C., 1983. Data on total and spectral solar irradiance. Appl. Opt. 22(9), 1354-1359, http://dx.doi.org/10.1364/AO.22.001354.

Mills, F.P., Esposito, L.W., Yung, Y.L., 2007. Atmospheric composition, chemistry and clouds. In: *Exploring Venus as a Terrestrial Planet*, Esposito, L.W., Stofan, E.R., Cravens, T.E. (Eds.), 73-100, American Geophysical Union, Washington, D.C., ISBN: 978-0-87590-441-2, http://dx.doi.org/10.1029/176GM06.

Molina, L.T., Lamb, J.J., Molina, M.J., 1981. Temperature dependent UV absorption cross sections for carbonyl sulfide. Geophys. Res. Lett. 8(9), 1008-1011, http://dx.doi.org/10.1029/GL008i009p01008.

Moroz, V.I., 1981. The albedo of Venus in the range 0.2-4.0 microns (in Russian). Kosm. Issled. 19(4), 591-598.

Moroz, V.I., Ekonomov, A.P., Moshkin, B.E., Revercomb, H.E., Sromovsky, L.A. et al., 1985. Solar and thermal radiation in the Venus atmosphere. Adv. Space Res. 5(11), 197-232. In: *The Venus International Reference Atmosphere*, Kliore, A. J., Moroz, V.I., Keating, G.M. (Eds.), Adv. Space Res. 5(11), 197-232 (1985), http://dx.doi.org/10.1016/0273-1177(85)90202-9.

Moroz, V.I., Zasova, L., 1997. VIRA-2: A review of inputs for updating the Venus International Reference Atmosphere. Adv. Space Res. 19(8), 1191-1201, http://dx.doi.org/10.1016/S0273-1177(97)00270-6.

Neckel, H. and Labs, D., 1984. The solar radiation between 3300 and 12500 A°. Solar Physics 90(2), 205-258, http://dx.doi.org/10.1007/BF00173953.

Palmer, K.F. and Williams, D., 1975. Optical constants of sulphuric acid: Application to the clouds of Venus. Appl. Opt. 14(1), 208-219, http://dx.doi.org/10.1364/AO.14.000208.

Parkinson, C., Gao, P., Schulte, R., Bougher, S.W., Yung, Y.L., Bardeen, C., 2015. Distribution of sulphuric acid aerosols in the clouds and upper haze of Venus using Venus Express VAST and VeRa temperature profiles. Planet. Space Sci. 113-114, 205-218, http://dx.doi.org/10.1016/j.pss.2015.01.023.

Parkinson, W.H., Rufus, J., Yoshino, K., 2003. Absolute absorption cross section measurements of CO_2 in the wavelength region 163-200 nm and the temperature dependence. Chem. Phys. 290, 251-256, http://dx.doi.org/10.1016/S0301-0104(03)00146-0.

Perrin, M.Y. and Hartmann, J.M., 1989. Temperature-dependent measurements and modeling of absorption by CO2-N2 mixtures in the far line-wings of the 4.3 µm CO2 band. J. Quant. Spectrosc. Radiat. Transfer 42(4), 311-317, http://dx.doi.org/10.1016/0022-4073(89)90077-0.

Piccioni, G., Drossart, P., Suetta, E., Cosi, M., Ammannito, E. et al., 2007. VIRTIS: The Visible and Infrared Thermal Imaging Spectrometer. ESA Spec. Publ. SP-1295, pp. 1–27, European Space Agency, Paris.

Pollack, J.B., Toon, O.B., Whitten, R.C., Boese, R., Ragent, B. et al., 1980. Distribution and source of the UV absorption in Venus' atmosphere. J. Geophys. Res. 85(A13), 8141-8150, http://dx.doi.org/10.1029/JA085iA13p08141.

Pollack, J.B., Dalton, J.B., Grinspoon, D., Wattson, R.B., Freedman, R. et al., 1993. Near-infrared light from Venus' nightside: A spectroscopic analysis. Icarus 103(1), 1-42, http://dx.doi.org/10.1006/icar.1993.1055.

Rossow, W.B., Del Genio, A.D., Limaye, S.S., Travis, L.D., Stone, P.H., 1980. Cloud morphology and motions from Pioneer Venus images. J. Geophys. Res. 85(A13), 8107-8128, http://dx.doi.org/10.1029/JA085iA13p08107.

Rothman, L.S., Wattson, R.B., Gamache, R.R., Schroeder, J.W., McCann, A., 1995. HITRAN HAWKS and HITEMP: high-temperature molecular database. Proc. Soc. Photoopt. Instrum. Eng. (SPIE) 2471, 105-111, http://dx.doi.org/10.1117/12.211919.

Rothman, L.S., Gordon, I.E., Barbe, A., Chris Benner, D., Bernath, P.F., et al., 2009. The HITRAN 2008 molecular spectroscopic database. J. Quant. Spectrosc. Radiative Transf. 110 (9–10), 533–572, http://dx.doi.org/10.1016/j.jqsrt.2009.02.013.

Rothman, L.S., Gordon, I.E., Barber, R.J., Dothe, H., Gamache, R.R., et al., 2010. HITEMP, the high-temperature molecular spectroscopic database. J. Quant. Spectrosc. Radiat. Transf. 111(15), 2139-2150, http://dx.doi.org/10.1016/j.jqsrt.2010.05.001.

Schofield, J.T. and Taylor, F.W., 1982. Net global thermal emission from the Venusian atmosphere. Icarus 52(2), 245-262, http://dx.doi.org/10.1016/0019-1035(82)90111-7.

Schofield, J.T. and Taylor, F.W., 1983. Measurements of the mean, solar-fixed temperature and cloud structure of the middle atmosphere of Venus. Q. J. Roy. Meteorol. Soc. 109, 57-80, http://dx.doi.org/10.1002/qj.49710945904.

Seiff, A., Kirk, D.B., Young, R.E., Blanchard, R.C., Findlay, J.T. et al., 1980. Measurements of thermal structure and thermal contrasts in the atmosphere Venus and related dynamical observations: Results from the four Pioneer Venus probes. J. Gephys. Res. 85(A13), 7903-7933, http://dx.doi.org/10.1029/JA085iA13p07903.

Seiff, A. and Kirk, D.B., 1982. Structure of the Venus mesosphere and lower thermosphere from measurements during entry of the Pioneer Venus probes. Icarus 49(1), 49-70, http://dx.doi.org/10.1016/0019-1035(82)90056-2.

Seiff, A., Schofield, J.T., Kliore, A.J., Taylor, F.W., Limaye, S.S. et 5 al., 1985. Models of the structure of the middle atmosphere of Venus from the surface to 100 kilometers altitude. In: *The Venus International Reference Atmosphere*, Kliore, A. J., Moroz, V.I., Keating, G.M. (Eds.), Adv. Space Res. 5(11), 3-58 (1985), http://dx.doi.org/10.1016/0273-1177(85)90197-8.

Shemansky, D.E., 1972. CO_2 extinction coefficients 1700-3000 A°. J. Chem. Phys. 56, 1582-1587, http://dx.doi.org/10.1063/1.1677408.

Sidebottom, H.W., Badcock, C.C., Jackson, G.E., Calvert, J.G., Reinhardt, G.W., Damon, E.K., 1972. Photooxidation of sulfur dioxide in the vacuum ultraviolet. Environm. Sci. Technol. 6, 72-79.

Smith, W.L., 1970. Iterative solution of the radiative transfer equation for the temperature and absorbing gas profile of an atmosphere. Appl. Opt. 9(9), 1993-1999, http://dx.doi.org/10.1364/AO.9.001993.

Stamnes, K., Tsay, S.C., Wiscombe, W. and Jayaweera, K., 1988. Numerically stable algorithm for discrete-ordinate-method radiative transfer in multiple scattering and emitting layered media. Appl. Opt. 27(12), 2502-2509, http://dx.doi.org/10.1364/AO.27.002502.

Tashkun, S.A., Perevalov, V.I., Teffo, J.L., Bykov, A.D., Lavrentieva, N.N., 2003. CDSD-1000, the high-temperature carbon dioxide spectroscopic databank. J. Quant. Spectrosc. Radiat. Transfer 82(1-4), 165-196, http://dx.doi.org/10.1016/S0022-4073(03)00152-3.

Taylor, F.W., 2006. Venus before Venus Express. Planet. Space Sci. 54(13-14), 1249-1262, http://dx.doi.org/10.1016/j.pss.2006.04.031.

Tellmann, S., Pätzold, M., Häusler, B., Bird, M.K., Tyler, G.L., 2009. Structure of the Venus neutral atmosphere as observed by the Radio Science experiment VeRa on Venus Express. J. Geophys. Res. 114(E00B36), 354-372, http://dx.doi.org/10.1029/2008JE003204.

Thekaekara, M.P., 1973. Solar energy outside the Earth's atmosphere. Solar Energy, 14(2), 109-127, http://dx.doi.org/10.1016/0038-092X(73)90028-5.

Thompson, B.A., Harteck, P., Reeves Jr., R.R., 1963. Ultraviolet absorption coefficients of CO_2, CO, H_2O, N_2O, NH_3, NO, SO_2, and CH_4 between 1850 and 4000 A°. J. Geophys. Res. 68(24), 6431-6436, http://dx.doi.org/10.1029/JZ068i024p6431.

Thompson Jr., R.T., Hoell Jr., J.M., Wade, W.R., 1975. Measurements of SO2 absorption coefficients using a tunable dye laser. J. Appl. Phys. 46, 3040, http://dx.doi.org/10.1063/1.321995.

Titov, D.V., 1995. Radiative balance in the mesosphere of Venus from the Venera-15 infrared spectrometer results. Adv. Space Res. 15(4), 73–77, http://dx.doi.org/10.1016/0273-1177(94)00066-A.

Titov, D.V., Svedhem, H., Taylor, F.W., 2006. The atmosphere of Venus: Current knowledge and future investigations. In *Solar System Update*, Blondel, P., and Mason, J.W. (Eds.), pp. 87-110, Springer Praxis Publishing, Chichester, UK, http://dx.doi.org/10.1007/3-540-37683-6_3.

Titov, D.V., Bullock, M.A., Crisp, D., Renno, N.O., Taylor, F.W., Zasova, L.V., 2007. Radiation in the Atmosphere of Venus. In *Exploring Venus as a Terrestrial Planet*, Esposito, L.W., Stofan, E.R., and Cravens, T.E. (Eds.), AGU Geophysical Monograph Series 176, 121-138, ISBN: 978-0-87590-441-2.

Titov, D.V., Taylor, F.W., Svedhem, H., Ignatiev, N.I., Markiewicz, W.J. et al., 2008. Atmospheric structure and dynamics as the cause of ultraviolet markings in the clouds of Venus. Nature 450, 620-623, http://dx.doi.org/10.1038/nature07466.

Titov, D.V., Piccioni, G., Drossart, P., Markiewicz, W.J., 2012. Radiative energy balance in the Venus Atmosphere. In *Towards Understanding the Climate of Venus*, Bengtsson, L., Bonnet, R.M., Grinspoon, D., Koumoutsaris, S., Lebonnois, S, Titov, D. (Eds.), ISSI Scientific Report Series 11, 23-53, ISBN: 978-1-4614-5063-4.

Tomasko, M.G., Doose, L.R., Smith, P.H., Odell, A.P., 1980. Measurements of the flux of sunlight in the atmosphere of Venus. J. Geophys. Res. 85(A13), 8167-8186, http://dx.doi.org/10.1029/JA085iA13p08167.

Tomasko, M.G., Doose, L.R., Smith, P.H., 1985. The absorption of solar energy and the heating rate in the atmosphere of Venus. Adv. Space Res. 5(9), 71–79, http://dx.doi.org/10.1016/0273-1177(85)90272-8.

Tonkov, M.V., Filippov, N.N, Bertsev, V.V., Bouanich, J.P., Van-Thanh, N. et al., 1996. Measurements and empirical modeling of pure CO_2 absorption in the 2.3 μm range at room temperature: far wings, allowed and collision-induced bands. Appl. Opt. 35 (24), 4863-487, http://dx.doi.org/10.1364/AO.35.004863.

Toon, O.B., Turco, R.P., Pollack, J.B., 1982. The ultraviolet absorber on Venus: Amorphous sulfur. Icarus 51(2), 358-373, http://dx.doi.org/10.1016/0019-1035(82)90089-6.

Tsang, C.C.C., Irwin, P.G.J., Wilson, C.F., Taylor, F.W., Lee, C. et al., 2008. Tropospheric carbon monoxide concentrations and variability on Venus from Venus Express/VIRTIS-M observations. J. Geophys. Res. 113(E00B08), 13pp., http://dx.doi.org/10.1029/2008JE003089.

Vandaele, A.C., Hermans, C., Fally, S., 2009. Fourier Transform measurements of SO_2 absorption cross sections: II. Temperature dependence in the 29000-44000 cm-1 (227-345 nm) region. J. Quant. Spectr. Rad. Transfer 110(18), 2115-2126, http://dx.doi.org/10.1016/j.jqsrt.2009.05.006.

Wallace, L., Caldwell, J.J., Savage, B.D., 1972. Ultraviolet photometry from the Orbiting Astronomical Observatory. III. Observations of Venus, Mars, Jupiter,

and Saturn longward of 2000 A. Astrophys. J. 172, 755-769, http://dx.doi.org/10.1086/151393.

Warneck, P., Marmo, F.F., Sullivan, J.O., 1964. Ultraviolet absorption of SO_2: Dissociation energies of SO_2 and SO. J. Chem. Phys. 40, 1132-1136, http://dx.doi.org/10.1063/1.1725260.

Watanabe, K. and Zelikoff, M., 1953. Absorption coefficients of water vapor in the vacuum ultraviolet. J. Opt. Soc. Am. 43(9), 753-754, http://dx.doi.org/10.1364/JOSA.43.000753.

Wiscombe, W.J., 1980. Improved Mie scattering algorithms. Appl. Opt. 19(9), 1505-1509, http://dx.doi.org/10.1364/AO.19.001505.

Wu, C.Y.R., Yang, B.W., Chen, F.Z., Judge, D.L., Caldwell, J., Trafton, L.M., 2000. Measurements of high-, room-, and low- temperature photoabsorption cross sections in the 2080- to 2950-A° region, with application to Io. Icarus 145(1), 289-296, http://dx.doi.org/10.1006/icar.1999.6322.

Zasova, L.V., Spänkuch, D., Moroz, V.I., Schäfer, K., Ustinov, E.A. et al., 1985. Infrared experiment onboard Venera-15 and Venera-16 (in Russian). Kosm. Issled. 23(2), 221-235.

Zasova, L.V., Moroz, V.I., Linkin, V.M., Khatuntsev, I.V., Maiorov, B.S., 2006. Structure of the Venusian atmosphere from surface up to 100 km. Cosmic Res. 44(4), 364-383, http://dx.doi.org/10.1134/S0010952506040095.

Zasova, L.V., Ignatiev, N.I., Khatuntsev, I., Linkin, V., 2007. Structure of the Venus atmosphere. Planet. Space Sci. 55(12), 1712-1728, http://dx.doi.org/10.1016/j.pss.2007.01.011.